AN EXPERIMENTAL CHARACTERIZATION OF A MULTI-ELEMENT LEAN PREMIXED PRE-VAPORIZED COMBUSTOR FOR SUPERSONIC TRANSPORT APPLICATIONS

A Dissertation
Presented to
The Academic Faculty

by

Mitchell Louis Passarelli

In Partial Fulfillment
of the Requirements for the Degree
Doctor of Philosophy in the
School of Aerospace Engineering

Georgia Institute of Technology

December 2023

AN EXPERIMENTAL CHARACTERIZATION OF A MULTI-ELEMENT LEAN PREMIXED PRE-VAPORIZED COMBUSTOR FOR SUPERSONIC TRANSPORT APPLICATIONS

Thesis committee:

Dr. Adam M. Steinberg, Advisor
School of Aerospace Engineering
Georgia Institute of Technology

Dr. Ellen Yi Chen Mazumdar
School of Mechanical Engineering
Georgia Institute of Technology

Dr. Jerry M. Seitzman
School of Aerospace Engineering
Georgia Institute of Technology

Dr. Krishna Venkatesan
Combustion Systems
GE Aerospace – Research

Dr. Tim C. Lieuwen
School of Aerospace Engineering
Georgia Institute of Technology

Date approved: December 11, 2023

ACKNOWLEDGEMENTS

With another chapter of my life coming to a close, I want to reflect on my time during my PhD studies and all those who supported me. The last four years have passed in what feels like the blink of an eye despite all that has happened in my life. From moving to a new city and making new friends, enduring a global pandemic and tackling a seemingly endless series of deadlines, my PhD life has been both stressful and rewarding in equal measures. I knew that it was not going to be easy, since it is the challenges that make it worth the effort. I have learned so much, not only about combustion and aerospace engineering, but also myself in sometimes unexpected ways. I am truly grateful for all of the opportunities I have been given and all of the experiences I now have thanks to my time at Georgia Tech. Still, I could never have done this on my own and I want to thank everyone for their support. Alas, I have no skill in writing and not enough space for this, but I will try to put in words how I feel.

First, to my advisor Prof. Adam Steinberg: thank you for supporting me and trusting in my work. When I did not believe in myself or understand the importance of parts of my work, you patiently led me through my struggles. The projects I have worked on throughout my graduate studies at both the University of Toronto and Georgia Tech have been invaluable learning experiences with exciting real-world applications. I have also grown under his supervision, learning to see beyond the scope of a single experiment to the breadth of possible applications. Adam's guidance has helped me to publish my research in prestigious journals and present at many conferences to audiences from around the world. Also, sorry it took so long to get to a first-name basis: bad habits are hard to kick.

I would like to acknowledge the financial support I received for my work. The Natural Sciences and Engineering Research Council of Canada (NSERC) postgraduate scholarship program provided me with a, sometimes critical, cushion for the expenses of living and learning abroad. The primary funding for my research was provided by grants through the Federal Aviation Administration (FAA) ASCENT program and through collaboration with GE Aerospace. GE allowed me to travel to their facilities to conduct my experiments and learn first-hand what goes into the development of actual gas turbine combustors in industry. To Krishna Venkatesan, Victor Salazar, Hannah Bower, John Hong, Arin Cross and the other GE engineers, it has been a pleasure and honour to work with you. Thank you for your patience, advice and support, even when it seems everything would go wrong. And to Walt and Tony, thank you for being such incredible people. Your extraordinary skills and enthusiasm are what make this work possible for us engineers.

Of course, I cannot forget the wonderful people at Georgia Tech and the Ben T. Zinn Combustion Lab. My lab-mates, Manya, Sam W., Jeremiah, Adhiraj, Jonathon, Jean-Luis, Cathy, Ari, Dominic, Askar and Boni are the silliest, brightest and most supportive co-workers anyone could ask for. The extended lab family, including Shivam, Parth, Hari Priya, Conner, Vedanth, Hanna, David, Kris, Seth, Ben and Vishal are a friendly and welcoming bunch that made the lab feel like home to me. Thank you all for putting up with me, whether I was complaining about the latest issues with my experimental campaigns, rambling about my hyper-fixation of the day or asking for a “sanity-check”. Even if I was less productive for it, each day spent at the lab with each of you made my life better. From studying for quals with Manya during the pandemic, to silly games with Adhiraj, to our infrequent cocktail nights, to gossiping and chilling with Boni, I have enjoyed every

moment. I will miss all of you dearly. So please give me a shout if you are ever in Toronto, or wherever I end up, or anytime!

To Askar, whom I seemingly followed from UTIAS to Georgia Tech, and has been a close friend, sounding board and supporter: thank you so much. Your example, your knowledge, passion, humour and drive kept me going even when I didn't know where I was headed. The last year of my PhD made me realize how much I enjoyed our walks back from the lab, talking about anything and everything to pass the time. If our phone calls now reflect anything, it's that we will never run out of things to talk about.

Thank you to those who weathered each GE campaign with me. Ketana, Sam Grauer, Sam Wonfor, Andy, Manya, Askar and Seunghyun have seen me at my best and my worst during those long months. Your reliability, patience and cooperation were what got me through to the end. I could not have asked for a better set of partners. Sam W. and Andy especially, even though it wasn't the best circumstances, I will cherish the time we spent together during those campaigns. I must also thank my undergraduate research assistants, Rachel, Kailey, Mihir and Ben, who saved me from countless hours poring through all the data from those campaigns. And to the next generation of GE collaborators, I wish you the best of luck!

Moving to Atlanta was stressful for me. I have never liked going through major changes and moving to another country is almost as big of a change as they come. Tom and Elizabeth welcomed me immediately into their home and took such amazing care of me. Whether it was celebrating American Thanksgiving with them or just going out for dinner together, Tom and Elizabeth treated me like I was part of their family. Tom's incredibly quick wit and humour always makes me laugh and Elizabeth's foodie tips helped me

explore the new city I was living in. I am so fortunate to have had both of you nearby and your support gave me the piece of mind I needed.

My friends back home in Toronto have been such great supporters for me that I doubt I can express my gratitude. To Phil, Rob, Eric, Jonathon, Logan, Kyle, Ryan, Chris and Pat: your encouragement means the world to me. I am so fortunate to have friends like you and I want you to know what it meant to me just knowing that each of you were there for me. From hanging out when I was in town to just chatting and playing games online, all of you have made the dark times brighter.

Finally, to my family: there are no words. I only know that I could not have made it without your constant love and support. My mom and dad have been a bedrock of support for me, always making time to help even for the smallest of things. My brothers never fail to put a smile on my face and help me forget whatever problems I might be dealing with. None of you ever doubted me, even when I doubted myself. It is the greatest comfort knowing that you are in my life. What I have achieved here is all thanks to you.

TABLE OF CONTENTS

LIST OF TABLES

LIST OF FIGURES

LIST OF SYMBOLS

Acronyms

BR Bypass Ratio

CL Chemiluminescence

CO Carbon monoxide

CO_2 Carbon dioxide

CST Commercial Supersonic Transport

DAQ Data Acquisition Unit

DFT Discrete Fourier Transform

EICO Emissions Index of Carbon monoxide

EINOx Emissions Index of Nitrous Oxides

EMD Empirical Mode Decomposition

FAR Fuel-Air (mass) Ratio

FFT Fast Fourier Transform

FTF Flame Transfer Function

GPOD Gappy Proper Orthogonal Decomposition

LBO Lean Blowoff

LDI Lean Direct Injection

LPP Lean Premixed Pre-vaporized

NOx Nitrous oxides

nvPM Non-volatile Particulate Matter

OH Hydroxyl

OPR Overall Pressure Ratio

PIV Particle Image Velocimetry

PLIF Planar Laser Induced Fluorescence

RMS Root Mean Square

RPM Revolutions Per Minute

RQL Rich burn-Quench-Lean burn

SPIV Stereoscopic Particle Image Velocimetry

TP Test Point

UHC Unburnt Hydrocarbons

Nomenclature

A	Main annulus area
Da	Damköhler number
$\mathrm{Da_{LBO}}$	Damköhler number at blowoff
d_{bb}	Main bluff-body diameter
d_{o}	Main annulus outer diameter
F	Forcing amplitude
f	Cyclic frequency
f_0	Natural (unforced) frequency
f_{f}	Forcing frequency
f_{o}	Observed frequency
$\dot{m}_{\mathrm{air}}$	(Total mixer) air mass flow rate
$\dot{m}_{\mathrm{f,p}}$	Pilot fuel mass flow rate
$\dot{m}_{\mathrm{main}}$	Total single main mass flow rate
P_3	Combustor inlet/reactant pressure
$\mathcal{P}_{\mathrm{max}}$	Spatial maximum spectral power
$\mathcal{P}_{\mathrm{sum}}$	Spatial sum spectral power
$\mathcal{P}_{\mathrm{th}}$	Thermal power
Re	Reynolds number
$S_{\mathrm{L}}{}^0$	Unstretched laminar flame speed
T_3	Inlet/reactant temperature
T_4	Combustor exit temperature
T_{prod}	Products temperature
v_{main}	Main jet velocity
W_{air}	Air molecular weight
W_{f}	Fuel molecular weight
$\Delta(\cdot)$	Uncertainty
Δf	Frequency detuning
$\delta_{\mathrm{f}}{}^0$	Unstretched laminar flame thickness
θ	Laminar boundary layer momentum thickness
μ_3	Reactant dynamic viscosity
ρ_3	Combustor inlet/reactant density
τ_{chem}	Chemical time scale
τ_{flow}	Flow time scale
φ	Total equivalence ratio
φ_{p}	Pilot equivalence ratio
ω	Radial frequency
$(\cdot)'$	Fluctuations of a quantity

SUMMARY

Recent trends have driven a re-emergence of research and development in aircraft engines for commercial supersonic transport (CST). Despite the vast body of literature that exists for gas turbine combustors operating at conditions relevant to conventional subsonic flight, there is little to validate extensions of this knowledge to the conditions encountered by CST engines. Further complications arise from advanced combustor designs that involve multiple different flames or flow devices. The interactions of such combustor elements can lead to individual behaviours that differ from that of single elements.

The existing literature on flame and flow interactions is focused on conditions relevant to the operation of conventional, subsonic aircraft engines. While such works provide a baseline understanding of the physical phenomena involved in such interactions, they do not necessarily predict the behaviours exhibited by different combustor configurations and/or at different conditions. Some recent studies have employed numerical simulations to determine the characteristics of various combustor schemes, including lean direct injection and lean premixed pre-vaporized (LPP) designs. These studies are limited by the lack of empirical data for validation and model development.

The work presented herein aims to characterize experimentally the flow field, flame dynamics and operating limits of a multi-element LPP combustor operating at CST-relevant conditions. Simultaneous laser and probe-based diagnostics were employed to obtain measurements of pollutant emissions, flow velocities, heat release rate, fuel-air mixing and thermoacoustic dynamics. The effects of combustor inlet pressure, temperature and fuel-air ratio are studied via corresponding parameter sweeps. Numerical chemistry simulations

provide estimates of relevant flame properties, complementary to the experimental results. A second set of experiments investigated the forced response of the combustor.

Overall, the results presented in this thesis demonstrate the importance of flame and flow interactions. In particular, the interactions of the pilot flame with neighbouring main flames are found to be critical in determining the stable operating range of the combustor. Furthermore, the pilot is found to dominate the dynamics of the combustor at forced and unforced conditions. Empirically-computed flame transfer functions at different forcing frequencies show that the pilot is most sensitive to acoustic perturbations and that this sensitivity is enhanced by interactions of the pilot with the main flames.

This work also demonstrates the viability of LPP combustors for CST applications in three aspects. First, the pollutant emissions characteristics of the combustor studied are in line with future emissions targets. Second, the mean flow field, flame and dynamical characteristics do not vary strongly with operating conditions or undergo sudden or unexpected bifurcations, except when exceeding blowoff limits. A Damköhler number (Da)-based blowoff analysis shows that this combustor design exhibits enhanced stability compared with previously reported bluff-body stabilized flames. The analysis itself also demonstrates the robustness of a simple Da correlation for blowoff prediction, which works for a complex geometry such as the one studied in this work.

CHAPTER 1

INTRODUCTION

1.1 Motivation

The continuous, ongoing push for reduced pollutant emissions around the globe is a key factor in gas turbine engine development. Recent studies [1] have shown there is a significant potential for improvement by developing aircraft engines optimized for supersonic flight. Market demand for high-speed transport is expected to drive a rapid re-emergence of commercial supersonic transport (CST) aircraft over the coming decades. This impending CST revival, combined with the increasingly harmful impacts of anthropogenic climate change, mandate advancements in CST-focused environmentally compatible technologies and policies.

In contrast to subsonic aircraft, engines for CST aircraft will (i) operate at significantly lower overall pressure ratio (OPR) and bypass ratio (BR); (ii) experience higher combustor inflow temperatures (T_3), lower pressures (P_3) and higher fuel-air ratios (FARs) at cruise; and (iii) cruise at higher altitudes. The reduced OPR and BR result in increased thrust-specific fuel consumption, thus increasing fuel burn and making it fundamentally more challenging to reduce emissions. Furthermore, the combination of low OPR and high cruise T_3 and FAR result in complicated trade-offs between nitrous oxide (NOx) at cruise and other emissions (CO, non-volatile particulate matter (nvPM) and unburnt hydrocarbons (UHC)) at lower power [2]. The environmental impact of flight emissions at supersonic cruise altitudes are not yet fully understood but are known to be strongly dependent on the altitude, emissions characteristics and likely the latitude of

emissions [3-5]. To address such issues, the Committee on Aviation Environmental Protection (CAEP) of the International Civil Aviation Organization (ICAO) has created a working group focused on CST exhaust emissions regulations. CAEP is also conducting an exploratory study on the global environmental impact of future CST aircraft.

The emissions of conventional, subsonic aero-engines have been studied for several different combustor architectures [2, 6]. Of particular relevance to this work are the rich burn-quench-lean burn (RQL), lean direct injection (LDI) and lean premixed pre-vaporized (LPP) architectures. These and other styles of combustors are reviewed extensively by Liu *et al*. [2]. RQL combustors operate with a fuel-rich head end flame, followed by a quench zone where the burning gases mix rapidly with cooler air to oxidize partial combustion products and transition to fuel-lean combustion [2]. In principle, the rapid dilution reduces NOx emissions by avoiding near-stoichiometric equivalence ratios and thermal NOx production, shown schematically in Figure 1 [7]. As Figure 1 illustrates, the finite time required for the dilution and mixing in the quench zone means that there is a transition through the peak NOx production equivalence ratios. This means that the design of the dilution is critical to the optimal functioning of an RQL combustor.

Beyond emissions benefits, the rich head-end flame enhances overall flame stability in terms of both attachment and response to dynamics, both of which have been demonstrated by the widespread success of RQL combustors in existing aero-engines [2, 8]. One of the main drawbacks of RQL combustors, however, is the increase in NOx emissions as OPR increases to improve combustion efficiency [2, 6]. While this is less of an issue at CST conditions, the higher T_3 yields higher flame temperatures and thus more NOx emissions.

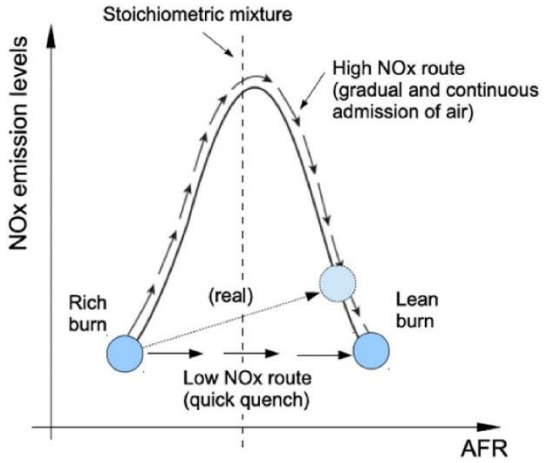

Figure 1: Schematic of NOx production routes and RQL operating principle [2].

Several recent studies have assessed potential CST fleet emissions and environmental impact [3-5, 9, 10]. However, these studies typically employed legacy, subsonic "donor" engine cores and have extrapolated CST emissions predictions from correlations based on ground testing data at subsonic flight conditions. Berton *et al*. [10] equipped their aircraft with a supersonic variant of a commercial CFM56-7B—modeled using the Numerical Propulsion System Simulation (NPSS) code [11]—with a modified low pressure spool and fan. Emissions regression models were created for NOx, CO and UHC based on a ground-level emission data for the original CFM56-7B and extrapolated to the combustor conditions (P_3, T_3) of the supersonic engine. Similarly, Speth *et al*. [12] used a CFM56-5B as the donor engine, allowed variations in the fan and compressor for the supersonic engine, modeled the engine with NPSS, leveraged ground testing data, and used a (P_3, T_3) method to model emissions from the supersonic engine; Speth *et al*. [12] also included a constant emissions index model for nvPM. However, both the CFM56-5B and -7B use Tech Insertion RQL combustors developed in the 1990s.

Some recent studies have performed "clean sheet" CST engine designs using NPSS, modifying many of the restrictions placed by the donor engine but still considering a Tech Insertion RQL combustor [9, 10, 13, 14]. Voet *et al*. [13] modeled the emissions using a chemical reactor network, validated against the aforementioned ground test data at subsonic-relevant conditions. Hassan *et al*. [14] considered the NASA Glenn (P_3, T_3) correlation for this combustor, Boeing Fuel Flow Method (Version 2) for NOx modeling and some other correlations [15, 16].

Studies such as these demonstrate that major innovations in combustor architecture will be required to meet emissions targets and create an environmentally compatible CST market. Despite the high T_3 and FAR, peak flame temperatures must be moderated to meet NOx targets, while also maintaining efficiency and achieving low CO, UHC and nvPM. This will require increased fuel-lean premixing prior to combustion.

LDI combustors offer one solution for reducing NOx emissions at high OPR. In LDI, the fuel is injected directly into the combustor with an excess of air to yield an overall fuel-lean mixture [2]. Using Figure 1, LDI strategies operate directly at the "lean burn" conditions, focusing on optimizing fuel-air mixing prior to combustion to ensure low flame temperatures. LDI combustors also typically employ internal fuel staging, with a lower flow rate "pilot" flame burning at FARs to ensure flame stability, while a majority of the fuel is burned in the "main" flames [2]. The staged configurations that have been studies introduce complications to flame stability and dynamics as the main and pilot flames interact [2]. Furthermore, the rapid mixing of fuel and air prior to combustion is critical to the operation and emissions of LDI combustors. This poses a particular challenge at the high T_3 encountered at CST conditions.

Recently, the potential of using modern LDI configurations at CST conditions has been investigated experimentally by Tacina *et al*. [17] and computationally by Ajmani *et al*. [18]. Tacina *et al*. [17] studied a 3-cup, 19-element "LDI-3" configuration at T_3 = 922 K and P_3 = 19 bar. Although the targeted equivalence ratio and post-flame temperature T_4 for CST cruise could not be achieved, the EINOx was extrapolated to the desired T_4 based on correlations. Experimental EINOx values were estimated to be 25 g/kg at T_4 = 1,990 K and 40 g/kg at T_4 = 2,085 K, which agreed well with the CFD predictions. Given the high T_4, these values are promising and indicate the potential for LDI in CST.

LPP combustors have been shown theoretically to have very high potential for ultra-low NOx emissions, especially when operating with liquid fuels [2, 6, 15]. In an LPP combustor, the fuel is vaporized and then mixed with the air to produce a uniform equivalence ratio mixture prior to burning. As a result, LPP combustors aim to operate at equivalence ratios close to the lean blowoff (LBO) limit. The homogeneous equivalence ratio eliminates potential hot spots in the combustor, where thermal NOx production could be an issue [2], similar to LDI operating conditions. Overall, LPP combustors have several attractive features over other combustor architectures, including lower coking risk and reduced complexity due to fewer injectors. Unfortunately, the premixed fuel and air pose a challenge for preventing flashback and autoignition in LPP combustors operating at subsonic conditions with high OPR [2]. Preventing flashback and autoignition requires combustor designs that minimize the residence time of the mixed reactants within the combustor [2, 7]. When operating with liquid fuels, however, this poses an issue for achieving complete pre-vaporization and premixing of the fuel [15]. However, these issues can potentially be alleviated by the high T_3 in CST combustors—which results in faster

vaporization—and advanced manufacturing to enable compact rapid-mixing flow elements.

Operating at such lean equivalence ratios also increases sensitivity to turbulent and acoustic fluctuations, potentially causing severe combustion dynamics or blowoff [8, 19, 20]. One method to address such flame stability issues is to apply staged fueling schemes similar to those found in LDI combustors. In such designs, it is crucial to understand how the various flames and flows interact. Furthermore, there are few experimental studies of LPP combustors, even at conditions relevant to subsonic flight [8, 20]. The collection of empirical data for practical gas turbine combustors operating at CST-relevant conditions is an important research task. Such experimental results can be used to validate existing extrapolated results, such as those presented above, along with developing improved models for predicting combustor performance.

The research in this thesis is focused on the experimental characterization of a novel, multi-element LPP combustor operating at conditions of relevance for CST engines. The data presented herein provides detailed measurements of the combustor flow field, dynamics and emissions which can be used in validating models for use in designing CST engines. Furthermore, this work analyzes how the behaviour of this LPP combustor compares with theoretical expectations and that of existing subsonic aircraft engines.

1.2 Outline

This thesis is structured as follows. The remainder of this chapter summarizes and highlights the relevant theoretical concepts in nonlinear dynamics, flame stabilization and thermoacoustic modelling. An emphasis is placed on the concepts of flame stabilization,

hysteresis, flame transfer functions and frequency interactions. The chapter closes with an explanation of the research objectives for this work.

Chapter 2 describes the setup of the experiments in the data collection campaigns. This includes an explanation of the various diagnostics deployed, the specific implementations and equipment used and the data preprocessing procedures. Resolutions and accuracy of the measurements are also discussed.

Chapter 3 explains the data analysis techniques used in this work. The first two sections present the equations and numerical simulations used to compute Reynolds and Damköhler numbers for flame stability analysis. This is followed by an evaluation of the uncertainty in the calculations, how the experimental results were used to assess flame stability and impact on interpreting results. Finally, the section closes with an overview of the analysis techniques used to characterize combustor dynamics.

Chapter 4 characterizes the mean flow field within the combustor across both experimental campaigns. The results are organized by parameter sweeps of fuel-air ratio, inlet pressure and inlet temperature. These mean fields are used to explore how the combustor changes across each of the parameter sweeps. The chapter closes with a similar investigation of the natural combustor dynamics.

In Chapter 5, the results of the blowoff analysis are explored. The results are compiled across all test conditions and the test points that exhibit blowoff of at least one main flame are compared to trends previously reported in literature. These comparisons elucidate the parameters important to preventing blowoff in the type of combustor investigated.

The response of the combustor and flame to external applied forcing are analyzed in Chapter 6. First, the effects of the forcing on the mean flow field are isolated before examining the flame transfer function and forced dynamics. The effects of frequency interactions are discussed in the context of flame transfer function measurements and interpretations.

The thesis closes with a summary of the work and primary contributions in Chapter 7. The main takeaways focus on the practicality of LPP style combustors for CST applications, especially in terms of operations and dynamics. The gaps of the present work are also identified with brief suggestions of future work to address them.

1.3 Literature Review

1.3.1 Flame stabilization & blowoff

Flame stabilization is a primary concern for new combustor designs, especially LPP configurations which operate so close to the lean limits. Phenomena such as flashback and blowoff dictate the operational limits, such as minimum fuel-air ratios, mass flow rates and combustor geometry [7]. Flame blowoff occurs when local flow time scales, such as those related to flame strain rates, exceed limits set by local chemical time scales and results in a loss of combustion within the engine [7]. The propagation speed of a flame is a chemical property controlled by several parameters such as P_3, T_3, equivalence ratio (φ) and mixing via flow turbulence [7]. The strong decreasing trend of flame speeds due to φ away from the optimal—typically slightly rich [7]—condition is a particularly relevant issue, given the industry and regulatory focus on reducing emissions from combustors (*e.g.*, Ref. [21]). The effects of turbulence are also difficult and costly to quantify accurately and practical combustors operate in turbulent combustion regimes. As such, much of the existing

literature [22-25] relies on empirical research to develop both physics-based descriptions and numerical models of blowoff.

Existing combustors employ several different approaches to stabilize flames in high-speed flows, including bluff-body and swirl stabilization [22, 23]. In general, flames are typically stabilized along or within low-speed regions or features of a flow (*e.g.*, shear layers, etc.) [22], with the differences in approaches arising from how these shear layers are formed. In bluff-body stabilization, the wake behind an object mechanically obstructing the flow creates the shear layers and low speed regions to anchor a flame [22, 23]. Swirl stabilization aerodynamically anchors the flame using the shear layers and recirculation zones that form due to a strong azimuthal, or swirling, velocity component [7, 23, 26].

Bluff-body stabilization is reviewed extensively by Shanbhogue *et al*. [22] and Tuttle [23], so a brief overview is provided here. As both works state, blowoff occurs due to a competition between chemical and flow time scales, which can be captured via Damköhler number (Da) correlations [22, 23], further described in Chapter 3. Fundamentally, the blowoff process is much more complex as Shanbhogue *et al*. [22] discuss several different open questions regarding the specifics of the blowoff process. Further complications arise from flame and flow interactions in multi-element combustors. Such designs may involve several swirl and/or bluff-body stabilized flames that can interact with one another chemically and hydrodynamically. However, Damköhler number correlations have been shown to be independent of fuel type, depending only on flow velocities and combustor geometry [22]. This commonality suggests a universal physical mechanism for blowoff. The process described by Shanbhogue *et al*. [22] for bluff-body stabilized flames is summarized here for reference.

Consider a stable, attached flame that is approaching blowoff via decreasing Da—via decreasing FAR, increasing flow velocity, etc.—as shown in Figure 2. Below some value, the local strain rate intermittently exceeds the extinction strain rate, creating holes in the flame from local extinction events ("stage 1" in Figure 2) [26]. As Da decreases further, these local extinction events become more frequent. Eventually, the holes in the flame sheet appear so frequently that it leads to larger scale disruptions of the wake fluid mechanics ("stage 2" in Figure 2). Decreasing Da further causes an abrupt change with the occurrence of global blowoff of the flame. Shanbhogue *et al*. [22] explain that Da correlations primarily capture the physics associated with the first stage of the blowoff process and cannot predict the ultimate condition that leads to global flame blowoff.

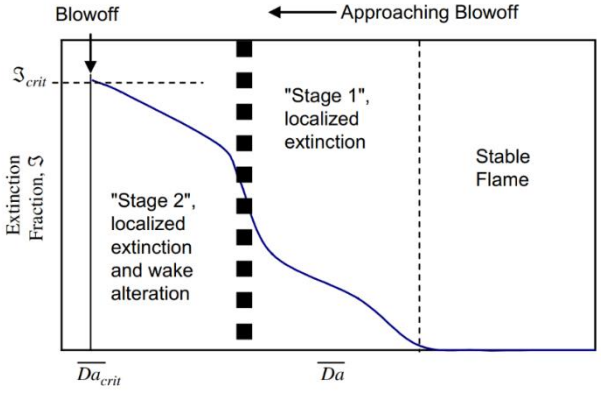

Figure 2: Stages of the blowoff process, reproduced from [22].

The successful use of Damköhler number correlations [22-24, 26], however, indicates that a higher-scale framework should be broadly applicable to blowoff. Both theory and literature [7, 27-29] illustrate that ignition and extinction—and blowoff—exhibit hysteresis and sudden bifurcations. In nonlinear dynamical systems parlance, hysteresis occurs when there exist multiple stable solutions to a system of differential

equations that result in different bifurcation points when the bifurcation parameter is varied from either side of the bifurcation. The sudden change in trajectory due to bifurcations with hysteresis is called a "catastrophe" [30]. This is illustrated schematically in Figure 3. Hysteresis is typically a symptom of multistability, where several stable solutions exist for a given set of parameters. As a result, strong perturbations can push a trajectory from one solution branch to another, but not return, such as in blowoff. Consider a flame that is along the "strongly burning branch" in Figure 3, but close to the extinction point. While a small variation in chemical or flow time scales could cause the flame to become extinguished, it would take a significantly larger change to reignite the flame. In the context of blowoff, hysteresis means that the operating conditions for reignition are much different than those where blowoff may occur. As such, blowoff limits in practice are often less lean than theoretical limits, owing to the need for robust combustor operations.

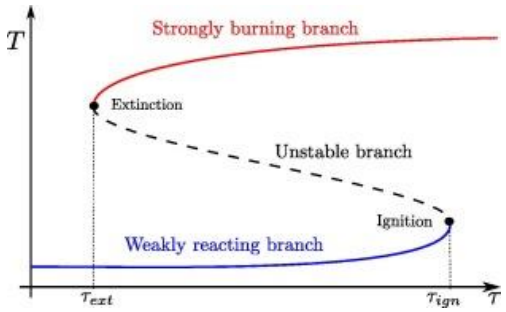

Figure 3: Ignition-extinction bifurcation with hysteresis of a perfectly stirred reactor [28].

1.3.2 Thermoacoustics & flame transfer functions

One of the most common issues encountered in LPP combustor operation is unwanted combustion dynamics, especially thermoacoustic oscillations. Thermoacoustic oscillations are a form of self-excited combustion instability wherein oscillations in the pressure and

heat release rate couple to drive each other. The local rate of energy transfer between the heat release and pressure oscillations is expressed by the Rayleigh Index,

$$\theta(\vec{x},t) \propto \frac{\omega}{\pi}\int_{t-\pi/2\omega}^{t+\pi/2\omega} P'(\vec{x},\tau)\dot{q}'(\vec{x},\tau)\,d\tau \qquad (1)$$

where P' is the pressure fluctuation, $\dot{q}'$ is the fluctuation in heat release rate, ω is the frequency of the oscillations and the integral is over the time interval centred at t. The volume integral of θ represents the source of acoustic energy within the integrated volume. When this is greater than the damping and net flux of acoustic energy, the oscillations will grow in amplitude; when it is negative, they will decay. Θ is positive when P' and $\dot{q}'$ are less than 90° out of phase and θ is negative when they are at least 90° out of phase [31, 32]. Hence, understanding the thermoacoustic behaviour in a combustion chamber requires measurements of both the pressure and heat release rate fluctuations.

As Culick [19] explains, the trend towards leaner φ operating conditions to reduce NOx emissions tends to exacerbate thermoacoustic oscillations. Specifically, the cooler flame temperatures cause the physical processes within gas turbine combustors to be less stable than at higher flame temperatures [19]. Furthermore, as systems operate closer to lean blowoff limits, the flame dynamics tend to become more sensitive to fluctuations, which can lead to additional unwanted oscillatory dynamics [19]. The large body of literature on gas turbine combustion dynamics [8, 19, 32-34] reflects the complexity of the physical mechanisms that generate thermoacoustics and the ongoing work to understand them.

While researchers explore the physics of combustion dynamics, engineers must still analyze and design new combustors to meet emissions regulations. Passive damping is one approach used to control—and in some cases eliminate—unwanted dynamics [8, 19].

Unfortunately, size and weight restrictions in aeronautical gas turbine engines preclude the use of passive damping devices for all oscillations [19, 33]. This requires engine designers to use more advanced analyses and tools to predict and prevent unwanted dynamics [19, 32, 33]. Despite advances in computing technology enabling higher-fidelity numerical simulations than previously possible, such as Large-Eddy Simulations (LES) [32], the computational cost of such simulations remains prohibitive for widespread design use [32, 33]. Instead, empirical models have been found to be effective in capturing and predicting the physical behaviours that lead to thermoacoustic oscillations in gas turbine combustors [32-34].

A flame transfer function (FTF) is a systems-based model that accounts for the response of a flame to velocity perturbations at a given frequency [35-39]. Existing works [35-42] have performed measurements to obtain FTFs and used them to explore the dynamics of various combustor designs. As Moeck *et al.* [37] note, FTFs effectively assume that oscillations only interact one-to-one at the same frequency.

Conventionally, the FTF is defined as the ratio of the complex amplitudes of the heat release rate, denoted by $\hat{\dot{q}}(\omega)$, and forcing velocity, $\hat{v}$, for a velocity disturbance of the form $v' = \sin \omega t$. Mathematically, this is expressed as

$$FTF(\omega) = \frac{\hat{\dot{q}}(\omega)}{\hat{v}(\omega)} \tag{2}$$

Note that the complex amplitudes can be taken to be the Fourier coefficients from the first-order Fourier expansions [37, 39]. This formulation makes several assumptions: (i) the oscillations are harmonic, (ii) the perturbations are at a single frequency, (iii) the flame responds only at the frequency of the perturbations, (iv) the response is independent of the amplitude of the perturbations [35, 36, 39]. The assumption of harmonic oscillations

(*i.e.*, that the solution is a linear superposition of independent modes) renders the FTF approach incapable of resolving complex dynamics such as some transients, bifurcations and transitions to chaos [37].

As Moeck *et al.* [37] and Haeringer *et al.* [39] note, experiments or numerical simulations of a flame subjected to external forcing at a single frequency can be used to evaluate the FTF. Such studies involve a sweep of various forcing frequencies and amplitudes while holding the mean operating conditions constant. After computing the FTF from such data, the FTF is incorporated in numerical models to handle how the flame responds to the natural acoustic modes in a feedback loop, as illustrated in Figure 4.

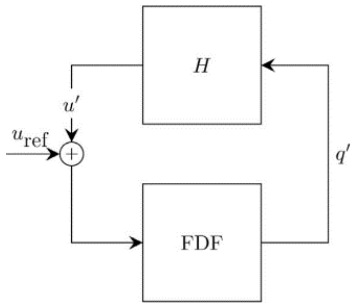

Figure 4: Thermoacoustic FDF model block diagram. "H" models the linear acoustic response to heat release perturbations [45].

Recent works [37, 39, 40, 42-45] have demonstrated that the effects of frequency interactions can be significant in practical gas turbine combustors and can confound FTF-based models if their effects are not included. Frequency interactions have been observed and analyzed in various systems since the 1600s, such as in pendulum clocks [46, 47], music and acoustics [48], neuroscience [49] and thermoacoustics [50]. The work by Moeck *et al.* [37] explores how multiple oscillatory modes can interact with each other and explores how a multi-input FTF can account for the interactions of various modes. Their

theoretical analysis reveals that single-input FTFs can fail to properly describe the stability of any single mode in a multi-modal system [37]. Despite the improvements offered by the multi-input FTF, it is impractical for anything beyond two modes [37]. Overall, there is a clear need to include the effects of frequency interactions in FTF methods.

1.3.3 Frequency interactions

Under the umbrella of nonlinear dynamical systems theory, synchronization theory [51, 52] and nonequilibrium dynamics and pattern formation theory [53] offer a mature framework for explaining and analyzing frequency interactions. The limitations of FTF methods highlight how oscillations at various frequencies can interact and yield dynamics that differ from predictions using linear analyses. Of particular importance are the frequency interactions related to synchronization phenomena. Entrainment is one example, wherein the oscillations at one frequency are drawn towards those at another frequency. Synchronization occurs when the two frequencies become *commensurate*. Mathematically, two frequencies f_1 and f_2 are commensurate if their ratio can be expressed as a rational number, *i.e.*, $f_1/f_2 = m/n$, where m and n are integers. The ratio of two commensurate frequencies is also known as the harmonic ratio and is frequently denoted by $m{:}\,n$. Conversely, *incommensurate* frequencies are those whose ratio is an irrational number.

The changes that occur en route to synchronization depend on the type of oscillation, the nature and directionality of the coupling, the separation in natural frequencies and the strength of the coupling. The coupling between two oscillations can be either bidirectional (mutual) or unidirectional (as in forcing). In forced synchronization, a self-oscillator is subjected to an externally driven forcing. Obviously, such forcing is independent of the self-oscillator, but what differentiates the combined system from driven

oscillations (like in resonance) is that the frequency and amplitude of the natural dynamics depend on the frequency and amplitude of the forcing. The strength of the coupling is proportional to the forcing amplitude F [51]. Except for infinitesimal forcing amplitudes, which yield a linear superposition of unforced and forced solutions, any applied forcing will interact with the observed unforced frequencies [51].

In mutual synchronization, the external forcing is replaced with another self-oscillator, and thus the frequencies and amplitudes of both oscillators depend on each other. In this case, there are two coupling strengths: B_{D} for dissipative coupling (damping) and B_{R} for reactive coupling (also called time-delay coupling) [51]. For complex systems like gas turbine combustors, mathematical expressions for B_{D} and B_{R} cannot usually be derived. However, changing B_{D} and B_{R} has different qualitative effects on mutually coupled oscillations which can be used to differentiate their influence in experimental results [51]. The remainder of this discussion focuses on forced synchronization given its relevance to FTF measurements. Mutual coupling will be mentioned where necessary.

The degree of synchrony achieved in a system of coupled oscillators depends not only on the coupling strength, but also the separation in natural frequencies. The separation in frequency, called frequency detuning (Δf), is measured with respect to the nearest harmonic ratio and is given by

$$\Delta f = mf_2 - nf_1 \tag{3}$$

where m and n are the integers of the harmonic ratio. Thus, for a forced system with $(\Delta f, F)$, there are three possible system states: (i) unsynchronized and coupled oscillations; (ii) phase synchronized or phase-locked oscillations; and (iii) suppressed dynamics. The parameter space over which synchronization occurs for harmonic ratio $m{:}\,n$ is roughly V-

shaped, as illustrated schematically in Figure 5. The synchronization region is also known as an Arnold tongue. The width of the Arnold tongues decreases as m and n increase in the harmonic ratio (*e.g.*, the 1:1 tongue is the largest, while the 3:2 tongue is larger than the 21:5 tongue). Crossing the solid or dashed lines in Figure 5 causes the system to undergo a saddle-node or torus-birth bifurcation, respectively. Ref. [51] describes other kinds of bifurcations related to synchronization.

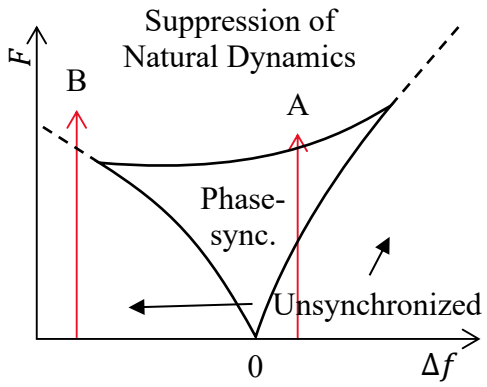

Figure 5: Schematic representation of *m:n* forced synchronization region. Arrow A denotes the phase-locking route; B denotes the suppression route.

The red arrows in Figure 5 illustrate two possible routes to synchronization for a given Δf. Arrow A lies along the phase-locking route, which occurs for relatively small Δf. Increasing from $F = 0$, the observed frequency of the oscillator f_o is pulled towards the forcing frequency f_f until they become commensurate. Once this occurs, the system is phase-locked and the phase difference between the oscillations becomes invariant in time [51]. The amplitude of the 'natural' dynamics does not change. In a mutually coupled system, both natural frequencies change as either coupling strength (B_D or B_R) increases. Dissipative coupling pulls both frequencies to the nearest harmonic ratio while reactive coupling causes both to increase until the slower frequency 'catches' the faster one [51].

Arrow B in Figure 5 denotes the suppression of natural dynamics route, which occurs for values of Δf larger than those for the phase-locking route. Increasing the forcing amplitude along this route has little effect on the frequency of the 'natural' dynamics. Instead, the amplitude of the natural oscillations decreases to zero as the response at the forcing frequency increases. Synchronization is achieved once the amplitude of the natural dynamics vanishes. For mutual coupling, the system undergoes oscillation death (also called amplitude quenching [54, 55]) instead of suppression, wherein the amplitudes at both frequencies vanish for a range of coupling strengths before restarting in a synchronized state [51, 56].

Another interesting feature of synchronization is that it is not limited to coupling between frequencies. Phase-locking in particular has three general forms, as illustrated in Figure 6 below. Phase-phase synchrony (Figure 6a) is the general form where the phases of the oscillations lock onto each other. Phase-amplitude synchrony (Figure 6b) is when the amplitude envelope of one oscillator phase-locks with the oscillation phase of the other. This produces an amplitude modulation at the same frequency as the other oscillator. Amplitude-amplitude synchrony (Figure 6c) is similar to phase-phase synchrony, but the phase-locking occurs between then amplitude envelopes of the two oscillations and the frequencies are not necessarily related.

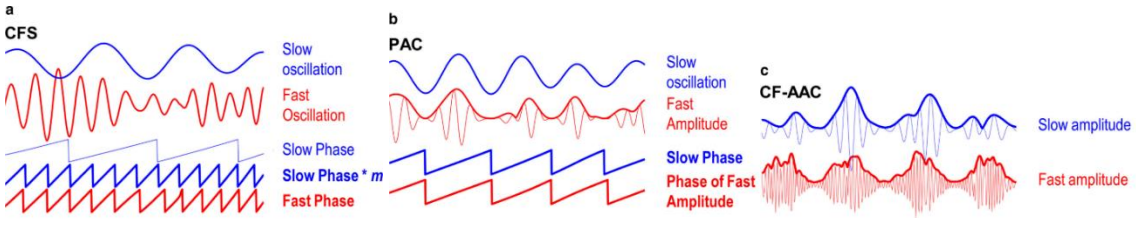

Figure 6: Types of synchronization; (a) Cross-Frequency Synchrony (CFS), (b) Phase-Amplitude Coupling (PAC), (c) Cross-Frequency Amplitude-Amplitude Coupling (CF-AAC) [57].

These observations apply to an ideal case without noise and examining only two unimodal oscillations. The effects of inharmonicity, multistability, noise and chaos can obfuscate the observations described above and alter the routes to synchronization [51]. First, it is important to understand the role of inharmonicity in nonlinear frequency interactions. Perfectly harmonic (sinusoidal) oscillations tend to operate independent of other frequencies [48]. Real oscillations are rarely perfectly harmonic and their inharmonicity enables the crosstalk of various frequencies within a single oscillator [51]. The excitation of sub- and super-harmonic frequencies is one example [43]. Second, overlapping Arnold tongues can result in multistable states where mode switching can occur [52]. Third, noise can have several interactions with coupled oscillations. In general, however, noise can disrupt synchronization and induce coherent behaviour at the natural frequency (rather than at the synchronized frequency) [51]. Finally, if the natural oscillations are chaotic, the coupled interactions become significantly more complex and depend on the geometry of the underlying chaotic attractor as described in Ref. [51].

The significance of frequency interactions and synchronization phenomena in practical gas turbine combustors is reflected in the growing interest on related research in the combustion literature. Many works [54, 56, 58-63] have demonstrated the universality of nonlinear dynamical systems theory, including various routes to synchronization and chaos. The results of Bellows *et al.* [41] indicate the presence of 3:2 synchronization in a gas turbine combustor, although it is not analyzed specifically. The works of Guan *et al*. [60, 61, 64] and Kashinath *et al*. [63] show the versatility of nonlinear time series analysis and the effects of cross-frequency coupling as related to various synchronization phenomena in the presence of forcing. More recent research efforts [44, 56, 58, 62, 65]

have explored the effects of mutual coupling between dynamics at various frequencies. The experiments performed by Balusamy *et al.* [40] and Guan *et al.* [60] explore how the presence of mutual coupling between self-excited thermoacoustic modes alters the response of a system to forcing. Guan *et al.* [60] note that the forcing must overcome the mutual coupling to achieve forced synchronization. Balusamy *et al.* [40] and Hochgreb *et al*. [42] note that experiments for FTF measurements must account for frequency interactions to provide reliable models of the flame response. These observations illustrate how the forced response of a system is fundamentally different from the response of the same system to self-excited dynamics with the same frequency as the forcing. With few exceptions, however, these studies are limited to either operation at atmospheric pressure or with gaseous fuels. The high-pressure and high-power conditions experienced in practical gas turbine combustors exhibit richer and more complex dynamics than what has been studied in existing experiments.

1.4 Research Objectives

The research presented in the literature highlights the lack of existing experimental data for LPP gas turbine combustors operating at conditions relevant to CST applications. This lack of data is multifaceted in that there is a gap in the knowledge of blowoff limits and behaviour and forced flame response in such combustors. In addition, the interactions between multiple combustor elements or flames are not well understood. Together, there are three areas of potential viability issues with LPP combustors at CST conditions:

1. Pollutant emissions at CST operating conditions.
2. Robustness and operability limits of LPP combustor designs.

3. Prediction of flow and flame interactions involving neighbouring combustor elements in multi-element designs.

The first issue arises from the lack of empirical data to show that combustor designs can meet future emissions regulations, as discussed in Section 1.1. This also plays into the second issue with operability limits, in that CST combustors must operate reliably over a wide range of conditions, from ground idle to supersonic cruise at high altitudes. Furthermore, while LPP combustors have been tested in the past, they do not operate well at subsonic conditions. As part of reliable operation is the ability to prevent unwanted oscillatory dynamics over the range of operating parameters for CST combustors. The influence of multiple, distinct combustor elements and flames complicates the prediction of combustion dynamics.

Each of the three viability issues can be resolved with an experimental characterization of a practical combustor design operating at CST conditions. Thus, the main objectives of this work are to experimentally:

- Identify mean flow features and dynamics of a multi-element LPP combustor.
- Determine blowoff limits and relevant physical effects, particularly the influence of neighbouring combustor elements.
- Analyze the forced flame response and interference from frequency interactions.
- Provide empirical data for validating existing models for combustion dynamics.

CHAPTER 2

EXPERIMENTAL APPROACH

Experiments were performed on optically accessible, high pressure, model lean premixed pre-vaporized (LPP) aeronautical gas turbine combustors at GE Research in Niskayuna, NY. Two data collection campaigns were conducted, focusing on basic combustor characterization for the first campaign in 2021 and on forced response and flame dynamics in 2022. While different pressure vessels and test cells were used in each campaign, the combustor dome face is same design with differences described below.

2.1 Test Rig

2.1.1 Campaign 1 (2021)

Figure 7 shows the facility used for the experiments in the first campaign (Campaign 1, 2021) and the layout of the optical diagnostics. Figure 8 shows a schematic of the combustor dome face, which consists of four, premixed, bluff-body stabilized "main" flames surrounding a central, premixed, swirl-stabilized pilot flame. Each main flame operates at fuel-lean conditions, burning partially pre-vaporized and premixed Jet-A fuel. For the laser diagnostics described below, the laser sheet passed through the centers of the mains on one side of the combustor as indicated in Figure 8 by the solid green line.

For the various diagnostics employed in Campaign 1, quartz windows were employed for the side walls and the top wall of the combustor section. The combustor bottom wall was a water-cooled window-blank with ports for ignitor and three dynamic

pressure sensors. The downstream tail pipe consisted of a water-cooled constant cross-section liner with ports for dynamic pressure sensors.

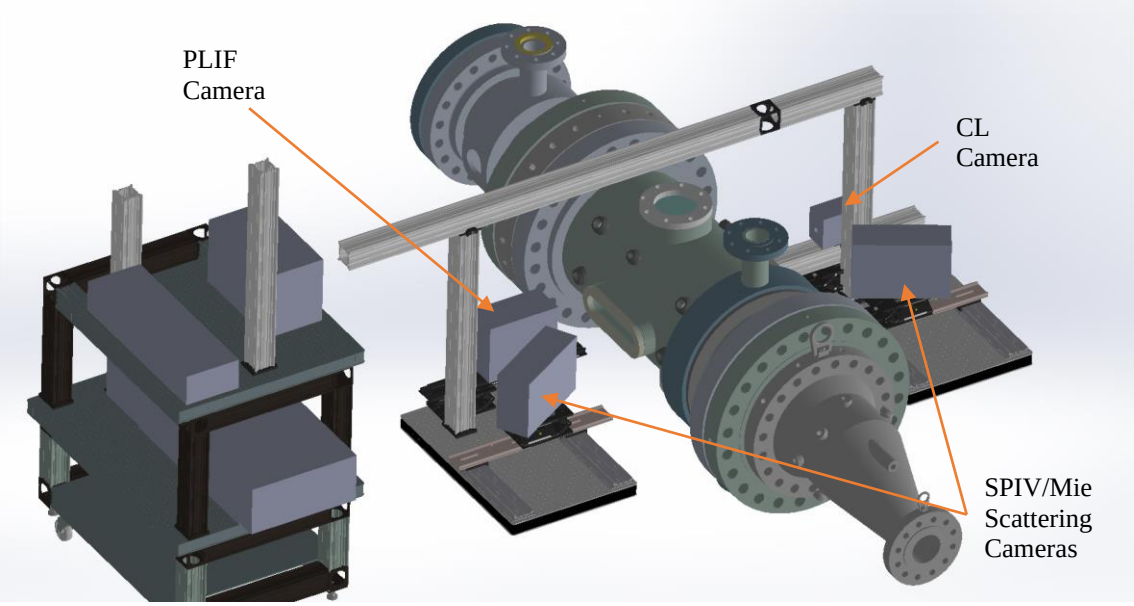

Figure 7: Campaign 1 test cell schematic with optical diagnostics.

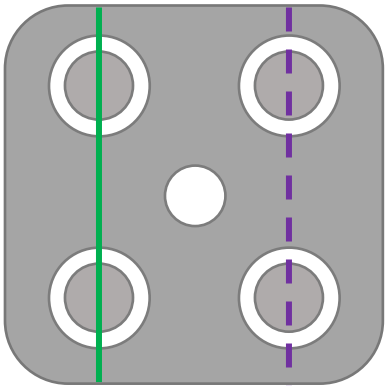

Figure 8: LPP style combustor dome geometry with laser sheet positions for Campaigns 1 and 2 indicated by solid green line and dashed violet line, respectively.

The rig is supplied continuously with high pressure preheated air for combustor and cooling needs. Liquid Jet-A fuel is injected into the combustor through three lines, with

one of these lines dedicated for fueling the pilot. The other two fuel lines separately feed the top and bottom fuel circuits of the premixer for the main injectors. Within the mixer are discrete fuel injectors arranged azimuthally. The angular positions of these injectors were not necessarily identical between each of the mains. A torch ignitor is located inside the combustor to ignite the fuel-air mixture. All air, fuel and water flows to the test rig are individually metered and controlled.

2.1.2 Campaign 2 (2022) modifications

While a different test facility and pressure vessel were used for the second campaign (Campaign 2, 2022), the test article, shown in Figure 9, is based on the design studied in the previous experimental campaign [66]. The different facility required a slightly different diagnostic layout than in Campaign 1 (Figure 7) but the layout was similar enough that is has been omitted for brevity. The combustor test article consists of an LPP dome, square optical liner and a constant area tail pipe section. The optical liner was changed to be square for this campaign to better mimic the aspect ratio of gas turbine combustors currently employed in industry. A constant area hot section was chosen to eliminate any combustor back-projection uncertainties of the acoustic pressure from the downstream multi-microphones. The test article design was based on GE's existing THOR optical liner design that was successfully employed over the last 8 years for various optical and laser diagnostics efforts for aero-engine studies [67].

A water-cooled orifice plate, located at the end of the tail pipe section provided the necessary acoustic boundary condition to suppress self-excited combustor tones. The dimensions of this orifice plate were sized based on the predicted rig tones and designed to

survive the thermal loading. This plate was added to the test article for Campaign 2 to eliminate potential interactions between the external forcing and self-excited dynamics.

The rig is supplied continuously with high pressure preheated air for combustor and cooling needs. Typical combustor air flow ranges from 0.2-0.4 kg/s and vessel cooling bypass air is provided at about 0.4 kg/s at 600 K. The test facility also features a topping heater that can potentially increase the air temperature delivered to the rig. Three liquid Jet-A lines supply fuel to the combustor. One of the three fuel lines supplies the fuel to the pilot. The other two fuel lines feed the top and bottom fuel circuits for the main mixer. A torch ignitor is located inside the combustor to ignite the fuel-air mixture. All the air, fuel and water flows to the test rig are individually metered and controlled.

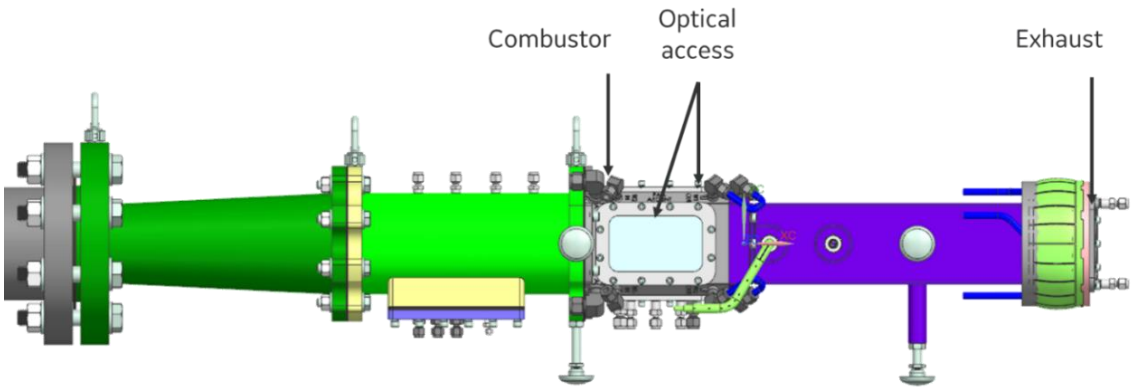

Figure 9: Profile view of Campaign 2 experimental test article.

A siren device is employed to modulate the frequency of the air sent to the premixer. By varying the RPM of the electric motor to the siren device the modulation frequency can be tuned from 1-1,050 Hz. The forcing amplitude is controlled through the split between the combustor air that flows through the siren versus through a bypass. In general, higher mass flow through the siren results in higher forcing amplitude. The forcing amplitude is dynamically changed by bypassing the flow to the siren and mixing the bypassed

(unforced) flow with the forced flow downstream of the siren and upstream of the premixer. The forcing amplitude is monitored and set using dynamic pressure sensors located upstream of the premixer.

2.2 Test Conditions

In both campaigns, the experiments were performed at a range of conditions relevant to CST operation. Nominal cruise conditions for CST applications involve higher T_3 and lower P_3 than found in conventional subsonic aircraft engines. The design of the experimental rig enables independent control of T_3, P_3 and pilot and main equivalence ratios, with the siren from Campaign 2 enabling sweeps of forcing frequency (f_f) and forcing amplitude (F). The variation of mixer equivalence ratio provides control over the combustor exit temperature (T_4). Campaign 1 focused on exploring the operating parameter space for CST engines (P_3, T_3 and FAR sweeps). Campaign 2 used a reduced parameter space from Campaign 1 to explore the forced flame response with the siren device.

The conditions analyzed from each campaign are summarized in Tables 1 and 2. These tables present the nominal values of each parameter, but the actual conditions varied slightly between test points (TP), indicated by the standard deviations for each nominal value. Note that for T_3 in Campaign 1, a range of values is provided instead of nominal values. The tables also provide the relative uncertainty, taken as the statistical uncertainty over the recording time for one TP. Prior to data acquisition, the combustor was allowed to settle to steady state as verified by examination of static pressure, thermocouple and mass flow rate measurements. For Campaign 1, $\dot{m}_{air}$ is proportional to P_3, such that its nominal values are uniquely based on P_3 (i.e., did not sweep $\dot{m}_{air}$, only P_3).

Table 1: Campaign 1 nominal test conditions with variations and uncertainties.

Parameter	Nominal Value(s)	Standard Deviation	Relative Uncertainty (%)
Reactant Pressure, P_3 (kPa)	788, 1027	15	0.2%
Reactant Temperature, T_3 (K)	640-720	N/A	0.07%
Total Equivalence Ratio, φ	0.54, 0.59, 0.66, 0.74	0.07	0.9%
Pilot Equivalence Ratio, φ_p	1.2	0.2	0.002%
Total Air Mass Flow Rate, $\dot{m}_{air}$ (kg/s)	0.165, 0.215	0.006	0.3%

Table 2: Campaign 2 nominal test conditions with variations.

Parameter	Nominal Value(s)	Standard Deviation
Reactant Pressure, P_3 (kPa)	797	9
Reactant Temperature, T_3 (K)	560	5
Total Equivalence Ratio, φ	0.59, 0.66, 0.73	0.01
Pilot Equivalence Ratio, φ_p	1.05	0.07
Total Air Mass Flow Rate, $\dot{m}_{air}$ (kg/s)	0.195	0.004
Forcing Frequency, f_f (Hz)	0, 300, 500, 670, 900	1

2.3 Diagnostics

Several diagnostics were employed over both campaigns focused on measuring the heat release rate, fuel-air mixing, combustor emissions, pressure dynamics and gas phase velocity. Campaign 1 involved simultaneous chemiluminescence (CL) electronically excited hydroxyl (OH*), fuel planar laser induced fluorescence (PLIF) and pressure measurements, with some fuel droplet Mie scattering. Campaign 2 added stereoscopic particle image velocimetry (SPIV), which was simultaneous with the OH* CL, but mutually exclusive with the fuel PLIF. Due to the operations and some data acquisition issues, not all measurements are available at every test condition.

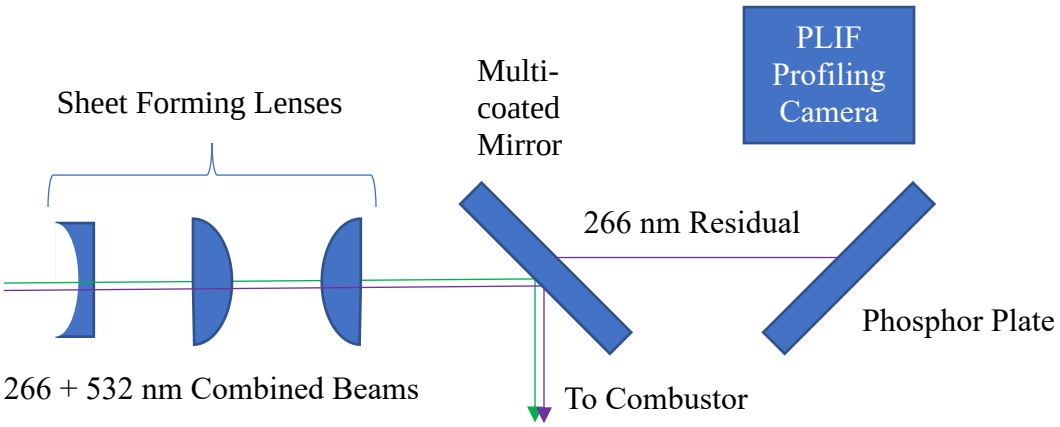

Figure 10: Side view of beam forming optics and PLIF laser profiling components.

2.3.1 OH* chemiluminescence

Chemiluminescence is the light emitted by electronically excited species as they return to the electronic ground state. Different chemical species emit different wavelengths of light, which can be filtered for individual detection by a camera. Each chemical species occurs at different points in the combustion process and so will appear with different positions and concentrations relative to the flame. In addition, the concentration and distribution of chemical species depends on the local equivalence ratio [68, 69].

It is known that, at a particular equivalence ratio, the intensity of the light emitted by certain electronically excited chemical species is related to the amount of heat released [69]. When the equivalence ratio is constant throughout a laminar flow, the relationship between the emitted intensity of light and the heat released is constant, and so chemiluminescence measurements provide temporal and some spatial information on the heat release rate. Unfortunately, even in such simple situations, the amount of spatial information extractable from chemiluminescence data is limited by the fact that the signal is integrated along the line-of-sight [69]. For partially-premixed turbulent flames, such as

those typical of liquid-fueled gas turbine combustors, the local equivalence ratio varies based on the level of mixing between the fuel and air, influenced by the turbulence in the flow, and other local flame properties [68].

Electronically excited hydroxyl (OH*) CL is commonly employed as a surrogate metric for heat release rate [31, 68-71] since OH* emits much of the CL in lean premixed hydrocarbon flames [69, 71]. In addition, OH* forms alongside CO in equal molar ratios [72, 73], and a majority of the heat release occurs during the oxidation of CO by OH for alkanes [7]. OH* CL is emitted mainly around wavelengths of 309 nm [71], but it is still important to quantify the contribution of the broadband chemiluminescence from triatomic and larger species [71]. Turbulence also reduces the intensity of chemiluminescence emission by influencing the local strain rate and flame curvature [71, 74, 75].

OH* CL imaging at 308 ± 5 nm served as the metric for line-of-sight integrated heat release rate measurements. Previous experiments [31, 44] and wide-spectrum measurements from a portable spectrometer (Ocean Optics HR2000) showed that OH* is the most appropriate indicator of heat release rate in the LPP style combustors analyzed in this work. A sample spectrum is shown in Figure 11 with the peak corresponding to OH* emissions indicated. As studies [69, 76] have shown, OH* CL provides only a qualitative metric for heat release rate. It can, however, serve as a qualitative indicator of flame structure [69] even for complex flame topologies such as the one examined in this work.

During Campaign 1, CL images were recorded at 10 kHz using a high-speed camera (Photron SA-5) coupled to an image intensifier (Invisible Vision UVi 2550B-10, gate time of 30-50 μs), commercial objective lens (Nikkor 105 mm UV, f/# = 11) and bandpass filter (312 ± 12.5 nm).

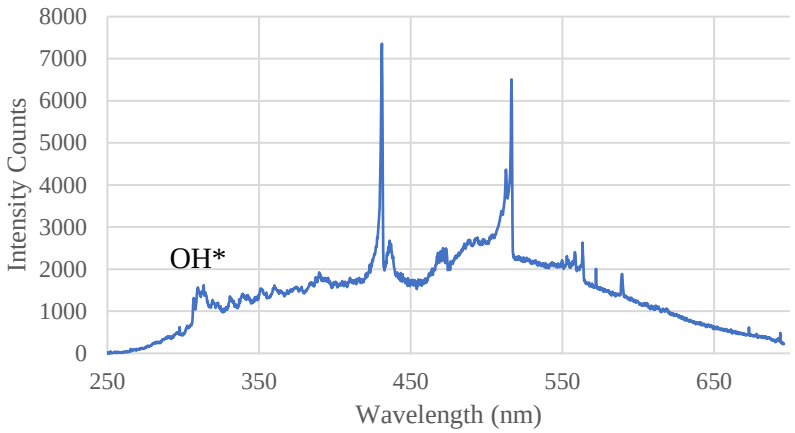

Figure 11: Sample spectrometer readings with OH* peak indicated.

During Campaign 2, the intensifier was a different model (Invisible Vision UVi 2550-10) with a fixed gate time of 20 µs, the objective lens was changed to a Cerco 100 mm (f/# = 2.8) and the filter was updated (Invisible Vision 308 ± 10 nm). In both campaigns, the camera recorded 7,534 frames per test point.

To start, a flatfield correction was applied to the CL images (only for Campaign 2). The flatfield correction eliminates silhouetting and any spatial variations caused by nonuniformities of the camera sensor. The flatfield is computed as the average of a series of images taken by each camera of a uniformly lit white plate. One flatfield was generated for each intensifier gain setting used in the experimental campaign. Next, the CL images were cropped to the visible area inside the combustor and then 2×2 binned to reduce computational cost and improve the signal-to-noise ratio. When required, the CL data could be temporally downsampled to the same frequency as the SPIV images by selecting every second frame from the data set. The first matching frame was determined from the camera exposure signals recorded by the DAQ (see Section 2.3.5 for more information).

2.3.2 Kerosene fuel planar laser induced fluorescence (PLIF)

The spontaneous emission of radiation by an excited chemical species as it returns to a lower energy level is called fluorescence [77]. Planar laser-induced fluorescence (PLIF) targets specific species based on the wavelength of the laser and the resulting fluorescent emissions occur over a planar region of space, enabling 2D analyses. Fundamentally, the intensity of PLIF emissions is proportional to both the input laser intensity and the concentration of the target species [77]. Performing quantitative PLIF measurements—to obtain absolute species concentrations—requires rigorous calibrations that are often not possible when applied to practically-relevant gas turbine combustor operating conditions [78]. It is possible to perform relative comparisons of PLIF intensities, yielding qualitative assessments of species concentrations. One of the goals of this thesis is to assess the fuel-air mixing of an LPP combustor and detect conditions where flame blowoff occurs. As such, qualitative PLIF is sufficient for this task.

Qualitative measurements of the fuel mixing behaviour were obtained via PLIF of the aromatic species naturally present in the Jet-A fuel. The study by Orain *et al*. [79], explains the various compounds that contribute to kerosene PLIF and the effects of combustor operating conditions on the PLIF signal. Importantly, Orain *et al*. note that the high temperature in the flame (regions above ~1,100 K) causes aromatic pyrolysis which results in the PLIF signal existing only in the reactants, upstream of the flame [79]. Thus, kerosene PLIF denotes the planar regions of unburned reactants in a combustor flow.

Optical layout

The flow was illuminated at a repetition rate of 10 Hz using the fourth harmonic (266 nm) output of a Nd:YAG laser (Spectra Physics Quanta-Ray PRO 350). The beam was formed

into a sheet via a three cylindrical-lens telescope and oriented perpendicular to the combustor dome face such that the laser sheet bisected the top and bottom mains on one side of the combustor.

PLIF signal was collected using an intensified camera (Andor iStar sCMOS, gate time of 100 ns) with an objective lens (Nikkor 105 mm UV, f/# = 4.5) and a two-filter setup consisting of a bandpass (340 ± 40 nm) and a steep-edge long wave pass filter (325 ± 3.5 nm). This filter setup was chosen to align with the center of the fluorescence spectrum of kerosene vapor [79] while blocking signal from OH* CL. In both campaigns, the camera recorded 1,000 frames per test point.

Signal corrections

While the fuel PLIF measurements ultimately require only qualitative data, a series of corrections were applied to increase the fidelity of the results and reduce noise. Noise sources include: (i) thermal noise, corrected via camera cooling and darkfield calibration; (ii) background noise from flame CL and laser scattering, corrected via background subtraction; (iii) nonuniform pixel sensitivity, corrected via whitefield calibration; (iv) shot-to-shot laser energy and profile variation, corrected via simultaneous measurements and normalization; and (v) laser energy absorption along the propagation direction, corrected via semi-empirical models. Figure 12 illustrates the PLIF correction process.

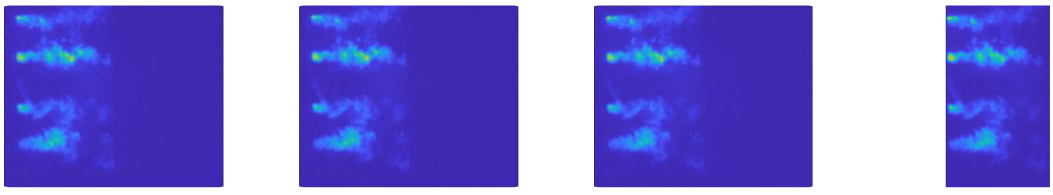

Figure 12: Fuel PLIF signal correction process with samples.

For thermal noise and background subtraction, each data set was collected twice: once with the laser running ("active" set) and once without ("dark" set). The mean of the "dark" data set provides the simultaneous darkfield and background subtractions for instantaneous PLIF images. Whitefield calibrations were performed after each campaign for each intensifier gain value used in that campaign. The whitefields were computed as the average of a set of images of a uniform, back-lit, diffuse LED panel.

Simultaneous shot-to-shot beam profile measurements were made by imaging a cuvette filled with a rhodamine dye solution. The cuvette was placed at the location of the beam waist along the path of residual transmission from the 266 nm sheet through the final mirror above the combustor. This low intensity copy of the sheet within the combustor caused the dye solution to fluoresce at visible wavelengths, which was then imaged with a separate camera system (FLIR Blackfly USB3). For the data from Campaign 1, no correction was made for absorption of laser power through the domain or fluorescence quenching.

For Campaign 2, the fuel PLIF correction system was improved. Given the issues encountered with the rhodamine dye solution evaporating from the cuvette over time, the cuvette was replaced with a phosphorescent plate that responds similarly to rhodamine when excited by UV laser light. To eliminate the interference from any residual 532 nm light that passed through the final mirror and scattered off the phosphor plate, the Blackfly camera was equipped with a coloured glass filter to block 532 nm light and pass only the phosphorescence (which was ~660 nm). These improvements enabled corrections for shot-to-shot laser sheet intensity and profile variations and laser power absorption through the combustor.

2.3.3 Fuel spray laser Mie scattering

Mie scattering is the form of light scattering most present for particles whose diameter is above, but similar to, the wavelength of the incident light. The main characteristic of Mie scattering is a varying scattering intensity with respect to viewing angle, with the peak in the forward direction (relative to the incident light propagation) and the minimum in the backwards direction [80]. Increasing the size of the scattering particle also affects the magnitude of the scattered light intensity for the same wavelength of incident light [80].

Unfortunately, quantitative relations between Mie scattering intensity and particle properties are challenging due to several confounding factors such as the simultaneous influences of viewing angle, particle properties and incident light intensity [80]. Nevertheless, Mie scattering can be used for qualitative descriptions of a flow. The raw Mie scattering images can provide an instantaneous snapshot of an atomized fuel spray, for example, for a qualitative assessment of the distribution of droplets and the shape of the jet. The images can be used in other techniques as well, such as particle image velocimetry (discussed in Section 2.3.4) for more quantitative results.

In this work, the fuel Mie scattering provides a qualitative metric for the amount of liquid fuel that enters the combustor and the spray penetration depth. It is also used for spectral analysis of the fuel spray, indicating the frequencies of related oscillatory modes.

Optical layout

For Campaign 1, the Mie scattering was collected using a two-camera setup (Phantom v2640) with Scheimpflug adapters (LaVision), objective lenses (Tamron 180 mm, f/# = 8) and bandpass filters (532 ± 5 nm). Only one of the cameras was used for the analysis of the data because both cameras were qualitatively similar. The flow was illuminated at a

repetition rate of 10 Hz using the second harmonic (532 nm) output of a Nd:YAG laser (Spectra Physics Quanta-Ray PRO 350). Given that these measurements were simultaneous with the fuel PLIF, the 532 nm beam was obtained from the residual of the fourth harmonic generator. The 532 nm sheet used separate sheet forming optics from the 266 nm beam but had similar dimensions and orientation, with a beam waist of approximately 2 mm at the midplane in the test article. During Campaign 2, the fuel Mie scattering was collected at 10 kHz using the stereoscopic particle image velocimetry (SPIV) system described in Section 2.3.4. In both campaigns, the cameras recorded 8,096 frames per test point.

2.3.4 Stereoscopic particle image velocimetry (SPIV)

Particle image velocimetry (PIV) is a technique for determining the velocity field in a flow from a time series of particle images. These particle images are obtained by illuminating, with a laser formed into a sheet, a flow seeded with inert particles and imaging the light scattering from the particles. The size of these inert particles is chosen so that the particles will follow the structures in the flow. Typically, PIV yields a velocity field whose components are coplanar with the illuminated laser sheet, but there are multiple techniques for determining all three velocity components, or even reconstructing the full three-dimensional velocity field [80]. Stereoscopic PIV (SPIV) is a method of obtaining all three velocity components in a two-dimensional velocity field by imaging a laser sheet from two different angles on separate cameras. Besides reconstructing the out-of-plane velocity component, SPIV also reduces the error associated with normal (planar) PIV since the latter is technically a projection of a 3D velocity onto a 2D plane [80]. Velocity vectors are determined using a cross-correlation algorithm that identifies the average displacement

within an interrogation window by the location of the peak of the correlation between the intensities of the two single-exposure frames.

Deployment of SPIV for velocity measurements in gas turbine combustors commonly encounters several challenges. Ideally, seed particles would have the same density as the surrounding fluid to ensure proper tracking, but this is not possible in high temperature reacting flows, as most nonreacting seed particles for high temperature use are solid [67, 80]. The high velocity component perpendicular to the laser sheet in swirl-stabilized flames can cause loss of particles between frames, which biases the cross-correlation algorithm towards lower velocities. Thickening the laser sheet mitigates this, at the expense of spatial resolution in the normal direction. Natural flame CL and laser scattering off soot particles or liquid fuel droplets contribute to background radiation, lowering the signal-to-noise ratio in PIV images [31, 67]. Light scattering off the large droplets (relative to the seed particles) and reflections in the optical setup also reduce the signal-to-noise, potentially causing regions of complete signal loss due to sensor saturation [31]. While the effects of flame luminosity can be reduced using filters in the experimental setup, the effects of unwanted scattering and seed density fluctuations must be handled using image processing prior to generation of the vector fields [31]. It is also possible to reconstruct missing data in post using techniques such as gappy proper orthogonal decomposition (GPOD) [67].

Optical layout

To characterize the flow field inside the combustor during Campaign 2, a double-pulsed, two-camera stereoscopic particle image velocimetry (SPIV) setup was used at 5 kHz ($St = 0.95$). The complex 3D flow fields generated by the multi-element mixer design require

higher fidelity than possible with planar PIV, so SPIV was selected. A high-speed 532 nm Nd:YAG laser (Quantronix Hawk-Duo) illuminated the flow with pulse separation times varying between 5-7 μs and a laser sheet thickness of approximately 2 mm near the beam-waist. The laser sheet was coincident with the 266 nm beam used for fuel PLIF, oriented perpendicular to the combustor dome face. Mie scattering from nominally 1-3 μm ZrO_2 tracer particles that were seeded was collected into the two SPIV cameras (Phantom v2640), each equipped with 532 ± 5 nm bandpass filters, objective lenses (Tamron 180 mm, f/# = 11) and Scheimpflug adapters. The cameras recorded 4,049 pairs of frames for each test point.

While the tracer particles had too high of a Stokes number to track the small-scale features of the flow, they were sufficient to measure the larger-scale, thermoacoustically-coupled flow dynamics of interest here as shown in previous works [65, 81]. Vector processing was performed using a multi-pass algorithm with adaptive window shape and size and an iterative vector filter in commercial software (LaVision DaVis). Ref. [65] details the processing procedure, which is summarized in below.

Image preprocessing

Prior to processing or analyzing the Mie scattering data, the images were preprocessed to both correct the visual perspective and remove the background. For the perspective calibration and correction, LaVision's DaVis 8.4 was used with a pinhole camera model based on images taken of a LaVision 106-10 two-sided, two-plane calibration plate.

Due to the largely pre-vaporized nature of this combustor, few droplets were present in the combustor. This resulted in relatively low signal-to-noise in the Mie scattering data, which required considerable processing was required to extract meaningful information

about the residual fuel spray; Figure 13 illustrates the processing pipeline. First, a mask was applied to the images to exclude the regions where no droplets appear or regions outside of the laser sheet. All the images were then normalized to the same mean intensity to account for the variation in pulse energy across all frames. Subsequent processing using a temporal high-pass filter removed the quasi-static background associated with the flame and laser reflections. Finally, thresholding and image segmentation operations removed much of the leftover background noise that pass through the filter and identify the spray field in the combustor. A similar procedure was applied to the images used for SPIV prior to the vector calculation step, with step 3 in Figure 13 omitted.

Figure 13: Mie scattering image preprocessing workflow.

The different data sets (fuel droplet Mie scattering or gas velocity) require slightly different preprocessing steps and acquisition settings. For example, the higher laser power used to illuminate the seed particles in the gas velocity data resulted in saturated regions where fuel droplets were present. Such regions do not provide any valid velocity results and should be ignored in the computations. There also is a difference between the fuel spray and gas velocities, so any fuel droplets in a gas velocity data set must be removed. Removing the droplets prevents the vector calculation algorithm from being influenced by the droplet velocities in the vicinity of the main jet.

The removal of the fuel droplets and undesired image regions is accomplished by algorithmically masking each image in the data set. For gas velocity data sets, the droplets in the main jets and the regions outside of the laser sheet are masked out. It is only necessary to mask down to the laser sheet for nonreacting gas phase data sets because there are no droplets present.

With the mask applied, the background is removed from the image via a combination of a high-pass Butterworth temporal filter (7 frames in length) subtracted from each pixel and a 2D sliding spatial Gaussian average subtraction (11×11 pixels). An image threshold eliminated near-zero intensities and a 3×3 median filter then reduced image noise.

After preprocessing, the DaVis SPIV self-calibration procedure used the preprocessed particle images to correct the original manual calibration. One nonreacting gas velocity data set was collected each day for the self-calibration procedure, as they yielded higher quality particle images and thus higher accuracy calibrations. The self-calibration procedure is critical to the proper computation of the out-of-plane velocity component. If a self-calibration could not be performed, then no velocity fields were computed for that run day of the campaign. Once calibrated, the data sets typically had resolutions of approximately 19.7 pixels/mm.

Velocity vector processing

The vector processing itself uses a multi-pass algorithm with adaptive window shape and size and an iterative vector filter. Spurious vectors are identified and taken out of the vector fields using a median filter outlier detection algorithm built into DaVis. Any remaining gaps in a gas phase data set are filled using GPOD [67]. Regions in the field of view with

gappiness above 50% (when less than 50% of the snapshots have vectors at that spatial coordinate) were then masked out of the final vector fields because the GPOD results become less reliable. That is, there was insufficient data for the GPOD algorithm to effectively predict the missing data.

Issues with the particle flow seeding device caused all the gas velocity data sets in Campaign 2 to suffer from poor seed density. The low seeding density produced low confidence vectors across most of the vector fields, especially for reacting test conditions. For example, approximately 50-70% of the field of view for all reacting test conditions contains vectors that DaVis identifies as potential outliers. Applying a moderate strength outlier removal post-processing step eliminates these seemingly valid vectors, resulting in vector fields that are too gappy for GPOD. Since it was impossible to prevent the outlier removal from eliminating these vectors, many true outliers had to be left in the fields. As such, the vector fields were deemed suitable only for computation of mean velocities.

2.3.5 Pressure fluctuations

Pressure fluctuations were measured using dynamic pressure transducers (PCB), mounted to the ends of uncalibrated waveguides in a semi-infinite loop configuration, at three axial locations within the combustor. All three waveguides were constructed to have the same length and were adjusted so that their heated (the length inside the pressure vessel) and unheated (the length outside the pressure vessel) portions were also equal. As a result, the frequency-dependent attenuation and phase shifts induced by the waveguides on the acoustic data is the same. Thus, the three pressure signals from inside the combustor section can be compared directly. All three pressure measurements were qualitatively identical, thus the data from the middle transducer were used for subsequent spectral analysis.

A data acquisition system (National Instruments USB-6361) recorded the pressure and camera timing signals at a sampling rate of 100 kHz. By using the camera timing signals, it is possible to synchronize the pressure and image-based measurements *a posteriori* as follows. Pressure signals had any sensor drift removed via empirical mode decomposition (EMD). Following this preprocessing, the pressure data could be downsampled to the same acquisition rate as the image data sets. The downsampling was achieved by selecting the indices of the pressure measurements that fell within each of the corresponding camera exposure signals. The pressure could be averaged over the exposure, or the centre index could be taken as representative of that exposure. For the doubly pulsed SPIV data, the centre measurement was the one located in the middle of both pulses. A comparison of the approaches showed that both options produced nearly identical results. The pressure measurements centred in each camera exposure were used for the downsampling used in this thesis.

Due to crosstalk between DAQ units, there were several test conditions in both campaigns where the pressure signal became saturated. For those data sets, the pressure data was replaced by that recorded using GE's DAQ. GE's DAQ was a cRIO model running at 6 kHz over a much longer time interval (~20 s). GE's DAQ recorded pressure fluctuations from not only the combustor section, but also upstream of the mixer and within the tail pipe section. These measurements were used by GE to compute acoustic FTFs using the multi-microphone method. However, this pressure data was not necessarily recorded simultaneously with the data recorded on the other DAQ. GE's pressure data will be indicated wherever presented in this thesis.

2.3.6 Exhaust emissions

Combustor emissions were measured using an axially and radially traversable water-cooled probe. Several analyzers were used to detect unburned hydrocarbons (CAI model 600 HFID), CO/CO_2 (CAI model 603 NDIR) and nitrous oxide (CAI model 600 HCLD). Emissions measurements were only performed in Campaign 1.

CHAPTER 3

ANALYSIS METHODS

3.1 Computation of Reynolds & Damköhler Numbers

Much of the existing literature for bluff-body stabilized flames uses Damköhler (Da) versus Reynolds (Re) number correlations [22]. For the purpose of comparing the data in this thesis to previously reported data, an effort was made to use similar quantities and calculations, especially those presented by Shanbhogue *et al*. [22]. The Damköhler number is the ratio of flow to chemical timescales, τ_{flow} and τ_{chem} respectively:

$$Da = \frac{\tau_{\text{flow}}}{\tau_{\text{chem}}} \tag{4}$$

Following Shanbhogue *et al*. [22], τ_{chem} was computed from the unstretched laminar flame thickness, δ_{f}^{0}, and speed, S_{L}^{0}:

$$\tau_{\text{chem}} = \frac{\delta_{\text{f}}^{0}}{S_{\text{L}}^{0}} \tag{5}$$

with

$$\delta_{\text{f}}^{0} = \frac{T_{\text{prod}} - T_{3}}{\max {dT}/{dx}} \tag{6}$$

where T_{prod} is the temperature of the products behind the flame and T_3 is the temperature of the reactants. The temperature profile across the flame and S_{L}^{0} were computed via numerical simulation for each of the experimental conditions in Campaign 1. The derivative of the temperature profile was approximated via forward differencing from the simulation results. The details of the simulations are described in Section 3.2.

Again following Shanbhogue *et al*. [22], τ_{flow} was calculated from an empirical correlation for the laminar boundary layer momentum thickness, θ, and the speed of the reactants at the exit plane of one of the mains, v_{main}:

$$\tau_{\text{flow}} = \frac{\theta}{v_{\text{main}}} \tag{7}$$

with

$$\theta = \frac{35 d_{\text{bb}}}{\sqrt{Re}} \tag{8}$$

where d_{bb} is the diameter of the bluff-body and

$$Re = \frac{\rho_3 v_{\text{main}} d_{\text{bb}}}{\mu_3} \tag{9}$$

The reactant (mixture) density, ρ_3, is computed from the ideal gas law assuming completely vaporized fuel and perfect mixing of fuel and air at the measured FAR, T_3 and P_3. The mixed reactants of Jet-A (fuel) and air are treated as a binary mixture, with molecular weights W_{f} = 158.6 kg/kmol [82, 83] and W_{air} = 28.96 kg/kmol respectively. The reactant mixture dynamic viscosity, μ_3, was obtained from the same numerical simulations as δ_{f}^0 and S_{L}^0 (see Section 3.2).

To compute v_{main}, the mass flow around the annulus of the mains was assumed to be uniform and equally distributed across all four mains and the speed was calculated from the Continuity Equation in 1D:

$$v_{\text{main}} = \frac{\dot{m}_{\text{main}}}{\rho_3 A} \tag{10}$$

where $\dot{m}_{\text{main}}$ is the total mass flow rate through a single main injector and A is the area of the annulus with outer diameter d_{o} such that $A = \frac{\pi}{4}\left(d_{\text{o}}^2 - d_{\text{bb}}^2\right)$ and

$$\dot{m}_{\text{main}} = \frac{1}{4}\left[(FAR+1)\dot{m}_{\text{air}} - \dot{m}_{\text{f,p}} - \frac{\dot{m}_{\text{f,p}}}{FAR_{\text{p}}}\right] \tag{11}$$

In Eq. (11), $\dot{m}_{\text{air}}$ is the total air mass flow rate through the mixer, $\dot{m}_{\text{f,p}}$ is the fuel mass flow rate through the pilot, FAR_p is the fuel-air ratio of the pilot assuming the stoichiometric fuel-air ratio of Jet-A is $\text{FAR}_\text{st} = 0.068$. $\dot{m}_{\text{air}}$, $\dot{m}_{\text{f,p}}$, FAR and FAR_p were all measured during data acquisition.

The v_{main} calculation was validated with the mean SPIV results from Campaign 2. Campaign 1 data was used to compute the mean main-pilot air mass flow rate split and that was applied to Campaign 2 data along with Eqs. (10) and (11) to get v_{main}. At nonreacting and unforced conditions from Campaign 2, Eq. (10) gives $v_{\text{main}} \approx 65.3 \pm 0.4$ m/s, which is very close to the SPIV results of ~65 m/s near the dome face.

3.2 Chemical/Laminar Flame Speed Simulations

Numerical simulations to obtain μ_3, δ_f^0 and S_L^0 were performed in CHEMKIN using the laminar flame speed reactor model and the HyChem reaction mechanism [82, 83]. The HyChem mechanism uses formulation POSF 10325 for Jet-A fuel and assumes air is comprised of only 79% nitrogen and 21% oxygen [82, 83]. Parameter sweeps of P_3, T_3 and φ included all conditions recorded at during Campaign 1.

As described in Ref. [84], the mixture dynamic viscosity uses the semi-empirical formula from Wilke [85] and Bird *et al*. [86]. Figure 14 plots the computed values of μ_3 against T_3 for all the test conditions in Campaign 1. The vertical spread is due to varying FAR, such that increasing FAR causes a minor decrease in μ_3 for the same T_3. Note that the trend is linear, such that $\mu_3 \propto T_3$ over the range of parameters examined.

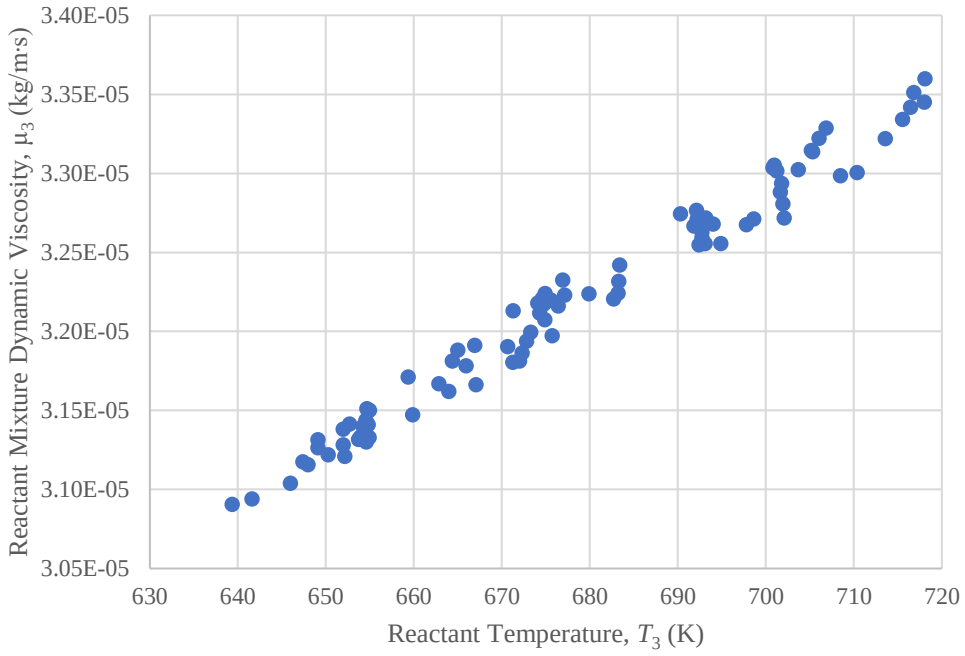

Figure 14: Simulated reactant dynamic viscosity VS temperature in Campaign 1.

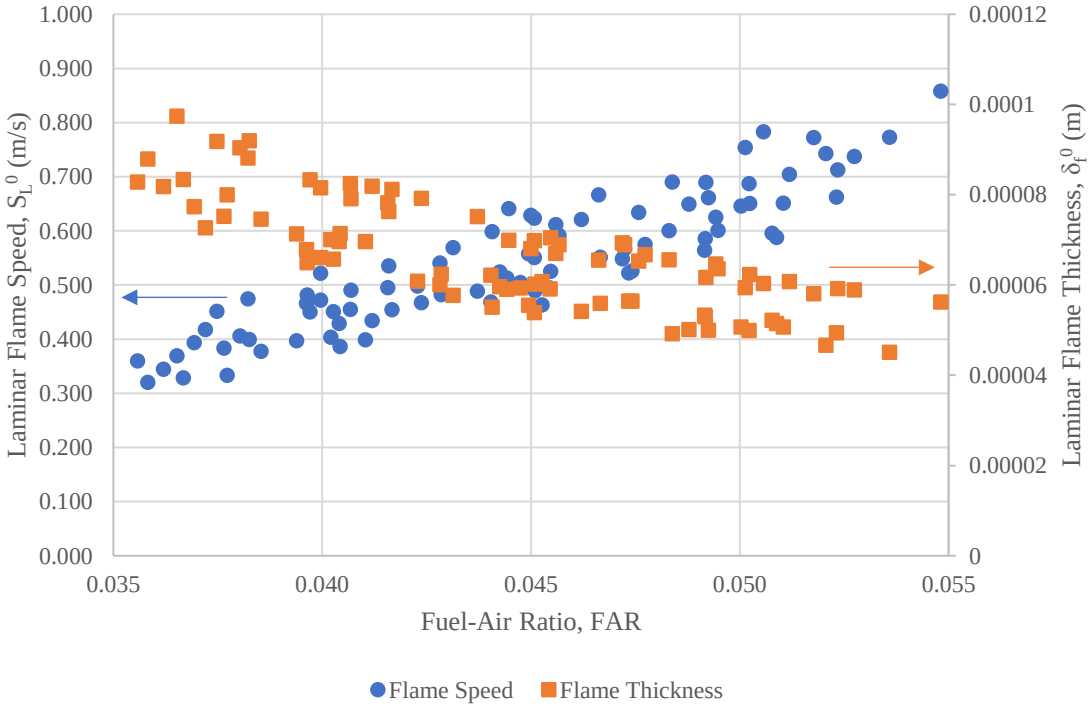

Figure 15: Simulated laminar flame speed and thickness VS FAR.

Figure 15 presents the trends in S_{L}^{0} and δ_{f}^{0} as FAR varies for all TPs in Campaign 1. The two distinct trendlines in δ_{f}^{0} are for low and high P_3, with variations in T_3 having minimal effect for a given FAR and P_3. The trend for S_{L}^{0} shows that while T_3 has a larger impact on S_{L}^{0} than δ_{f}^{0}, the impact of P_3 is lesser. The resulting trend in τ_{chem} using Eq. (5) is roughly linear such that $\tau_{\mathrm{chem}} \propto -FAR$, with variations in both P_3 and T_3 having minor effect over the range of conditions studies in Campaign 1.

3.3 Uncertainty Quantification

Applying standard uncertainty propagation formulae to Eqs. (4), (9) and (11) yields

$$\frac{\Delta Da}{Da} = \sqrt{\left(\frac{\Delta\delta_{\mathrm{f}}^{0}}{\delta_{\mathrm{f}}^{0}}\right)^{2} + \left(\frac{\Delta S_{\mathrm{L}}^{0}}{S_{\mathrm{L}}^{0}}\right)^{2} + \left(\frac{\Delta P_3}{P_3}\right)^{2} + \left(\frac{\Delta T_3}{T_3}\right)^{2} + \frac{1}{4}\left(\frac{\Delta\mu_3}{\mu_3}\right)^{2} + 4\left(\frac{\Delta d_{\mathrm{bb}}}{d_{\mathrm{bb}}}\right)^{2} + \left(\frac{\Delta Re}{Re}\right)^{2} + \left(\frac{W_{\mathrm{f}} - W_{\mathrm{air}}}{W_{\mathrm{f}} + W_{\mathrm{air}} FAR}\frac{\Delta FAR}{FAR}\right)^{2}} \tag{12}$$

$$\frac{\Delta Re}{Re} = \sqrt{\left(\frac{\Delta\dot{m}_{\mathrm{main}}}{\dot{m}_{\mathrm{main}}}\right)^{2} + \left(\frac{\Delta\mu_3}{\mu_3}\right)^{2} + \left(\frac{d_{\mathrm{o}}^{2} + d_{\mathrm{bb}}^{2}}{d_{\mathrm{o}}^{2} - d_{\mathrm{bb}}^{2}}\frac{\Delta d_{\mathrm{bb}}}{d_{\mathrm{bb}}}\right)^{2} + 4\left(\frac{d_{\mathrm{o}}^{2}}{d_{\mathrm{o}}^{2} - d_{\mathrm{bb}}^{2}}\frac{\Delta d_{\mathrm{o}}}{d_{\mathrm{o}}}\right)^{2}} \tag{13}$$

$$\Delta\dot{m}_{\mathrm{main}} = \frac{1}{4}\sqrt{(\dot{m}_{\mathrm{air}}\Delta FAR)^{2} + [(FAR+1)\Delta\dot{m}_{\mathrm{air}}]^{2} + \left(\frac{FAR_{\mathrm{p}} + 1}{FAR_{\mathrm{p}}}\Delta\dot{m}_{\mathrm{f,p}}\right)^{2} + \left(\frac{\dot{m}_{\mathrm{f,p}}}{FAR_{\mathrm{p}}^{2}}\Delta FAR_{\mathrm{p}}\right)^{2}} \tag{14}$$

where $\Delta(\cdot)$ represents the uncertainty of a quantity.

Given the results in Figure 14, applying uncertainty propagation suggests $\Delta\mu_3/\mu_3 \propto \Delta T_3/T_3$. Indeed, based on the formula for pure species viscosity in CHEMKIN [84], uncertainty propagation indicates that $\Delta\mu_3/\mu_3 \approx \Delta T_3/2T_3$ to first order. This was used for computing uncertainties in Eqs. (12) and (13).

Assuming a worst-case relative uncertainty of 2% for simulated quantities (δ_f^0 and S_L^0) and using statistical uncertainties for all measured parameters (P_3, T_3, FAR, FAR_p, $\dot{m}_{air}$ and $\dot{m}_{f,p}$) as indicated in Table 1 gives $\Delta Da/Da \approx \pm 3\%$ and $\Delta Re/Re \approx \pm 0.6\%$ on average across the entirety of Campaign 1. The worst-case uncertainty of 2% for δ_f^0 and S_L^0 is a very conservative estimate given the results in Figure 15. Specifically, propagating < 1% relative uncertainty in either P_3 or T_3 from Table 1 should yield < 1% relative uncertainty in τ_{chem}. This estimate does not account for systematic errors that could stem from differences in the formulation of POSF 10325 in the CHEMKIN model and the actual samples of Jet-A used in the experiments. The error bars for these quantities are included in the figures reported later in this thesis. However, those figures indicate that the uncertainty is negligible and thus does not require more rigorous modelling and quantification.

3.4 Detection of Blowoff

Given the exploratory nature of this research, it is important to identify the operating limits of an LPP combustor operating at CST relevant conditions. Of particular import are the lean blowoff (LBO) limits, which indicate the limits of several quantities before the flame can no longer remain stably attached within the combustor. The OH* CL and fuel PLIF were the only diagnostics capable of distinguishing between attached and blown off states. Figure 16 shows the temporally averaged OH* CL and fuel PLIF fields from the same day across different values of FAR.

For the fuel PLIF, blowoff was identified by the presence of any amount of PLIF signal directly behind the bluff body, as in Figure 16b-c. Figure 16a shows a clear example

of an attached flame, which is visually distinct from a blown off flame. The main drawback to using PLIF for blowoff detection is that it only works for the mains along the laser sheet. Given the multi-element design of this combustor, it is possible for only one of the mains to blow off while the others remain attached.

The OH* CL is much less robust for detecting blowoff. The first issue lies in the very short recording duration (~0.75 s VS 100 s for the fuel PLIF). Figure 16c shows a case where one of the mains blew off after the OH* CL images were finished recoding. As such, the OH* CL field shows a fully attached flame, while the fuel PLIF indicates blowoff. In cases such as Figure 16c, when the blowoff is intermittent, the OH* CL's short recording time makes it unreliable to identify whether the flame is primarily attached or blown off. The second issue arises from the fact that CL is line-of-sight integrated, meaning that if only one main blows off along the line-of-sight, it may not be reflected in the mean field correctly. Figure 16b is an example of a data set where both mains in line blew off, while both Figure 16a (confirmed during acquisition) and c are examples of fully attached flames. Comparing Figure 16a and c shows the local OH* CL intensity is not necessarily dependent on the flame attachment state. Overall, OH* CL is an unreliable indicator of blowoff, but it can provide additional information when paired with the corresponding fuel PLIF data.

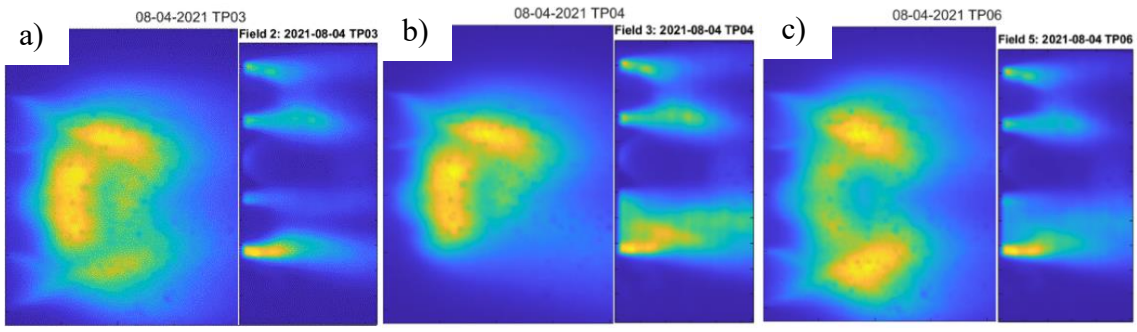

Figure 16: Temporal mean OH* CL and fuel PLIF (insets) fields for select conditions. (a) Da = 0.11, attached; (b) Da = 0.10, blown off; (c) Da = 0.13, blown off.

3.5 Spectral Analysis

To understand the system dynamics of this combustor, a spectral analysis of the collected data was carried out. Long-duration power spectra, computed via Fast Fourier Transform (FFT), provided a first-pass characterization of the active self-excited dynamics in the combustor. FFTs for image-based data were computed from spatially integrated or averaged probe regions. Spray Mie scattering power spectra used only the upper half of the field of view, OH* CL used the entire field of view and SPIV spectra were generated from probes located in regions along the mains and between them.

Time-frequency spectrograms aid in visualizing unsteady spectral content to distinguish dynamics from amplified noise. The spectrograms were created using Welch's method of overlapped segment averaging and a sliding temporal window to obtain time-varying power spectra. The window size was based on the sampling frequency with 75% overlap, yielding good balance between frequency- and time-resolution.

By treating each pixel of a time series of images as an individual time series and applying the FFT to each produces a spatial power distribution. Such distributions were used to identify the regions where certain frequencies were dominant and create power spectra that fully resolve antisymmetric modes. Two different spatially resolved power spectra are used, named "max-hold" and "spatial-sum" spectra. Max-hold spectra are computed via the spatial maximum power at each frequency, *i.e.*, $\mathcal{P}_{\max} = \max_{(x,y)} |FFT|$, whereas spatial-sum spectra are computed via $\mathcal{P}_{\text{sum}} = \text{sum}_{(x,y)} |FFT|$. Comparing spatially resolved spectra to FFTs of the spatially integrated data reveals frequencies that have spatial patterns that result in phase cancellation. Inspecting the FFT fields of a given frequency provides a more detailed picture of the spatial pattern, or mode shape.

CHAPTER 4
COMBUSTOR CHARACTERIZATION

The data from Campaign 1 is presented in this chapter to illustrate the basic flow and flame characteristics of the LPP combustor. First, the emissions data are presented for sweeps of P_3, T_3 and FAR. Next, the mean fields of the OH* CL, fuel spray Mie scattering and fuel PLIF are presented across a sweep of FAR at constant P_3 and T_3 corresponding to nominal CST cruise conditions. This sweep shows the influence of FAR on the heat release, flame structure and stability and fuel mixing. Finally, the OH* CL and pressure fluctuations provide insight into the dynamics of this combustor. Comparisons of OH* CL and pressure fluctuations at nominal and higher pressures help to identify the impact of P_3 on flame structure and dynamics.

4.1 Normalized Emissions

Figure 17 shows the NOx and CO emissions trends for this combustor. “NC” in Figure 17 designates “nominal cruise” pressure conditions. Each data series corresponds to a different T_3 range, as indicated in the legend. The yellow “x” markers indicate the test cases for the Campaign 1 optical data presented in Section 4.2.1. The normalization is applied individually to EICO and EINOx across all conditions presented, such that low and high P_3 emissions indices are on the same scale. While quantitative values cannot currently be published, the maximum NOx values are in line with NASA’s 2035 CST goal [21].

The increase in CO emissions observed for lean FAR (low T_4) indicates that the system is approaching LBO. Existing literature [7, 22], shows that due to increased local

extinction events along the flame front, there is less complete combustion and oxidation of CO as a flame approaches LBO [7]. This effect is accentuated at lower T_3 because to achieve the same T_4, the FAR must be higher. Furthermore, T_3 influences the reaction rate for the oxidation of CO into CO_2 via reaction with OH [7], so for a fixed residence time or flow rate within the combustor, decreasing T_3 yields greater CO emissions.

Unfortunately, no fuel PLIF was recorded for the near-LBO conditions in Figure 17 (the blue dots for EICO at either P_3), and as discussed in Section 3.4, the OH* CL is not suitable for detection of blowoff. As such, it is not possible to directly address the influence of instantaneous local extinction events on the trends in EICO approaching blowoff in Figure 17. Away from LBO, EICO is independent of T_3 for both P_3 conditions. Increasing P_3 does, however, lead to a small decrease in EICO for the same T_3 and T_4 conditions. This decrease in CO emissions results from the increased reaction rates of alternate oxidation pathways, such as reactions with HO_2 [7]. This trend agrees with those previously reported in literature for CO emissions of gas turbine combustors [7, 87].

Overall, the results for EICO in Figure 17 suggest that T_3 and P_3 have an impact on the blowoff limits of this combustor. The influence of T_3, P_3 and blowoff on emissions will be explored in greater detail throughout the remainder of Chapter 4 and in Chapter 5. In particular, Sections 4.2.2 and 4.2.3 demonstrate that increasing T_3 and P_3 helps to prevent blowoff, which agrees with the EICO trends in Figure 17.

In contrast with EICO, at nominal cruise pressure the trend in EINOx is dependent on T_3, with higher T_3 increasing the sensitivity of EINOx to T_4. The increased sensitivity stems from the fact that to achieve the same T_4 at higher T_3 requires lower FAR. At leaner FAR, other NOx formation mechanisms—such as the intermediate N_2O or prompt

mechanisms—tend to dominate over the traditional thermal NOx mechanism [7]. This trend is not observed in the data at high P_3 conditions even at the highest T_3 due to the smaller range of T_4 collected. However, the EINOx trends at high P_3 match those at low P_3 for similar T_3 and T_4 values. Overall, Figure 17 indicates that increasing P_3 has a slightly reductive impact on NOx emissions and decreases the sensitivity of EINOx on T_3. The reduction in EINOx with increasing P_3 in a gas turbine combustor was previously reported by Xi *et al*. [87]. Xi *et al*. [87] attribute this behaviour to the reduction in flame length and thus residence time in the flame as pressure increases, decreasing prompt NOx formation.

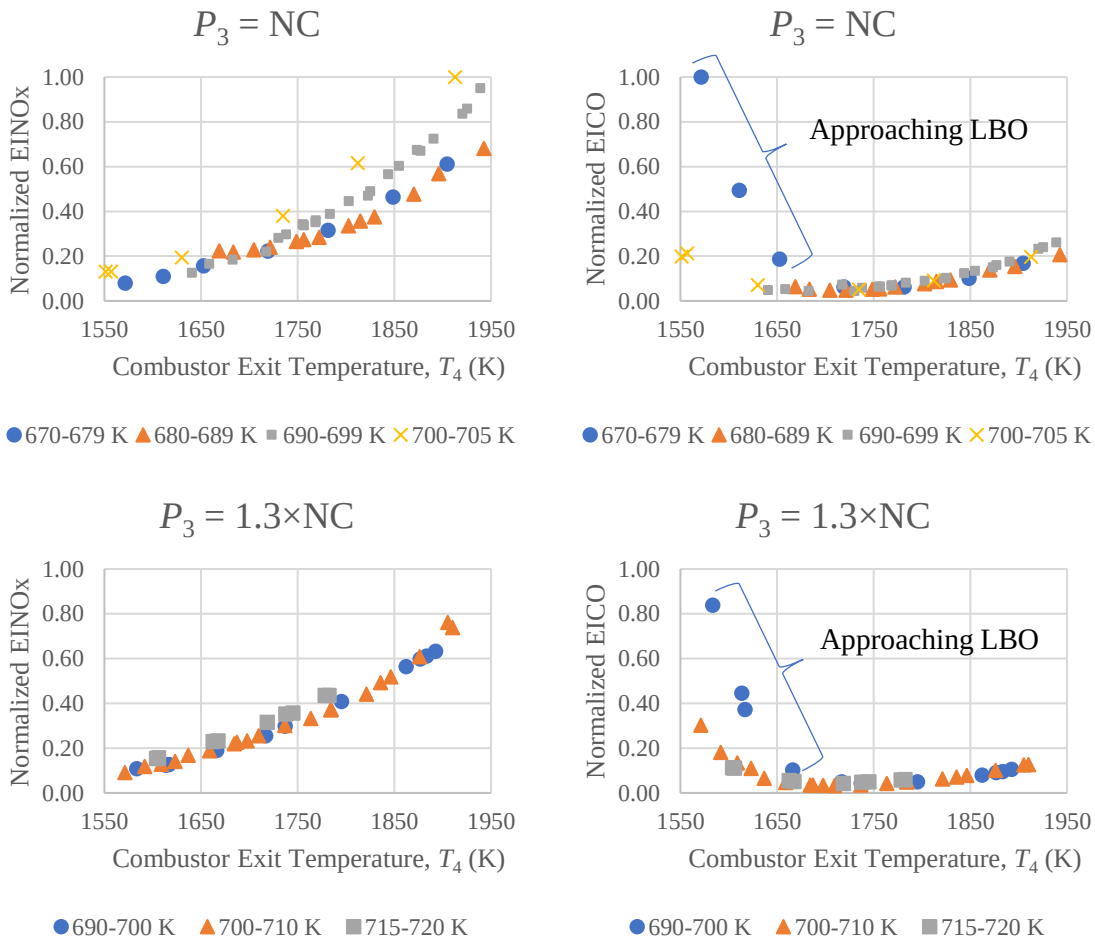

Figure 17: Normalized emissions indices over several TPs at nominal pressure (top row) and high pressure (bottom row) as indicated.

4.2 Mean Flow Fields

4.2.1 FAR effects

Campaign 1

To analyze the fuel spray and mixing characteristics, the mean fuel droplet Mie scattering, OH* CL and fuel PLIF fields were computed for each test case. Figure 18 shows a typical instantaneous PLIF field from the test case with the highest FAR. The mean fields of OH* CL, fuel PLIF and spray Mie scattering are shown in Figure 19, with each case (columns of Figure 19) ordered from left-to-right by decreasing FAR. Each set of mean fields (corresponding to each row in Figure 19) is normalized by the maximum intensity across all cases. The spatial coordinates for the spray Mie scattering and fuel PLIF fields are normalized by the outer diameter of the main fuel injectors. Note that the spray and PLIF field of view are smaller than the OH* CL. The red rectangle in the first CL mean field indicates the approximate position of the Mie scattering and PLIF fields of view.

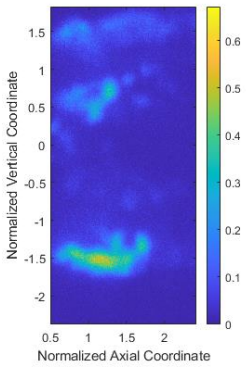

Figure 18: Sample instantaneous PLIF field from highest FAR test case.

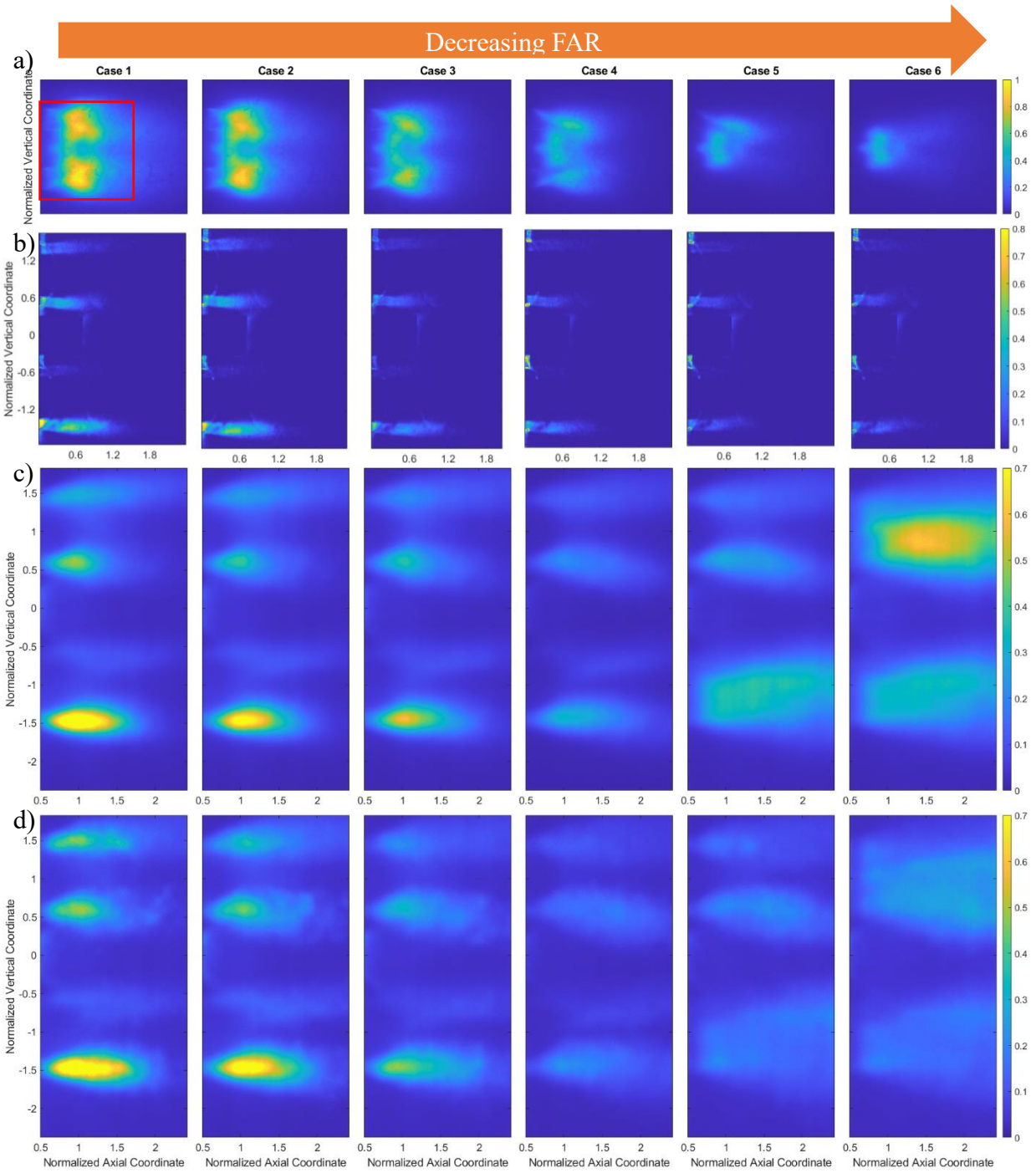

Figure 19: (a) Mean OH* CL, (b) mean fuel droplet Mie scattering, (c) mean fuel PLIF and (d) fuel PLIF root mean squared fluctuations. Approximate position of spray and PLIF field of view denoted by red rectangle in first OH* field.

Despite the sparsity of the fuel droplets in the spray, the Mie scattering mean fields generally agree with the results in the PLIF mean fields in terms of length and qualitative intensity between regions. The sparsity of fuel droplets also indicates that the combustor is vaporizing most of the fuel prior to entry into the combustion chamber, resulting in good overall mixing. The differences in the mean fuel amount between mains (and between the two halves of each main) may be attributed to the discrete fuel injectors in the premixer tube and other naturally arising asymmetries. For example, when the flame is attached, the bottom main always has the highest PLIF signal (Figure 19c, Cases 1-4). Given that fuel PLIF data from Campaign 1 was not corrected for laser energy absorption, the high intensity of the lower branch of the bottom main (Figure 19c) is partially due to the greater density of liquid fuel droplets, as evidenced by the fuel droplet Mie scattering in Figure 19b. It is possible the fuel injectors in the bottom main were oriented such that one along the lower half of the premixer tube was more directly aligned with the PLIF laser sheet than those on the top half, resulting in a higher concentration of fuel along the bottom.

At the higher FARs, the fuel PLIF measurements show an annular region of premixed fuel and air, as well as regions of low PLIF signal denoting burnt products. Product gases occurred both within the bluff body recirculation zone and surrounding the fuel/air jets, indicating an annular partially premixed flame surface. Decreasing the FAR from Case 1 to 4 decreased the PLIF and OH* signals without qualitatively changing the flame geometry. At Case 5, the lower flame blew off, resulting in no lower main flame in the OH* CL; premixed fuel and air filled the recirculation zone in the PLIF images. Further adjusting the conditions to Case 6 resulted in complete blowoff of the main flames. It is worth noting that the behavior of the main fuel injectors was not symmetric in the direction

perpendicular to the laser sheet. Specifically, in Case 5, the upper main on the side of the combustor opposite the laser sheet had also blown off (three of the four mains were blown off). The relatively high root mean squared fuel PLIF fluctuations at all conditions are indicative of both the high turbulence intensity in the shear layer between the mains and recirculation zones, as well as spatiotemporal variations in the fuel/air mixing exiting the premixer tubes. Comparing Figures 17 and 19, the observed increase in CO with decreasing FAR corresponds to the conditions approaching LBO.

Campaign 2

Given the changes to the combustor geometry and the use of a different test rig for Campaign 2, an effort was made to ensure that the flow fields were consistent with Campaign 1. Figure 20 shows the temporally averaged OH* CL and fuel PLIF fields for unforced cases across all three FAR conditions in Campaign 2. Overall, the results appear structurally similar to that in Figure 19. It should be noted, however, that the Campaign 2 data blew off consistently at a higher FAR than in Campaign 1. Comparing Tables 1 and 2 shows that the primary differences in experimental conditions are in T_3 and $\dot{m}_{\mathrm{air}}$. The effects of these parameters on blowoff in Campaign 2 are examined in the following.

Campaign 2 conditions were at significantly lower T_3 tested than in Campaign 1. This lower T_3 caused much less pre-vaporization of the fuel, resulting in a more significant liquid spray entering the combustor, as shown by the relatively high PLIF signal along the main jets despite blowoff in the second and third columns of Figure 20b (compare with Case 6 in Figure 19c). Unfortunately, the increased fuel droplet density was not enough to permit a more detailed analysis of the spray characteristics using the Mie scattering images. Another data collection campaign was conducted using phase doppler particle analysis

(PDPA), but the data from those experiments are not included in this work. As Cavaliere *et al.* [24] show, the increased presence of liquid fuel is believed to have minimal impact on the blowoff Da.

The combined effects of T_3 and $\dot{m}_{\mathrm{air}}$ are accounted for using a Da and Re based correlation. Using the scaling $\mu_3 \propto T_3$ derived in Section 3.2 gives the ratio of Campaign 2 to Campaign 1 (low P_3 only) Reynolds number as $\mathrm{Re}_2/\mathrm{Re}_1 \approx 1.2$ to two significant figures. As will be shown in Chapter 5 using the Campaign 1 data, such an increase in Re is not enough to yield a significant difference in the Da at blowoff. Furthermore, applying scaling relations to τ_{chem} based on the trends reported in Section 3.2 estimates that the Campaign 2 Da are ~20% lower than those in Campaign 1 at similar FARs. It is hypothesized that this is due to the ~20% higher mass flow rate through the combustor in Campaign 2 than in Campaign 1 for the same P_3 (compare Tables 1 and 2). As a result, the FARs in Campaign 2 equate to lower Da than the same FAR in Campaign 1. Assuming the same blowoff limits in terms of Da for both campaigns indicates that, for Campaign 2, blowoff should occur at higher FARs.

The OH* intensity in the pilot relative to the main flames also differs between campaigns. Figure 20 shows that, while the peak signal still occurs in the region where the main and pilot flames overlap, the pilot has similar intensity to the overlap region. Furthermore, the pilot appears to be the main contributor of OH*, especially near blowoff. Assuming the same main-pilot air mass flow rate ratio as in Campaign 1 yields a pilot thermal power in Campaign 2 that is higher than that of a single main, especially since the pilot is near-stoichiometric (i.e., $\mathcal{P}_{\mathrm{th,p}} > 0.2\mathcal{P}_{\mathrm{th,tot}}$). This suggests the high intensity in the main-pilot overlap region is mostly due to the contribution of the pilot flame.

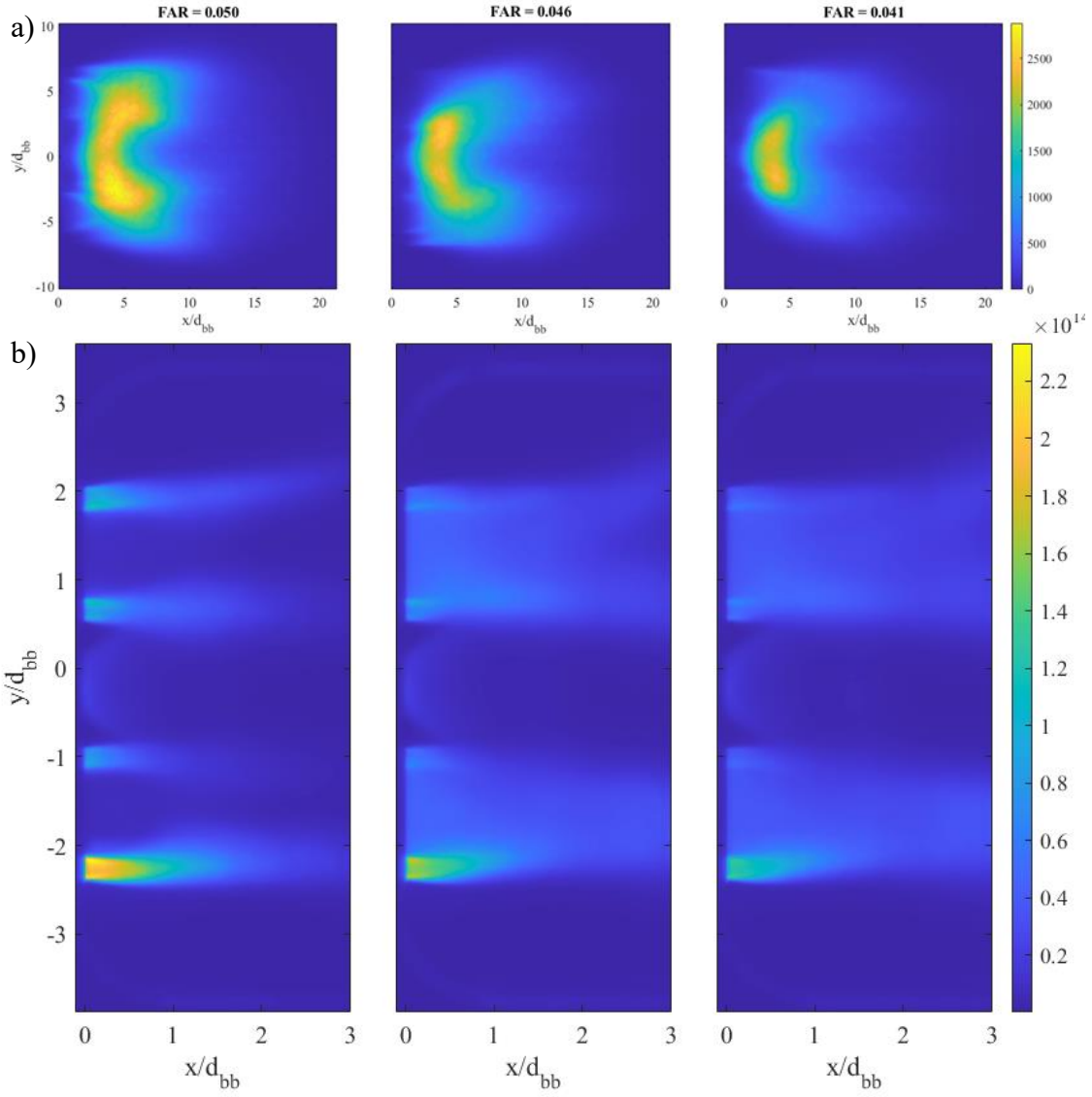

Figure 20: Temporal mean fields from Campaign 2 unforced FAR sweep. (a) OH* CL, (b) fuel PLIF.

Figure 21 shows the unforced, nonreacting (top row) and reacting (bottom row) SPIV velocity fields from Campaign 2. In both cases, the main recirculation zone behind the bluff-body is approximately $1d_{bb}$, matching the corresponding regions in Figure 20b. In the reacting case, however, the shear layers follow a straighter path than in the nonreacting case, as shown by the zero-contours in the vorticity fields.

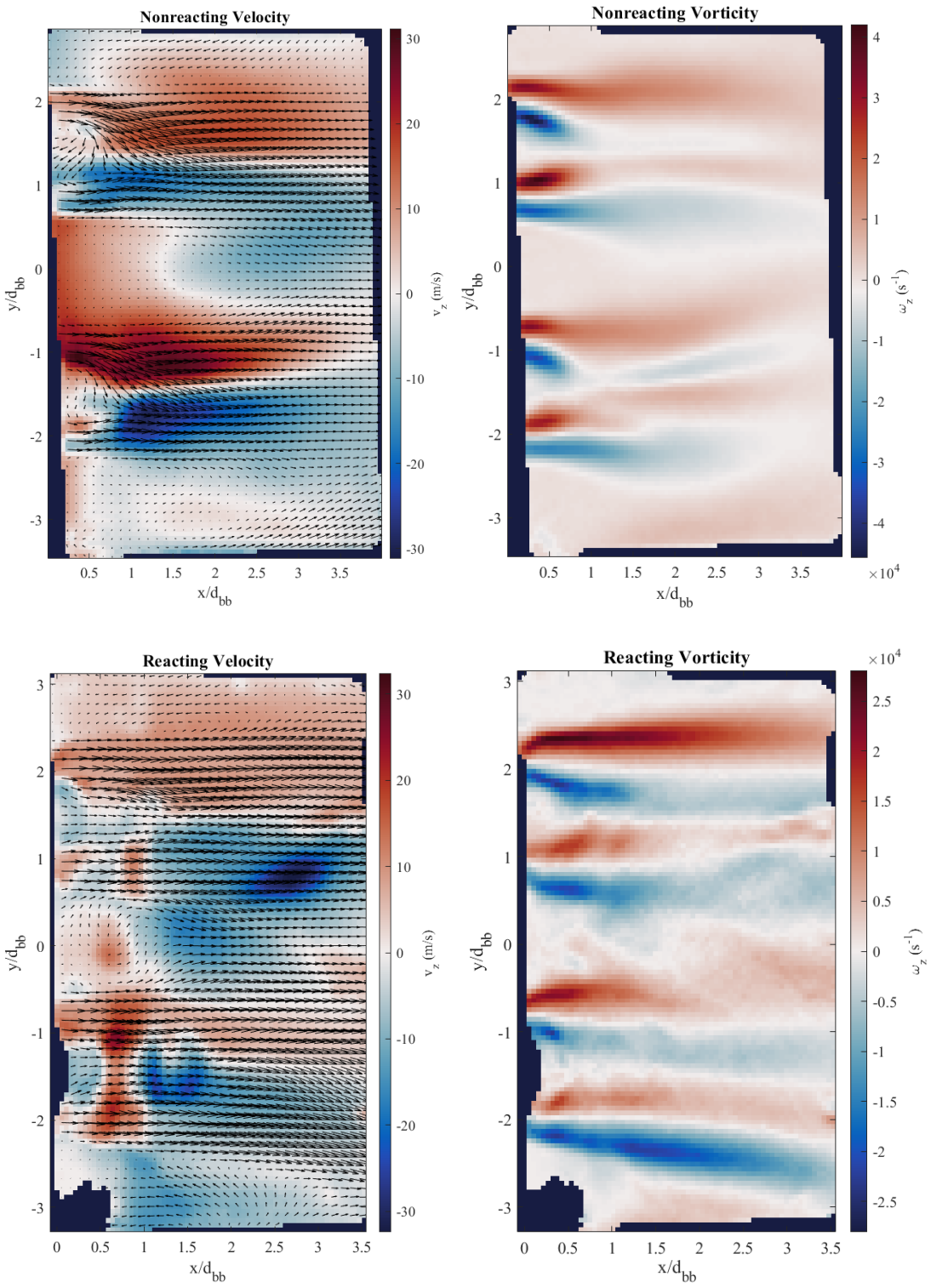

Figure 21: Temporal mean velocity (left) and vorticity (right) fields at nonreacting (top) and reacting (bottom) conditions from Campaign 2. Coordinates normalized by the bluff-body diameter. Only half of the vectors are shown for clarity.

4.2.2 Inlet temperature effects

Campaign 1 also involved sweeps of T_3 across all conditions. For brevity, the results from one of the FAR sweeps with low P_3 at a lower nominal T_3 and another at the highest nominal T_3 are presented in Figures 22 and 23 below. Figure 22 shows the time-averaged OH* CL fields for both T_3 conditions and Figure 23 shows the time-averaged fuel PLIF fields at the same test conditions. Note that the first two fields in the top row of Figure 22 were recorded with a lower intensifier gain than the others, while the other two in the top row had a higher gain than those in the bottom row. Due to the lack of whitefield calibrations for the OH* data, the colour scales are thus not consistent in Figure 22.

The mean fields in Figure 22 indicate that T_3 has two effects on the structure of heat release. The first is a slight expansion of the region of peak heat release at higher T_3. The second is that increasing T_3 improves flame stability at the leanest FAR, indicated by the reappearance of OH* signal along the top main at high T_3. This observation is corroborated by the corresponding fuel PLIF mean fields in Figure 23, which show that the top main reattached at higher T_3.

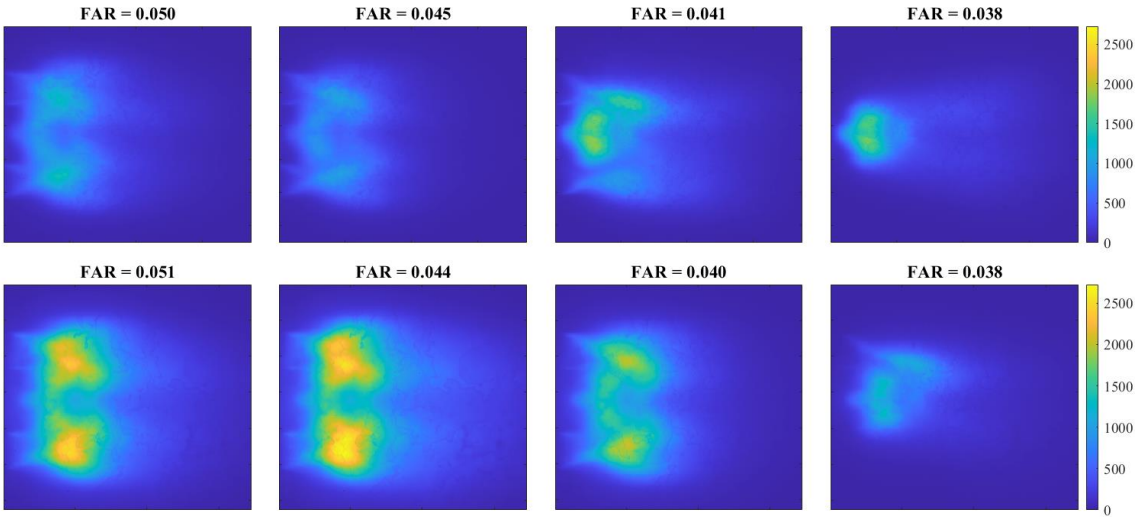

Figure 22: Temporal mean OH* CL fields at low (top row) and high (bottom row) T_3.

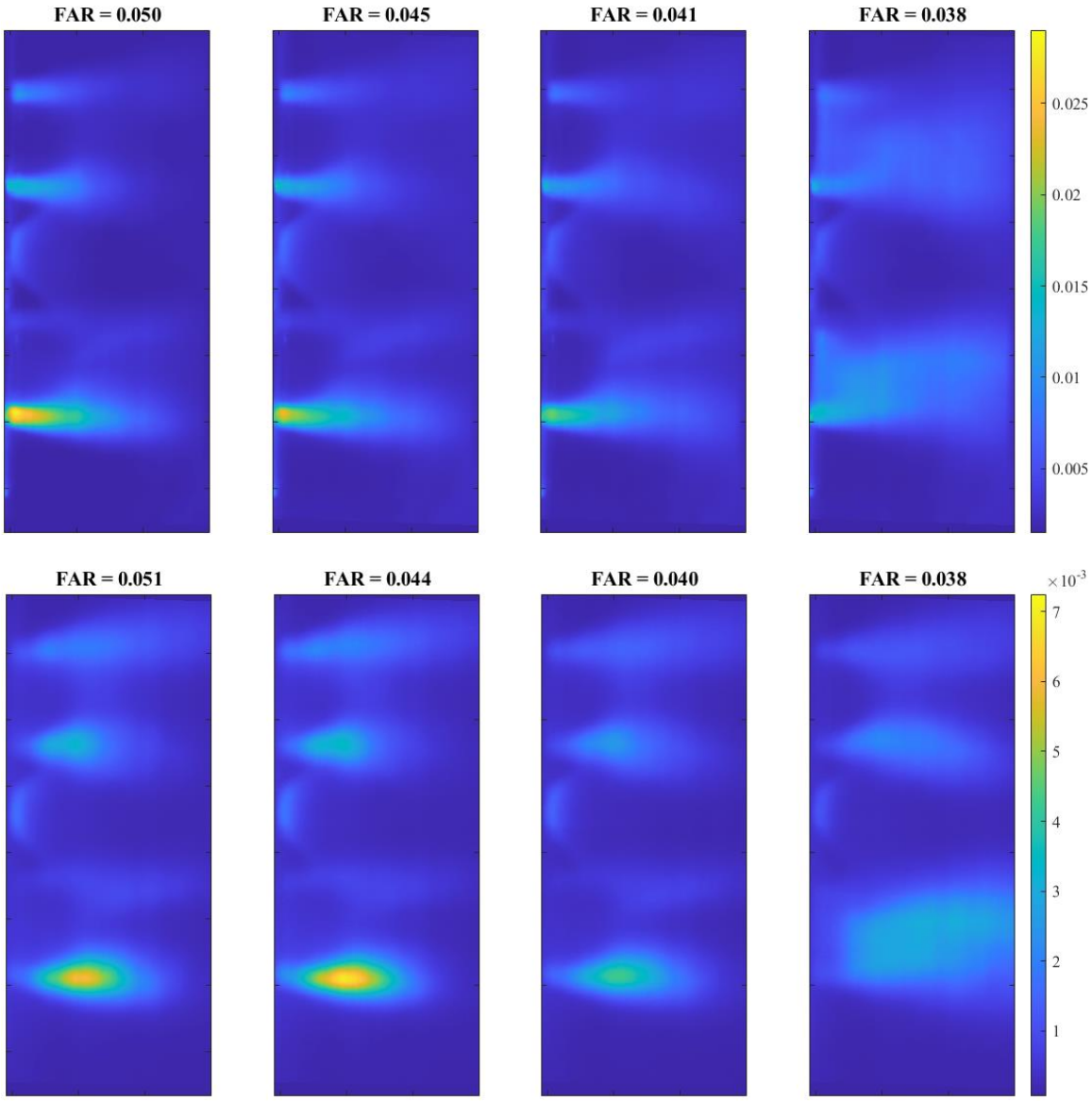

Figure 23: Temporal mean fuel PLIF fields at low (top row) and high (bottom row) T_3.

From the fuel PLIF mean fields in Figure 23, it is evident that T_3 has some impact on the fuel-air mixing. At lower T_3 (cf. Figure 23 top row), the peak fuel PLIF signal occurs next to the combustor dome face. At high T_3 (cf. Figure 23 bottom row), the peak fuel PLIF signal is shifted downstream and the region broadens. The two factors that could cause this shift are the amount of liquid fuel entering the combustor and the spray characteristics.

As shown in Figure 20, which is at even lower T_3 than the data in Figure 23, less pre-vaporization occurs for lower T_3. The liquid phase is a much higher concentration of fuel compared to a premixed and pre-vaporized fuel-air mixture and thus fluoresces strongly in comparison. Furthermore, with less pre-vaporization at lower T_3, there is less mixing between the fuel and air, which also contributes to high PLIF signal close to the dome face. The effect of the fuel droplets is illustrated in the lower branch of the bottom mains at low T_3 (Figure 23 top row). As the FAR decreases, the peak PLIF intensity next to the dome face decreases as the amount of fuel droplets entering the combustor decreases.

Additionally, as T_3 increases, the vaporization rate of any liquid droplets that enter the combustor increases, changing the mean spray characteristics. The increased evaporation rate of the droplets and the higher flame temperatures resulting from the increased T_3 cause a more rapid expansion of the main jet which broadens its profile. Furthermore, there are turbulence and combustion effects that couple dynamically with the main jet as described by Nair [88]. In general, these dynamic effects cause the boundaries and shape of the jet to be unsteady in time, which would broaden the resulting mean field.

4.2.3 Inlet pressure effects

Figures 24 and 25 report mean fields of OH* CL and fuel PLIF at high and low P_3. Due to the combustor operation, the higher P_3 conditions also had higher $\dot{m}_{\mathrm{air}}$, while FAR and T_3 were held roughly constant. In Figure 24, the mean fields in the top row for FAR = 0.050 and 0.045 were recorded at a lower gain than the others, which explains why only those two fields have lower total signal. Otherwise, the mean fields have very similar structure and intensity for similar FARs, regardless of P_3. For example, the pilot cone angle and flame lengths do not change despite the increased $\dot{m}_{\mathrm{air}}$ at high P_3. The OH* CL suggests

the heat release rate is not strongly dependent on P_3 in this combustor, as expected for a lean-burn configuration.

A similar conclusion can be drawn regarding the fuel-air mixing based on the fuel PLIF mean fields in Figure 25. Namely, that P_3 has minimal impact on the level of fuel-air mixing in the combustor. Figure 25, however, shows a stabilizing effect: at the lowest FAR, the higher P_3 keeps the top main flame attached. While this appears to contradict the observations from the OH* fields in Figure 24, the OH* is not a reliable indicator of blowoff. As discussed in Section 3.4, the fuel PLIF recording interval was much longer than the OH* CL (more than 100 times longer). Since the fuel PLIF clearly shows the top main is attached for high P_3, FAR = 0.036 while the OH* does not, this could be an indication of some intermittency in the flame attachment. Reviewing the instantaneous fuel PLIF and OH* CL images indicates no intermittency, *i.e.*, the top main is attached in all fuel PLIF images and detached in all OH* CL images. Given that the OH* CL and fuel PLIF cameras were not triggered at the same time, it is most likely that for this TP, the OH* CL and fuel PLIF did not overlap temporally. Section 5.1 explores the effects of P_3 on blowoff in more detail.

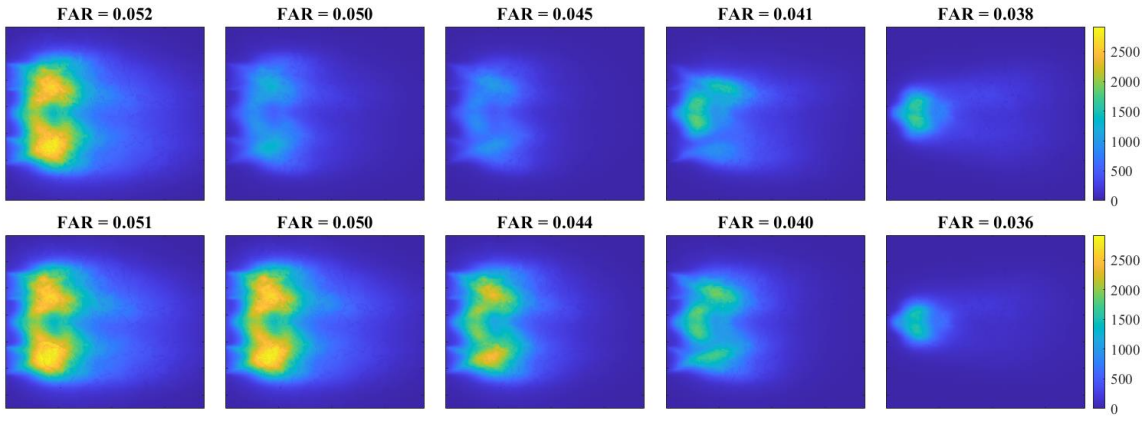

Figure 24: Temporal mean OH* CL fields at low (top row) and high (bottom row) P_3.

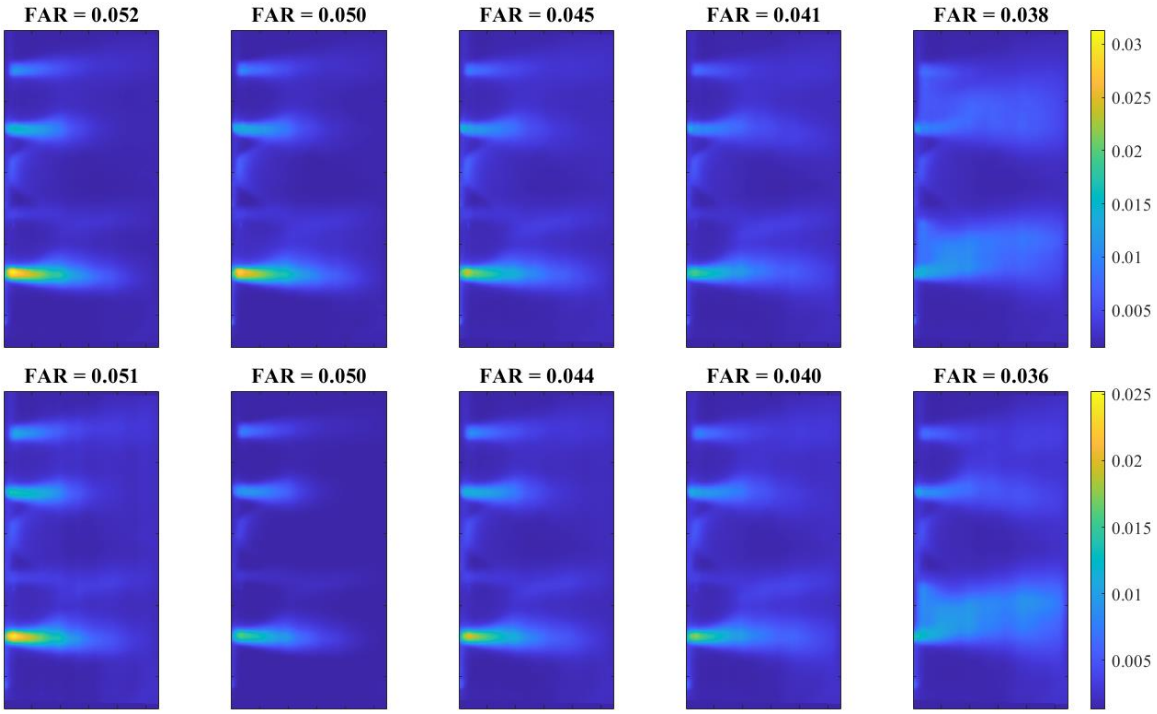

Figure 25: Temporal mean fuel PLIF fields at low (top row) and high (bottom row) P_3.

4.3 Natural (Unforced) Dynamics

Figures 26 and 27 display the power spectra computed via FFT for the pressure and globally integrated OH* CL fluctuations, respectively. Both figures use the same data sets (also the same as that used to generate the mean fields in the preceding sections) and illustrate the effects of changing FAR, P_3 and T_3 on natural dynamics within the combustor. Note that the power spectra are limited to frequencies less than 1 kHz for clarity and because there is no spectral content beyond 1 kHz in any of the power spectra. Due to the sparsity of fuel droplets, the fuel Mie scattering from both campaigns is unsuitable for this computation. The gas phase velocities from Campaign 2 have a large quantity of outliers, making them unsuitable for this analysis as well. Both the spray Mie scattering and gas velocities have thus been omitted.

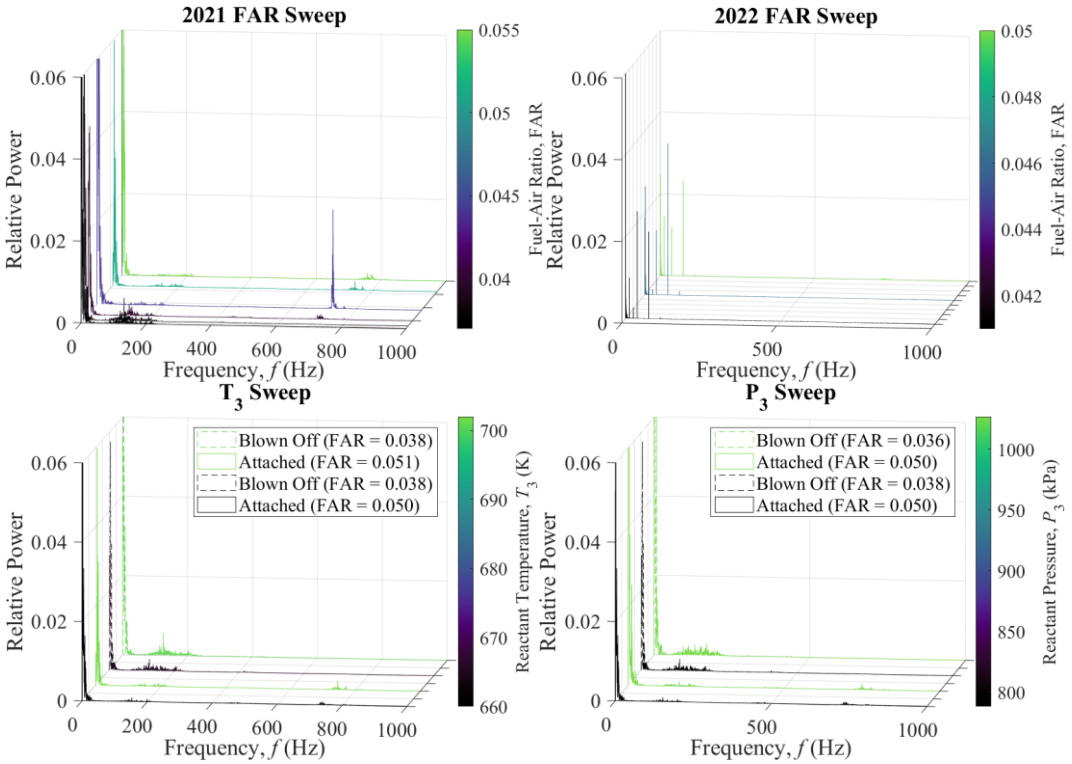

Figure 26: Pressure FFTs across sweeps of operating conditions.

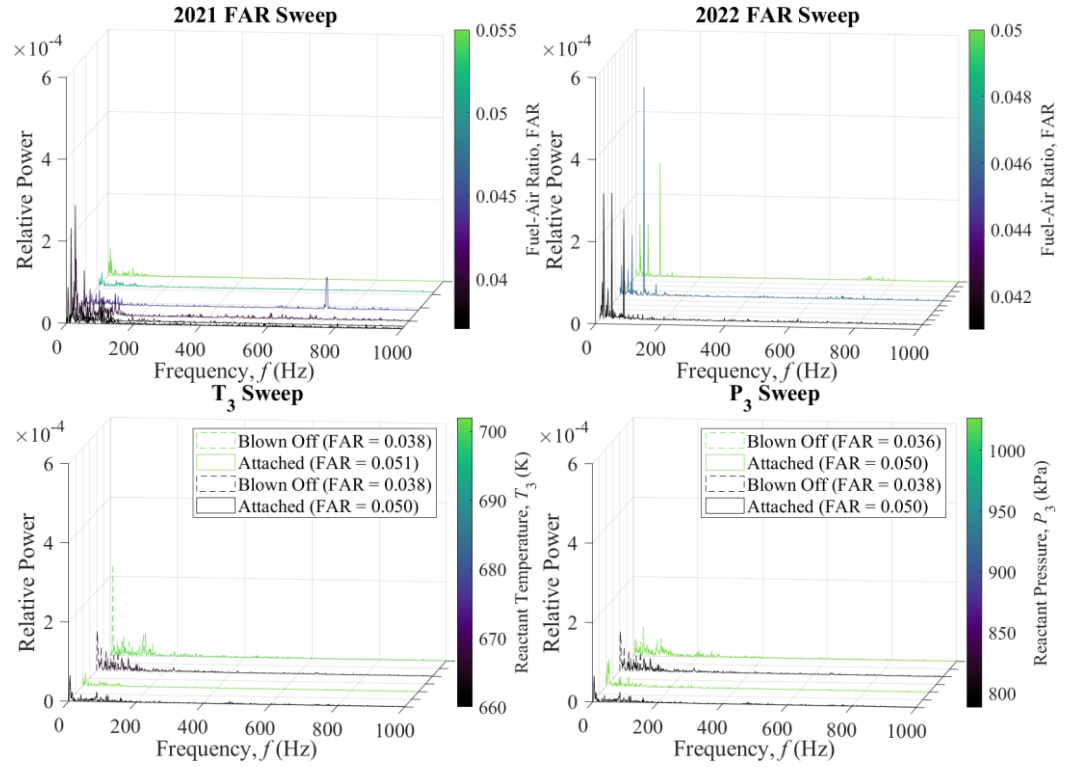

Figure 27: OH* CL FFTs across sweeps of operating conditions.

Overall, the power spectra in Figures 26 and 27 change very little with respect to each parameter. The T_3 sweep indicates that at higher temperatures, the pressure and OH* dynamics tend to have higher amplitudes and that blowoff results in higher amplitude dynamics at low frequencies. The P_3 sweep shows the opposite, with the higher pressures yielding lower amplitude dynamics when the flame is attached. In both cases, the heat release rate amplitudes appear less affected by either parameter (Figure 27, bottom row). As expected, varying the FAR has the greatest effect on both heat release rate and pressure fluctuations. Interestingly, blowoff appears to have no major effect on the power spectra in Figures 26 and 27.

From the Campaign 1 FAR sweep, decreasing FAR increases the amplitude of the low frequency dynamics (< 300 Hz) in both the pressure and heat release rate. At specifically FAR = 0.044, however, there is a spike in spectral content ~730 Hz. Comparisons of power spectra from other data sets indicate that the increased power of 730 Hz oscillations is anomalous. Specifically, the high amplitude ~730 Hz dynamics do not occur for other data sets at similar (FAR, P_3, T_3) conditions but do occur for some data sets at different conditions.

The 2022 FAR sweep illustrates the effect of the rig design modifications. As mentioned in Section 2.1.2, Campaign 2's test article added a damping plate in the exhaust duct to eliminate 600-800 Hz oscillations. Figures 26 and 27 also show that the Campaign 2 test article had relatively high amplitude dynamics below ~100 Hz. Given that these low frequency oscillations were not present in the Campaign 1 data, they must be characteristic of the test facility used in Campaign 2. Indeed, these frequencies were observed in other experiments at the same facility with completely different combustor designs.

CHAPTER 5

FLAME STABILIZATION

Given the complexity of the multi-element LPP combustor flow fields presented in Chapter 4, this chapter focuses on the effects of pilot-main and main-main interactions on blowoff limits. Beginning with a presentation of the recorded results in (Re, Da) space, the data is filtered down to only the conditions where blowoff occurred. After assessing the influence of P_3 and T_3 on blowoff limits, potential outliers are identified. The resulting data, with outliers removed, is compared with trends and data reported in the combustion literature. The discrepancies between the observations and literature suggest the pilot flame has a substantial impact on flame attachment. Finally, the analysis of the potential outliers explores the various factors and phenomena that contribute to flame blowoff.

5.1 Pressure & Temperature Effects on Blowoff

Figure 28 collects the blowoff results for data points recorded in Campaign 1. The data sets from one run date have been excluded due to possible improper rig operation. As described in Section 3.4, a test point was considered blown off if any fuel PLIF signal was detected behind the bluff-body of a single main. The point in the red circle in Figure 28 marks an outlier, as it has an abnormally high Da_{LBO} and is discussed in Section 5.3. Note that the increase in Re caused by increasing P_3 is only due to the increase in density. Based on literature [22, 23], increasing Re should decrease Da_{LBO}. However, the wide range in Da_{LBO}—even excluding the potential outlier—and limited range of Re for the data shown in Figure 28 yields too much uncertainty in the slope of a (Da, Re) correlation to quantify

the effects of P_3 on Da_{LBO}. The comparison with correlations presented in existing literature is continued in Section 5.2.

Figure 29 plots only the conditions that exhibited blowoff and colours the dots by the range of T_3. Due to the nature of the experiment operations and procedures, it was not possible to vary only one of P_3, T_3 or φ at a time. In nearly all cases, all three parameters varied between TPs. As shown in Figures 28 and 29, this obfuscates the relationships between P_3 or T_3 and Da_{LBO}. From theory [7], one would expect higher T_3 to increase reaction rates, decreasing τ_{chem} and thus Da_{LBO}. From Figure 29, however, there appears to be no relationship between T_3 and Da_{LBO}. These figures demonstrate how Da VS Re correlations capture the effects of P_3, T_3 and φ simultaneously and more clearly. In addition, Da correlations capture several other physical aspects of the blowoff process, as detailed by Shanbhogue *et al*. [22] and reviewed in Section 1.3.1.

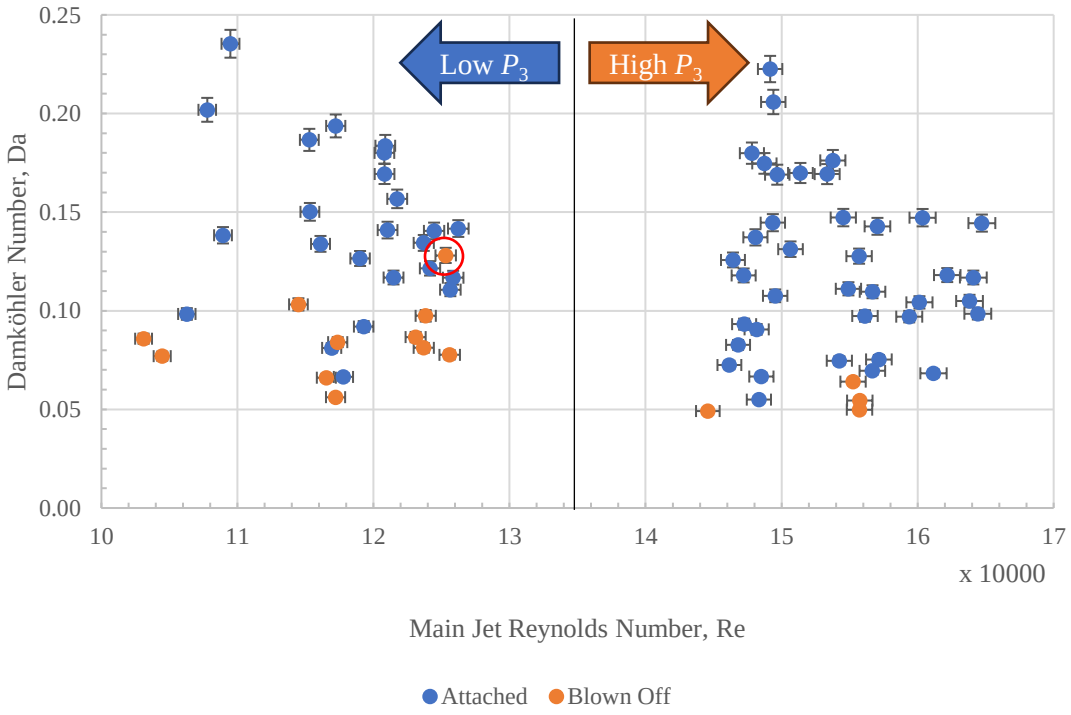

Figure 28: Da VS Re for all test points in Campaign 1. Arrows denote clusters of data corresponding to low and high P_3 as indicated. Aberrant blowoff case circled in red.

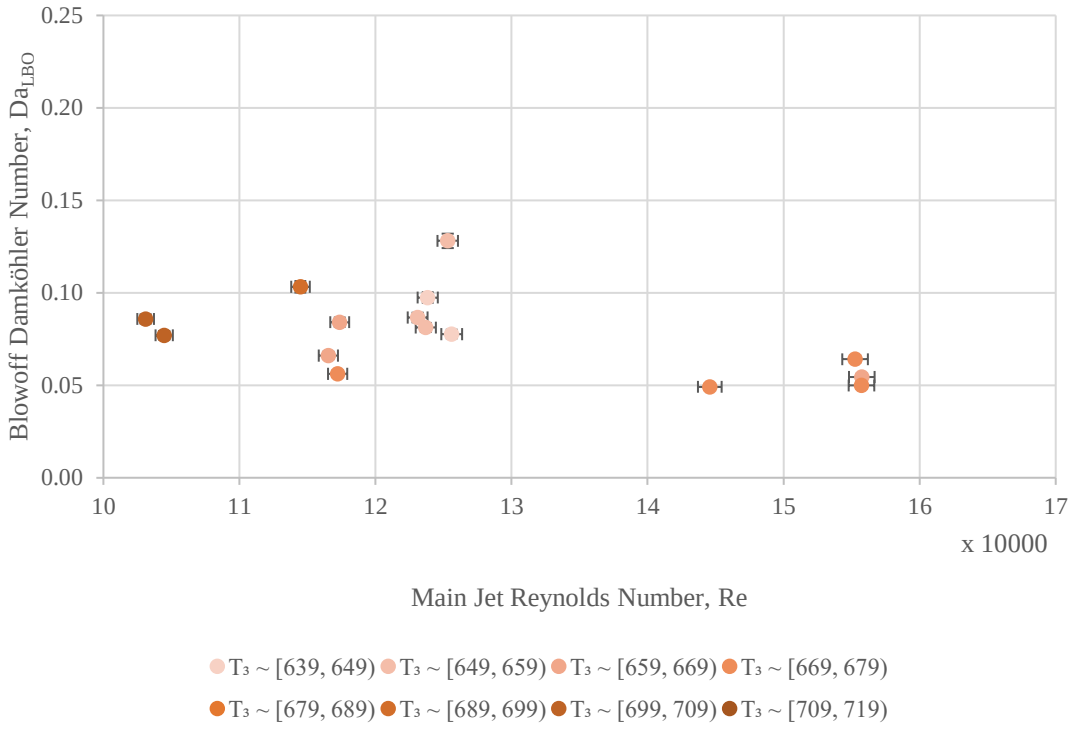

Figure 29: Blowoff Da VS Re for varying temperature. Colour of markers denotes T_3 range as indicated in the legend.

5.2 Comparison with Existing Correlations

The limited range of Re spanned by the data makes it unsuitable for computing Da correlations directly. As such, these results were compared with those previously reported in literature. Figure 30 overlays the new data points on top of those compiled by Shanbhogue *et al*. for 2D and axisymmetric 3D bluff-bodies [22]. As detailed in Section 3.1, the computation of Re and Da uses the same relations employed by Shanbhogue *et al*. [22] to ensure compatibility of the plots.

From Figure 30, it is clear the Campaign 1 results do not follow the expected correlation for axisymmetric bluff-bodies. Overall, the data from Campaign 1 are grouped towards the lower limit of the other data in Figure 30 (left) and appear to follow a trend

with a steeper slope. This discrepancy is expected, since the data reported by Shanbhogue *et al*. are collected from studies of single-element, unpiloted combustors operating at nearly atmospheric pressure and temperature [22]. It remains to identify the factors that contribute to this discrepancy as follows. Given the nature of this LPP combustor, particular attention is paid to the effects of CST-relevant P_3 and T_3, along with the interactions of the various main and pilot flames and flows.

Section 5.1 explains that, for the conditions analyzed in this combustor, changing P_3 does not have a quantifiable effect on Da_{LBO} and therefore will be neglected from the remaining discussion. The observed independence of Da_{LBO} from T_3 (Figure 29) matches behaviour noted by both Shanbhogue *et al.* and Tuttle [22, 23]. Tuttle's work [23] specifically explores the effects of variations in T_3 for premixed flames, finding that T_3 has a stabilizing effect, but only with respect to the blowoff φ at a given Re. Tuttle notes that varying T_3 yields an approximately constant value for Da_{LBO} [23], which roughly agrees with the results in Figure 29. Cavaliere *et al*. [24] corroborate this finding in the context of the degree of pre-vaporization and premixing. Their experiments show that fully premixed, non-premixed and liquid spray flames blowoff at similar Da and Re [24]. For an LPP combustor, T_3 controls the amount of pre-vaporization of the liquid fuel and thus influences the amount of premixing of the fuel and air. Together, the works of Tuttle [23] and Cavaliere *et al*. [24] demonstrate that T_3 has minimal impact on Da_{LBO} and thus cannot explain the discrepancies in Figure 30 (left). As such, it is concluded that the discrepancies in Figure 30 (left) must be due to the combustor configuration and flow field rather than (global) inlet conditions.

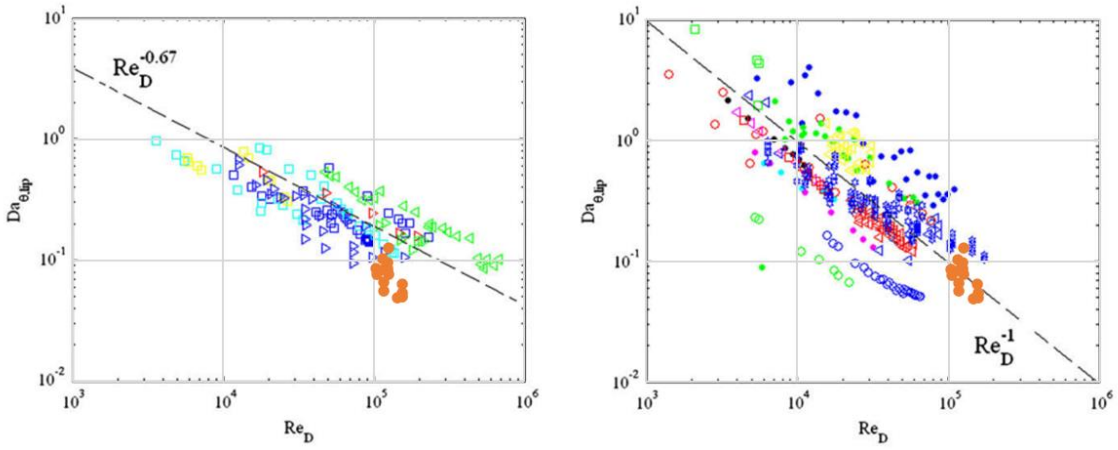

Figure 30: Da VS Re for axisymmetric (left) and 2D (right) bluff-bodies. Solid orange dots are data from Campaign 1, other data from Ref. [22]. Error bars are too small to see.

The reviews of Shanbhogue *et al*. [22] and Tuttle [23] reveal several other relevant factors that could explain the trends in Figure 30. The effects of spatial variations in φ, due to both stratification and partial premixing, dynamic coupling and flow symmetry are particularly relevant. As discussed above, Cavaliere *et al*. [24] show that although less premixed flames tend to blow off at leaner φ, there is minimal effect on Da_{LBO}. Specifically, Cavaliere *et al*. [24] compute Da_{LBO} based on the local chemical processes, using local φ for premixed flames and stoichiometric φ for non-premixed/spray flames. They note, however, that non-premixed and spray flames do not behave like premixed stoichiometric flames, despite having similar chemical rates with respect to blowoff [24].

Unfortunately, the recorded data cannot resolve instantaneous, local fluctuations in φ. Figure 19d, however, shows such fluctuations are significant in this combustor. Despite not accounting for the level of premixing as done by Cavaliere *et al*., Da_{LBO} is closely grouped in Figure 28, suggesting that the flame chemistry is predominantly premixed in

character. This is further supported by the sparsity of the fuel spray (Figure 19b). Therefore, local, instantaneous variations in φ are not a major contributor to blowoff.

As shown in Chapter 4 (*e.g.*, Figure 18, etc.), there is some degree of φ stratification (*i.e.*, asymmetric fuel profiles) across the mains. Specifically, the top branch of the bottom main always tends to have less fuel than the bottom branch (see Figure 19b-c). Given that single combustor elements have some stratification and $\varphi_p \neq \varphi$, there is also stratification across the combustor itself in the regions where the fluid streams from the mains and pilot mix. Tuttle [23] demonstrates, however, that stratification reduces flame stability, causing blowoff at higher φ than for uniform fueling. Since this would result in a higher Da_{LBO}, it does not explain why the Campaign 1 data blow off at lower Da than expected for axisymmetric bluff-bodies.

A similar argument also applies to the effects of acoustic coupling (see Ref. [23]), excepting the outlier case circled in Figure 28. As Tuttle [23] explains, for fuel stratified flows, the thermoacoustic dynamics can lead to blowoff at higher Da values than expected. Tuttle [23] also demonstrates that stratified φ flows are more prone to acoustic coupling at lower Re. In such cases, the power spectrum of OH* CL should exhibit strong peaks at frequencies related to hydrodynamic modes of wakes, such as the Bénard-Von Kármán instability [23]. Reviewing the unforced dynamics in Section 4.3 indicates that the power spectra of blown off data sets do not differ substantially from those of attached data sets or other blown off data sets (cf. Figures 26-27). Furthermore, acoustic coupling is a has a destabilizing effect on blowoff and thus cannot explain why the data from Campaign 1 in Figure 30 (left) are at lower Da_{LBO} than the other data points. This indicates that, nominally,

the blowoff observed in the reported data sets is not due to acoustic or hydrodynamic coupling. For analysis of the outlier, see Section 5.3.

The interactions between individual flames are also important. As Figure 19a shows, the wide cone of the pilot flame intersects with the main flames. The pilot-main mixing zones would be heated by the pilot's combustion products, as would the flame base near the dome face due to the outer recirculation zones of the pilot. Based on Refs. [22, 23] and the preceding discussions, it is reasonable to expect the local increase in T_3 would have minimal effect on Da_{LBO}. However, the temperature of the pilot products is far enough outside the range investigated by Tuttle [23] for other factors to become important. For example, the pilot could serve as an ignition source for the mains, which should help to maintain flame attachment at conditions where blowoff would occur normally. In addition, in Campaign 1, the pilot operated at fuel-rich φ, while the mains operated at fuel-lean φ. This means the hot combustion products from the pilot contained some excess fuel that could mix with the oxidizer-rich fluid from the mains and combust. The instantaneous OH* CL images do not provide any insight into this hypothesis. Future work should endeavour to quantify the stabilizing effect of the pilot flame.

For conditions where blowoff would occur without the pilot flame, or even conditions approaching LBO, the strain experienced by the flame causes local extinction, leading to holes appearing in the flame sheet [22]. The regions of local extinction can be reignited by the hot gases from the pilot flame or from the recirculation zones near the dome face, which would allow the main flames to stay attached when subjected to strains that would normally lead to blowoff. Building on the blowoff process presented in Section 1.3.1 and by Shanbhogue *et al*. [22], the pilot flame works to suppress the formation of the

holes in the flame sheet. This delays the onset of the first stage of blowoff (cf. Figure 2) and, in turn, the onset of stage 2 and ultimate blowoff. As Shanbhogue *et al*. [22] explain, Da correlations capture the physics associated with the first stage of blowoff and thus should capture the influence of the pilot flame in this combustor. More precisely, the fact that Da_{LBO} is lower for the Campaign 1 data than expected for axisymmetric bluff-bodies could be because the calculation of Da in this thesis does not properly account for the pilot's effects.

Finally, one must consider the interactions between the mixer elements (mains and pilot) and their impact on blowoff. As shown in Figure 21, the mains also have a small counterclockwise swirling component to the velocity. While not high enough to stabilize the flame or form other hydrodynamic phenomena, this swirl velocity is important to defining the symmetry of the main flames. Since the mains swirl in the same direction, the region between each of the mains is subjected to flows swirling counter to one another. As shown in Figure 21, this creates top-bottom—and logically left-right—asymmetries in the wakes behind each of the bluff-bodies. The pilot swirls clockwise, however, such that the tangential velocity of the pilot is aligned with each of the mains where the flows meet. This would yield regions of locally increased swirl velocity as due to the higher swirl component in the pilot relative to the mains. In general, these regions of local shear disrupt the periodic symmetry of a single main's flow field. Based on the data in Ref. [22], axisymmetric bluff-bodies have a different (Da, Re) correlation than nominally 2D ones.

As discussed in Section 1.3.1, blowoff is an example of a symmetry-breaking bifurcation with hysteresis. It has been observed in other symmetry-breaking bifurcations that when the system is biased against the axis of broken symmetry, the bifurcation can be

delayed [30, 53]. Relating this back to blowoff, flow features that are counter-aligned to those that appear after blowoff could delay the onset of blowoff. Therefore, it is possible that the discrepancies in Figure 30 (left) are due in part to the loss of flow symmetry and periodicity. The data collected and presented in this thesis is not capable of resolving such effects and this is one area recommended for future work.

Overall, the data presented in this section indicates the multi-element mixer design enhances the blowoff limits compared to single-element bluff-body stabilized flames. The analysis focuses on potential chemical effects that could explain the observed enhancement in blowoff limits. The dominant factor was determined to be the that the mixing regions between the pilot and mains serves as a potential ignition source to stabilize flames beyond the normal blowoff limits. Additionally, these flame and flow interactions disrupt the natural flow symmetry, resulting in behaviour that is unlike that previously reported for axisymmetric bluff-bodies. This conclusion is supported by the coincidence of the Campaign 1 data with the correlation for nominally 2D bluff-bodies (Figure 30 right).

There are potential confounding factors with respect to flow time scales that could also resolve the observed enhanced stability. Such factors include the effects of boundary layer thickness around the bluff-body, the detailed bluff-body geometry and the influence of pressure gradients in the flow field. Additional work is required to properly address these effects.

5.3 Investigation of Aberrant Blowoff Behaviour

The outlier identified in Figure 28 poses a particular issue with the operation of this LPP combustor. The possibility of blowoff at abnormally high Da reduces the reliability of operations. Thus, the outlier indicates a possible failure mode for the operation of this style

of combustor. The following analysis aims to determine the root cause of this outlier to assess the potential failure mode. The discussions in Sections 1.3.1 and 5.2 indicate that potential causes include hysteresis and dynamical coupling; both are explored below.

This case of aberrant blowoff occurs at Da = 0.13, approximately 30% higher than the next highest case with blowoff (Da = 0.10), although the Re are different. In contrast with other blown off data sets at similar Re, the aberrant case Da_{LBO} is 30-63% higher. Furthermore, there are other data sets recorded at similar Re, T_3 and P_3 that did not experience blowoff. Closer examination of the operating conditions for the outlier case and others on the same date revealed that the TPs preceding the outlier were also blown off, but at leaner φ and lower Da (same T_3 and P_3). This suggests the blowoff in the outlier case is due to hysteresis.

If the aberrant blowoff is due to hysteresis, then there should be some intermittency in the instantaneous data. Indeed, inspection of the instantaneous fuel PLIF images reveals a switching intermittency. For roughly the first third of the data set, both mains are attached and the bottom main is blown off for the remainder of the images. Additionally, during the attached interval, there are instances where the bottom main blows off for 1-2 frames in sequence. The reverse is true during the blown off interval: there are individual frames where the bottom main is attached. Figure 31 shows sample instantaneous fuel PLIF fields from the aberrant blowoff case. Figure 31 (left) is taken from the attached interval and shows the bottom main flame is attached, while the other field is taken from the blown off interval and shows the flame is blown off. Both fields in Figure 31 are normalized by the maximum intensity in each field.

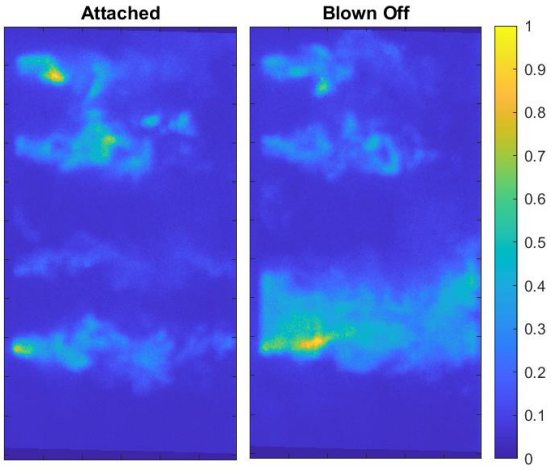

Figure 31: Sample instantaneous fuel PLIF fields from attached and blown off intervals of aberrant blowoff case.

In contrast, in the TPs preceding the aberrant case (both at leaner φ), the bottom main is always blown off with no intermittent switching at all. The RMS fluctuation fields in Figure 32 reflect the intermittency of the aberrant case in a more compact manner than using series of instantaneous images. Comparing the other blown off cases in Figure 32 (φ = 0.64, 0.61) to the aberrant case (φ = 0.70) shows significantly higher RMS fluctuations in the bottom main behind the wake in the aberrant case than for the other two.

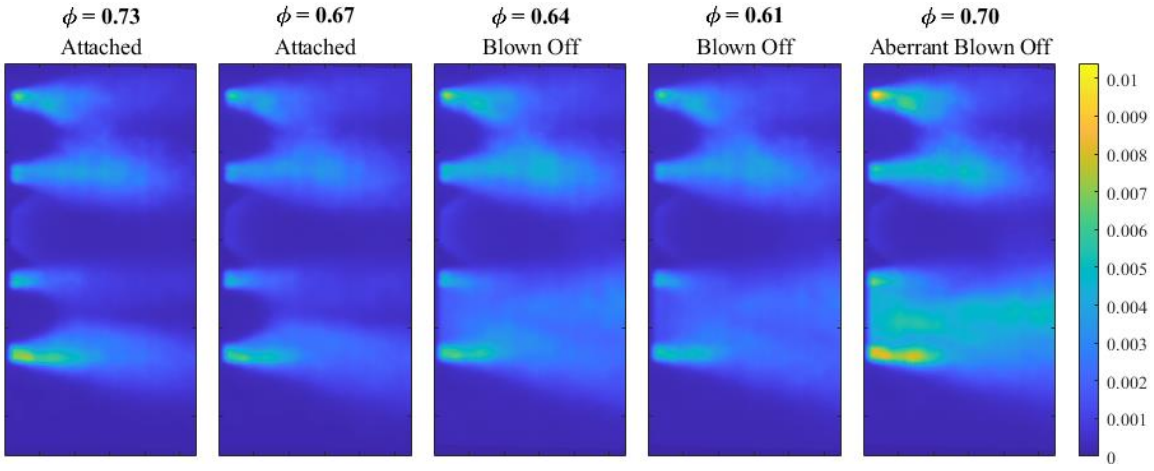

Figure 32: Fuel PLIF RMS fluctuation fields for TPs preceding and including outlier case. TPs are ordered chronologically from left to right.

Unfortunately, the fuel PLIF sample rate of 10 Hz was too slow to capture transitions between attached and blown off states. The OH* CL and pressure recording times were also too short and finished recording before the end of the attached interval. Regardless, the switching intermittency is characteristic of hysteresis and multistability.

Given that the outlier is the only case where blowoff occurs for a higher φ and Da than normal, it is believed that the hysteresis region is not very large. It is still important for operating procedures to account for this hysteresis and ensure reliable performance.

CHAPTER 6

FORCED DYNAMICS

This chapter investigates the forced response of the combustor using measurements from Campaign 2. First, the mean flow fields are presented to assess the effect of the siren device and the forcing. Next, the FTFs are presented and analyzed to determine how each of the combustor elements and their interactions contribute to the flame dynamics. Spatial FFT fields of the OH* CL illustrate the changes to the forcing spatial pattern as frequency varies and how this spatial pattern influences the FTF gain. Finally, the chapter closes with a discussion of the frequency interactions detected in this combustor and how they affect the interpretation of the FTFs.

6.1 Effects On Mean Flow Field

The mean fuel PLIF signal for cases with thermal power $\mathcal{P}_{\mathrm{th}} = 0.40$ MW at different forcing frequencies is shown in Figure 33. No significant qualitative differences in mean fuel distribution were observed across the different forcing frequencies, indicating no bifurcation in overall flame or flow structure as the system is forced. This observation also held at the different thermal powers, corresponding to leaner φ.

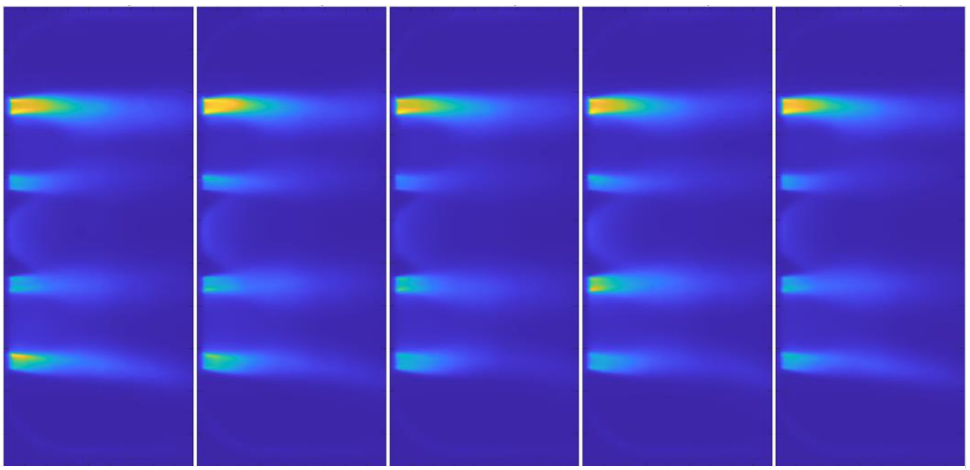

Figure 33: Mean fuel PLIF fields for 0.40 MW at different forcing frequencies.

As will be discussed below, the combustor shows highest response to forcing at f_f = 670 Hz. Figure 34 shows the mean fuel PLIF fields for 670 Hz forcing across different thermal powers. As φ was decreased, unburnt fuel is measured in the recirculation zones behind the combustor bluff bodies and farther downstream. This observation is indicative of local extinction along the inner shear layer between the reactants and recirculation zone, allowing mixing of unburnt reactants. It also is indicative of more axially distributed heat release. The phase-conditioned mean fuel PLIF fields at different phases of the pressure cycle (not shown here) did not demonstrate any coherent oscillations in the fuel flow at any combination of thermal power and forcing frequency. Hence, heat release oscillations at the flame do not appear to be due to oscillating equivalence ratio; heat release oscillations are anticipated to be due to velocity coupling and a detailed analysis of the velocity dynamics is needed.

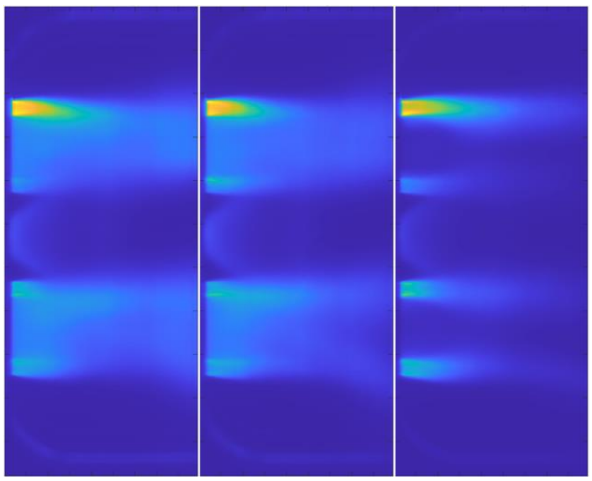

Figure 34: Mean fuel PLIF fields at different FAR for $f_{\mathrm{f}} = 670$ Hz.

Figure 35 shows the mean velocity fields at different forcing frequencies and without forcing at $\mathcal{P}_{\mathrm{th}} = 0.36$ MW. Vector arrows show in the in-plane velocity, while the background colormap indicates the out-of-plane velocity. All absolute velocity scales have been removed for proprietary reasons. Similar to the fuel PLIF fields, there are no major qualitative changes in the velocity field as the system is forced. The largest difference is that the unforced case has a slightly higher swirl velocity in the downstream region compared to the forced cases.

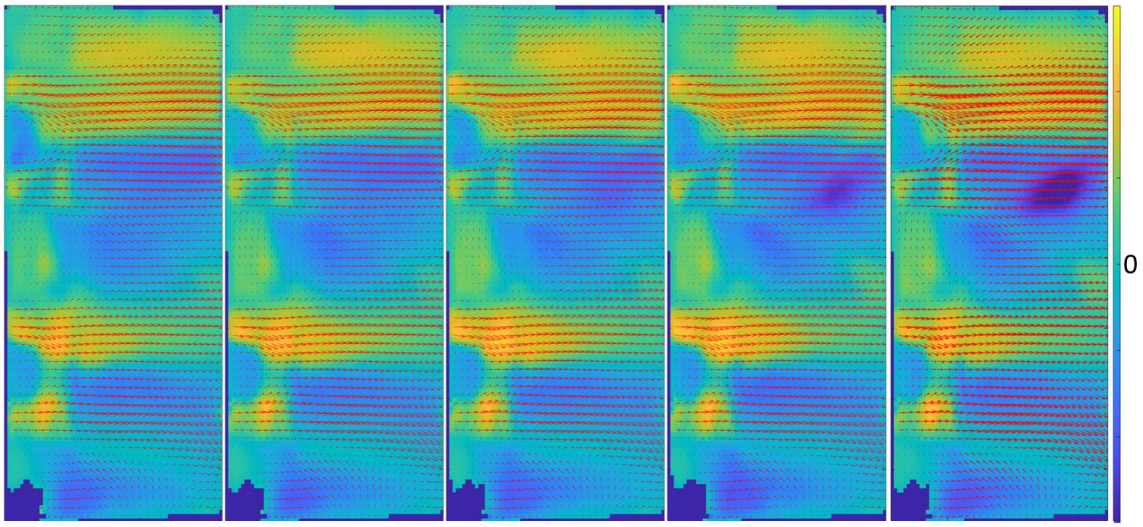

Figure 35: Mean velocity fields for 0.40 MW. Vector arrows are the in-plane velocity and background is the out-of-plane velocity with blue and yellow indicating positive and negative, respectively.

6.2 Forced Flame Response

Overall, the forcing has negligible impact on the mean flow characteristics of the combustor. In addition, there were no cases where the presence of the forcing caused blowoff of an otherwise stable flame. The analysis performed by Salazar *et al*. [89] yields the FTFs illustrated in Figure 36. The two FARs are the conditions where it was possible to stabilize at least one main flame in the combustor. At the leaner FAR, however, the main flames were often blown off and only intermittently reattached.

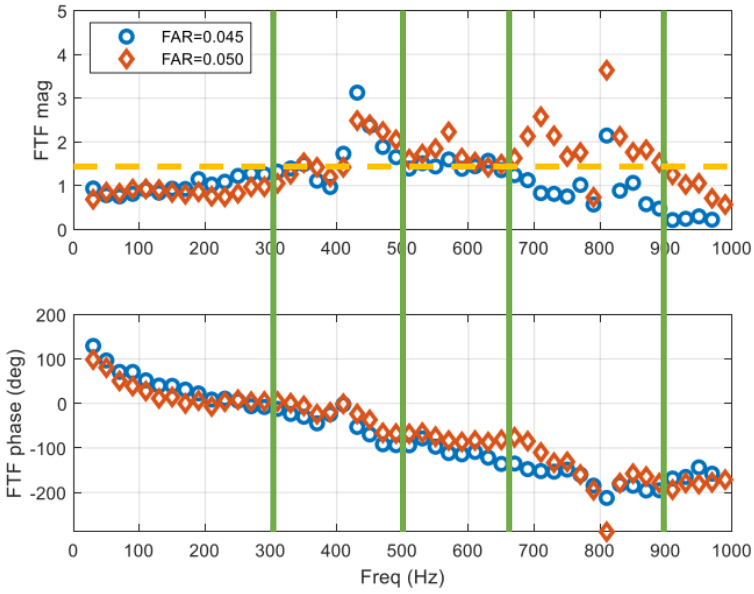

Figure 36: Measured FTFs for two FARs from Campaign 2, modified from [89]. Vertical green lines denote frequencies where optical data was recorded. Horzontal dashed yellow line in upper plot approximates the mean gain across the four frequencies.

Comparing Figures 20 and 36 provides some additional insight on the dynamics of the combustor. From Figure 20 and confirmation with other data sets (not shown), the mains blow off at FAR ≈ 0.045. Thus, the dynamics of the combustor for low FAR correspond to that of the pilot alone, whereas for FAR ≈ 0.050, the dynamics involve the mains and main-pilot interactions. Figure 36 shows that the peaks at ~580 and ~710 Hz vanish when the FAR decreases to 0.045, while the peaks at ~420 and ~810 Hz remain. Together, it may be concluded that the ~580 and ~710 Hz peaks arise from either the mains individual dynamics or the interactions between the main and pilot flames. The ~420 and ~810 Hz peaks, however, must stem from the natural dynamics of the pilot. The observed increase in FTF magnitude as FAR increases is potentially due to the contribution of main and/or main-pilot interactions. Additional experiments are required to validate these hypotheses.

6.3 Phase Cancellation & Spatial Modes

While Figure 36 indicates that the forcing frequencies selected for optical diagnostics have very similar gain, it is still worthwhile to investigate how this might be. To do so, the complex valued FFT fields of the OH* CL images were computed at the highest φ condition across all forcing frequencies and plotted in Figure 37. The unforced case was excluded because it is not possible to extract a corresponding frequency field.

As explained in Section 3.5, the FFT fields can be used to identify regions that are in and out of phase with others, thereby revealing phase cancellation effects. In Figure 37, phase cancellation occurs when both the real and imaginary parts of the FFT are opposite signs at the same spatial locations. The response at each of the forcing frequencies has some cancellation for either the real or imaginary part of the field, but never both simultaneously. This represents the changes in phase that result from the different forcing frequencies, but their magnitudes are all similar, as expected from Figure 36.

Figure 37 also permits a basic, qualitative investigation of the mode shapes at the forcing frequency. Treating the FFT fields as the mode shapes of a Discrete Fourier Transform (DFT) allows interpreting the real and imaginary parts as a complementary mode pair representing the spatial dynamics at a given frequency. Applying this interpretation to Figure 37 reveals that the shape of the pilot's forced oscillations responds the most to the forcing frequency. As f_f increases, the spatial wavelength along the pilot's centreline decreases faster than along the centrelines of the mains. This is more clearly illustrated by the phase fields in Figure 38. The phase fields were computed from the real and imaginary parts of the Fourier mode shapes in Figure 37. Each edge between 0 rad and 2π rad phase represents the end of one wavelength along the axial direction.

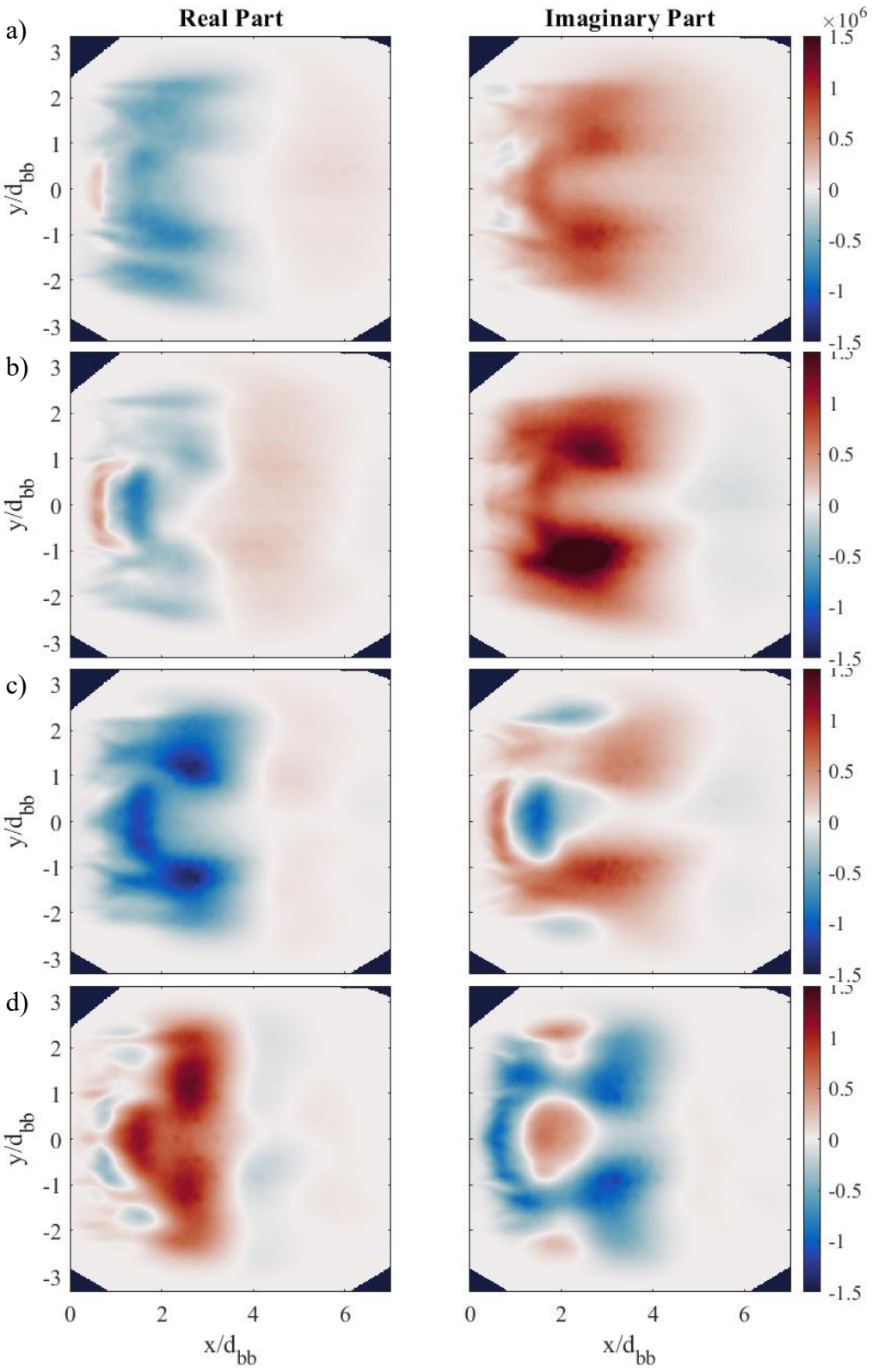

Figure 37: Complex FFT fields of OH* CL from highest φ condition at (a) f_f = 306 Hz, (b) f_f = 503 Hz, (c) f_f = 672 Hz and (d) f_f = 901 Hz.

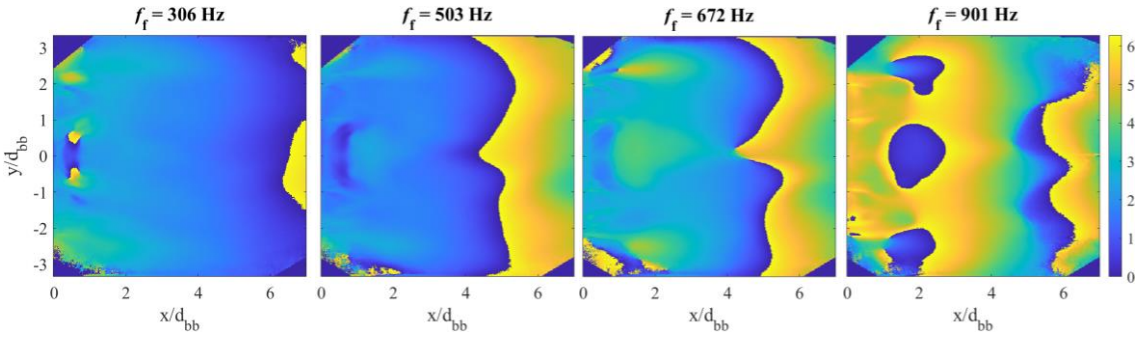

Figure 38: Phase fields from Fourier modes in Figure 38. Phase measured in radians.

Considering the discussion of the pilot's heat release rate in Section 4.2.1 and the evidence of piloted flame stabilization presented in Chapter 5, Figure 37 provides additional support that the dynamics and characteristics of this combustor are pilot-dominated, even when subjected to external forcing. Throughout Figure 37, the highest amplitude fluctuations occur within the pilot region (*i.e.*, $0 \leq x/d_{\mathrm{bb}} \leq 2, |y/d_{\mathrm{bb}}| \leq 2$) and/or the region where the mains and pilot overlap ($2 \leq x/d_{\mathrm{bb}} \leq 4, 1 \leq |y/d_{\mathrm{bb}}| \leq 2$). Given that much of the signal intensity in the overlap region is due to the pilot (cf. Section 4.2.1) and the pilot exhibits higher power fluctuations, it is reasonable to conclude that the higher power fluctuations in the overlap region are mostly from the pilot.

6.4 Frequency Interactions

Thus far, the data collected and presented indicate that the pilot is integral to the nominal operation and characteristics of the LPP combustor investigated. Indeed, the analysis in Sections 6.2 and 6.3 show that the dynamics of this combustor appear pilot dominated. As such, it is important to examine how the forcing interacts with the natural dynamics of the pilot. This analysis is also used to explore how frequency interactions can interfere with measurements for FTFs in practical combustors.

Figure 39 plots the peak frequency fields and spatially resolved power spectra of the OH* CL images for TPs at the highest φ investigated and each of the forcing frequencies. The highest φ condition was chosen because of the blowoff exhibited in data sets at leaner φ. Data sets with blowoff are unsuitable because it is not possible to see the impact of main-pilot interactions or the contributions from the individual mains. The peak frequency fields are computed by plotting the frequency with the highest power at each spatial coordinate in the OH* CL. The resulting fields clearly show where the dominant oscillations exist in the combustor and their frequencies. As explained in Section 4.3, the high power, low frequency (< 100 Hz) oscillations are suspected to be an artifact of the experimental rig, not the combustor design, and have been omitted from this analysis.

Figure 39a shows the results computed for the unforced case. The peak frequency field clearly shows that the pilot oscillates at $f_0 \approx 4.2$ kHz, while the power spectra indicate that this self-excited tone dominates the unforced dynamics. In addition, comparing Figures 27 and Figure 39a shows that the pilot dynamics are antisymmetric since they do not cause global OH* CL oscillations. The corresponding Fourier mode shape of the unforced pilot mode is shown in Figure 40. It is also worth noting that the ~4.2 kHz pilot dynamics are approximately a multiple of the ~420 Hz peak in Figure 36, which was also reasoned to stem from the pilot. Unfortunately, the data recorded to compute the FTFs is not able to resolve the relationship between the two frequencies.

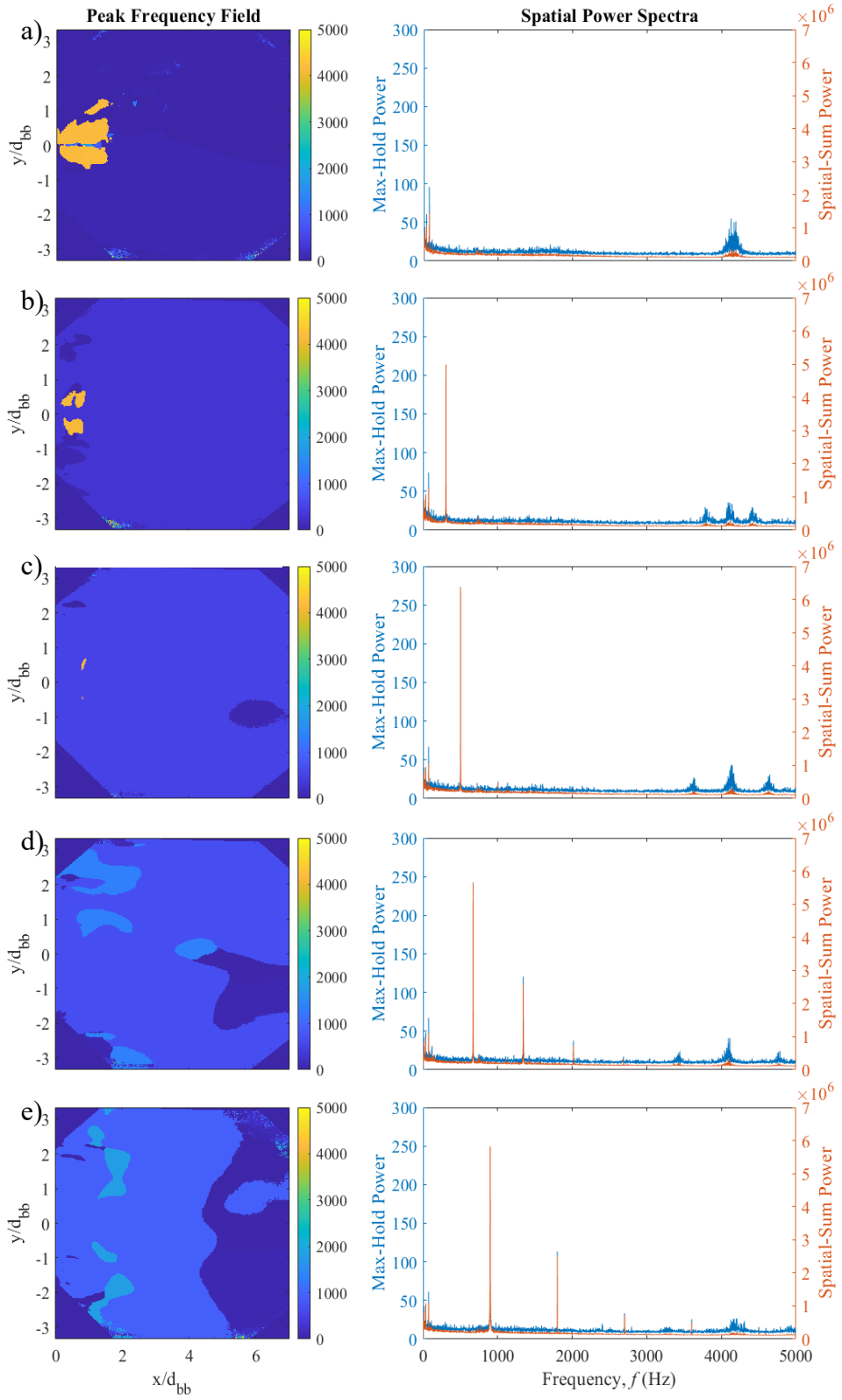

Figure 39: OH* CL peak frequency fields and spatially resolved power spectra at highest φ for (a) unforced, (b) $f_f = 306$ Hz, (c) $f_f = 503$ Hz, (d) $f_f = 672$ Hz and (e) $f_f = 901$ Hz.

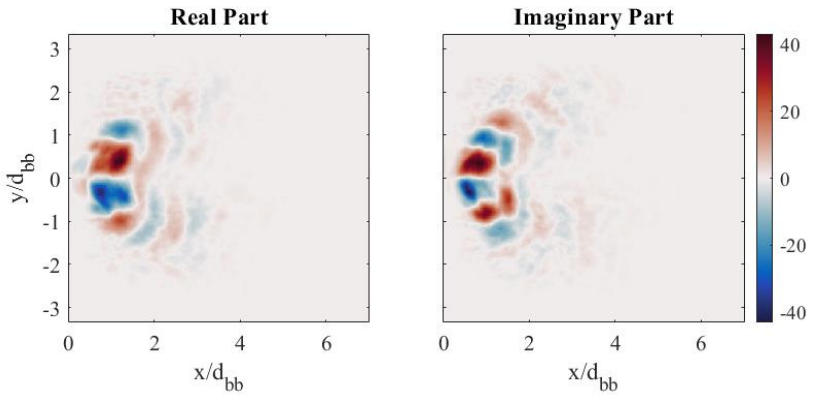

Figure 40: OH* CL Fourier mode of unforced pilot dynamics.

Figure 39b-e illustrate how the applied forcing interacts with the natural dynamics of the pilot. The first effect is the appearance of sum and difference frequencies in the forced cases at $f_0 \pm f_f$. The second effect, called frequency pulling or pushing [60], causes the peak frequency of the pilot's natural dynamics to shift towards nearby harmonics of f_f, because of one-way coupling and real wave properties as described in Section 1.3.3. For example, forcing at $f_f = 671$ Hz shifts the pilot oscillations by ~100 Hz to ~4.1 kHz. While there should be a relationship between the shift in f_0 and f_f, the present data is not able to resolve this relation due to variation in forcing amplitude across the cases.

The effects of frequency interactions are important in the context of FTF measurements. As f_0 shifts towards a harmonic of f_f, similar effects can manifest such as those encountered along synchronization routes [51]. As a result, these frequency interactions can reduce or amplify the response at the forcing frequency. This means that the measured response to the forcing frequency is coupled with the self-excited dynamics. Neither the frequency pulling/pushing nor the amplification effects are captured by FTFs (cf. Section 1.3.2). These effects have been previously reported in a practical gas turbine combustor by Hochgreb *et al*. [42].

CHAPTER 7

CONCLUSIONS

7.1 Summary & Contributions

The primary goal of this work was to experimentally characterize the mean flow field, dynamics and operating limits of a novel LPP combustor with relevance to applications in CST aircraft. This research was motivated to investigate three areas of concern with respect to the viability for LPP combustors in CST applications. The three areas were pollutant emissions, operability limits and combustor dynamics. In contrast with existing LPP combustor studies, the work in this thesis explores conditions at higher T_3 and lower P_3 than those found in conventional, subsonic aero-engines. In addition, the LPP combustor studied involved multiple interacting combustor elements. Specifically, the mixer had a central, swirl stabilized pilot flame surrounded by four annular, low swirl, bluff-body stabilized main flames. Experiments deployed high-speed OH* CL and SPIV with low-speed fuel PLIF to obtain measurements of heat release rate, gas phase velocity and fuel-air mixing, respectively.

Overall, the results indicate that LPP combustors have significant potential for CST applications. Parameter sweeps of P_3, T_3 and FAR provided valuable emissions data that indicate similar LPP combustors will be able to meet and exceed future pollutant regulations [21]. The unforced dynamics and mean fields are similarly encouraging, with variations in P_3, T_3 and FAR yielding minimal changes to the pressure and heat release rate dynamics, except in cases where blowoff occurred. Interestingly, the blown off conditions exhibited similar dynamics to those without blowoff. Together with the OH* mean fields,

these results suggest that the pilot flame is a dominant contributor to the flow characteristics.

The OH* CL and fuel PLIF revealed the complexity of the multi-element flow field within the combustor. As a result, it was necessary to execute a detailed blowoff analysis. The results from this analysis show that the combustor design studied has enhanced blowoff limits compared to single-element bluff-body stabilized combustors previously reported in literature. Specifically, for the range of Re conditions collected, the Da at blowoff is lower than those reported in literature for axisymmetric bluff-bodies. Further analysis indicates that the enhanced flame stability is due to the presence of the pilot flame. The pilot flame itself acts as a persistent ignition source for the mains and the hot combustion products from the pilot are recirculated to the dome face to heat the fresh reactants from the mains, keeping the main flames ignited and preventing blowoff. Within the mixing zones where the pilot flow path intersects the mains, the pilot helps anchor the main flames due to its slightly rich φ and due to symmetry-breaking effects. In fact, the collected data falls along the (Re, Da) trend reported in literature for planar bluff-bodies. Again, this evidences the importance of the pilot flame to the operation and nominal characteristics of this LPP combustor.

The importance of the pilot flame is further supported by the forced flame response data. The empirically-obtained FTFs show that for nominal conditions (*i.e.*, all flames attached) the flame responds most at four frequencies. When the main flames blow off, however, two of the FTF peaks vanish, indicating that the remaining two stem from the pilot dynamics. Analyzing the spatial FFT fields of the OH* CL reveals that the pilot is dominated by dynamics near 4.2 kHz, which is a harmonic of one of the FTF peaks.

Furthermore, the spatial FFT fields at the forcing frequencies indicate the pilot responds the most to the forcing. Coupled with the blowoff analysis, mean fields and unforced dynamics, the results demonstrate that this combustor is pilot-dominated.

Together, this thesis collects and presents experimental data of a multi-element LPP combustor operating at CST-relevant conditions. The results show that the pilot flame is integral to the stable and robust operation of the combustor across a range of conditions. This shows how important it is to account for the interactions of various combustor elements in complex mixer designs. That said, much of the existing tools and theory already developed for single-element combustors is still relevant for multi-element designs. Da-based correlations for blowoff, for example, provide reasonable agreement with the data presented in this work, despite many assumptions and simplifications made to facilitate the computation of Da and Re in this combustor. Finally, the data collected in this thesis is part of an ongoing validation effort to determine the applicability and accuracy of existing numerical and analytical combustor models.

7.2 Future Work

While the present work provides insight into the complex flow and flame interactions in a multi-element LPP combustor, there are still some limitations to the data collected. In particular, the laser diagnostics were limited to a single laser sheet position. This means that the fuel PLIF and SPIV results could only study the flow fields along the centrelines of the mains. Future studies should collect data regarding the flow field along the pilot centreline and along planes between the mains and pilot, where the pilot and main flows mix. Obviously, such data could be used to validate numerical models and simulations.

However, it can also provide more concrete information regarding the fluid and chemical processes that occur in the mixing regions.

For the flame blowoff analysis, future work should study the flame stability of a single main and attempt to isolate the individual contributions of various interactions. For example, this work was not able to distinguish between the effects of main-main interactions and pilot-main interactions. Additional studies could also investigate the dynamics and behaviours leading up to and during the blowoff process. Existing studies [22, 23] are limited to single-element combustors and thus do not resolve how interacting flows and flames might alter the physical mechanism of blowoff.

With regards to the forced dynamics, there is much that can be learned with a finer sweep of f_f and forcing amplitude. Given that the mains and pilot flames have different φ, stabilization approaches and basic flow features, it is likely that they each respond differently to forcing. A high-resolution forcing sweep could investigate synchronization modes between the pilot and mains. This could reveal how the spatial pattern of the forcing influences the response of the combustor, which has not been studied for multi-element combustors such as this one. Alternatively, such a study could determine the relationship between f_f and the pilot frequency, expanding on the observations of frequency-pulling described in this work.

Ongoing work is using the experimental SPIV results to validate computational fluid simulations used for analyzing combustor dynamics. One part of these efforts is the development of analytical FTF models to capture the convective velocity of flow and flame perturbations. These current simulations assume that the convective velocity of acoustic and flow perturbations is not affected by the presence of the flame and that the presence of

the pilot and main flows do not interact and alter flow symmetry or periodicity. The experimental data in this thesis can be used to evaluate the validity of those assumptions and quantify their impact on the accuracy of the derived models and simulations. Furthermore, comparisons between experimentally and numerically derived FTFs could reveal which physical mechanisms are not adequately captured by the simulations.

REFERENCES

[1] J. Steelant, "LAPCAT Publishable Final Activity Report," ESA-ESTEC, 2008.

[2] Y. Liu, X. Sun, V. Sethi, D. Nalianda, Y.-G. Li and L. Wang, "Review of Modern Low Emissions Combustion Technologies for Aero Gas Turbine Engines," *Progress in Aerospace Sciences,* vol. 94, pp. 12-45, October 2017.

[3] J. Zhang, D. Wuebbles, D. Kinnison and S. L. Baughcum, "Stratospheric Ozone and Climate Forcing Sensitivity to Cruise Altitudes for Fleets of Potential Supersonic Transport Aircraft," *Journal of Geophysical Research: Atmospheres,* vol. 126, no. 16, p. e2021JD034971, 2021.

[4] J. Wen, C. J. Weit, M. Mayakonda, A. Anand, T. Zaidi and D. Mavris, "A Methodology for Supersonic Commercial Market Estimation and Environmental Impact Evaluation (Part II)," in *AIAA Aviation Forum*, Virtual, 2020.

[5] D. Rutherford, B. Graver and C. Chen, "Noise and Climate Impacts of an Unconstrained Commercial Supersonic Network," The International Council on Clean Transportation, 2019.

[6] B. Owen, J. G. Anet, N. Bertier, S. Christie, M. Cremaschi, S. Dellaert, J. Ebedeli, U. Janicke, J. Kuenen, L. Lim and E. Terrenoire, "Review: Particulate Matter Emissions from Aircraft," *Atmosphere,* vol. 1230, p. 13, 2022.

[7] S. R. Turns, An Introduction to Combustion: Concepts and Applications, 3rd ed., New York: McGraw-Hill, 2012.

[8] Y. Huang and Y. Vigor, "Dynamics and Stability of Lean-Premixed Swirl-Stabilized Combustion," *Progress in Energy and Combustion Science,* vol. 35, no. 4, pp. 293-364, 2009.

[9] A. Kharina, T. MacDonald and D. Rutherford, "Environmental Performance of Emerging Supersonic Transport Aircraft," The International Council on Clean Transportation, 2018.

[10] J. J. Berton, D. L. Huff, J. A. Seidel and K. A. Geiselhart, "Supersonic Technology Concept Aeroplanes for Environmental Studies," in *AIAA SciTech Forum and Exposition*, Orlando, 2020.

[11] J. K. Lytle, "The Numerical Propulsion System Simulation: An Overview," NASA, Cleveland, 2000.

[12] R. L. Speth, S. D. Eastham, T. M. Fritz, I. Sanz-Morére, A. Agarwal, P. Prashanth, F. Allroggen and S. R. H. Barrett, "Global Environmental Impact of Supersonic Cruise Aircraft in the Stratosphere," NASA, Cleveland, 2021.

[13] L. J. A. Voet, P. Prashanth, R. L. Speth, J. S. Sabnis, C. S. Tan and S. R. H. Barrett, "The Impact of Design Space Constraints on the Noise and Emissions from Derivative Engines for Civil Supersonic Aircraft," in *AIAA SciTech Forum*, Virtual, 2021.

[14] M. Hassan, H. Pfaender and D. Mavris, "Design Tools for Conceptual Analysis of Future Commercial Supersonic Aircraft," in *AIAA Aviation Forum*, Virtual, 2020.

[15] R. W. Niedzwiecki, "Low Emissions Combustor Technology for High-Speed Civil Transport Engines," NASA, Cleveland, 1992.

[16] S. C. Greenfield, P. V. Heberling and G. E. Moertle, "HSCT Sector Combustor Hardware Modifications for Improved Combustor Design," NASA, Cleveland, 2005.

[17] K. M. Tacina, D. P. Podboy, F. P. Lee and B. Dam, "Gaseous Emissions Results from a Three-Cup Flametube Test of a Third-Generation Swirl-Venturi Lean Direct Injection Combustion Concept," in *Turbo Expo: Power for Land, Sea, and Air*, Phoenix, 2019.

[18] K. Ajmani, F. P. Lee, C. T. Chang and M. T. Kudlac, "CFD Evaluation Of Lean-Direct Injection Combustors for Commercial Supersonics Technology," in *AIAA Propulsion and Energy Forum*, Indianapolis, 2019.

[19] F. E. C. Culick, "Unsteady Motions in Combustion Chambers for Propulsion Systems," NATO, Washington, 2006.

[20] J. E. Temme, P. M. Allison and J. F. Driscoll, "Combustion Instability of a Lean Premixed Prevaporized Gas Turbine Combustor Studies Using Phase-Averaged PIV," *Combustion and Flame,* vol. 161, pp. 958-970, 2014.

[21] NASA, "ARMD Strategic Implementation Plan," NASA, Cleveland, 2019.

[22] S. J. Shanbhogue, S. Husain and T. Lieuwen, "Lean Blowoff of Bluff Body Stabilized Flames: Scaling and Dynamics," *Progress in Energy and Combustion Science,* vol. 35, pp. 98-120, 2009.

[23] S. G. Tuttle, "Blowoff Behavior of Bluff Body Stabilized Flames in Vitiated and Partially Premixed Flows," University of Connecticut, Storrs, 2010.

[24] D. E. Cavaliere, J. Kariuki and E. Mastorakos, "A Comparison of the Blow-Off Behaviour of Swirl-Stabilized Premixed, Non-Premixed and Spray Flames," *Flow, Turbulence and Combustion,* vol. 91, pp. 347-372, September 2013.

[25] Z. Wang, B. Hu, A. Fang, Q. Zhao and X. Chen, "Analyzing Lean Blow-off Limits of Gas Turbine Combustors Based on Local and Global Damköhler Number of Reaction Zone," *Aerospace Science and Technology,* vol. 111, p. 106532, April 2021.

[26] Q. An and A. M. Steinberg, "The Role of Strain Rate, Local Extinction, and Hydrodynamic Instability on Transition Between Attached and Lifted Swirl Flames," *Combustion and Flame,* vol. 199, pp. 267-278, January 2019.

[27] R. Shan and T. Lu, "Ignition and Extinction in Perfectly Stirred Reactors with Detailed Chemistry," *Combustion and Flame,* vol. 159, no. 6, pp. 2069-2076, 2012.

[28] M. Kooshbaghi, C. E. Frouzakis, K. Boulouchos and I. V. Karlin, "n-Heptane/Air Combustion in Perfectly Stirred Reactors: Dynamics, Bifurcations and Dominant Reactions at Critical Conditions," *Combustion and Flame,* vol. 162, no. 9, pp. 3166-3179, 2015.

[29] C. Foley, I. Chterev, B. Noble, J. Seitzman and T. Lieuwen, "Shear Layer Flame Stabilization Sensitivities in a Swirling Flow," *International Journal of Spray and Combustion Dynamics,* vol. 9, no. 1, pp. 3-18, 2016.

[30] S. H. Strogatz, Nonlinear Dynamics and Chaos: With Applications to Physics, Biology, Chemistry, and Engineering, Boca Raton: CRC Press, 2015.

[31] S. Kheirkhah, J. D. M. Cirtwill, P. Saini, K. Venkatesan and A. M. Steinberg, "Dynamics and Mechanisms of Pressure, Heat Release Rate, and Fuel Spray Coupling During Intermittent Thermoacoustic Oscillations in a Model Aeronautical

Combustor at Elevated Pressure," *Combustion and Flame,* vol. 185, pp. 319-334, 2017.

[32] S. Candel, "Combustion Dynamics and Control: Progress and Challenges," *Proceedings of the Combustion Institute,* vol. 29, no. 1, pp. 1-28, 2002.

[33] T. Poinsot, "Prediction and Control of Combustion Instabilities in Real Engines," *Proceedings of the Combustion Institute,* vol. 36, no. 1, pp. 1-28, 2017.

[34] S. Ducruix, T. Schuller, D. Durox and S. Candel, "Combustion Dynamics and Instabilities: Elementary Coupling and Driving Mechanisms," *Journal of Propulsion and Power,* vol. 19, no. 5, pp. 722-734, 2003.

[35] N. Noiray, D. Durox, T. Schuller and S. Candel, "A Unified Framework for Nonlinear Combustion Instability Analysis based on the Flame Describing Function," *Journal of Fluid Mechanics,* vol. 615, pp. 139-167, 2008.

[36] S. J. Illingworth and M. P. Juniper, "When Will a Flame Describing Function Approach to Thermoacoustics Work Well?," in *International Congress on Sound and Vibration*, Vilnius, 2012.

[37] J. P. Moeck and C. O. Paschereit, "Nonlinear Interactions of Multiple Linearly Unstable Thermoacoustic Modes," *International Journal of Spray and Combustion Dynamics,* vol. 4, no. 1, pp. 1-28, 2012.

[38] M. P. Juniper and R. I. Sujith, "Sensitivity and Nonlinearity of Thermoacoustic Oscillations," *Annual Review of Fluid Mechanics,* vol. 50, pp. 661-89, 2018.

[39] M. Haeringer, M. Merk and W. Polifke, "Inclusion of Higher Harmonics in the Flame Describing Function for Predicting Limit Cycles of Self-Excited Combustion Instabilities," *Proceedings of the Combustion Institute,* vol. 37, no. 4, pp. 5255-5262, 2019.

[40] S. Balusamy, L. K. B. Li, Z. Han and S. Hochgreb, "Extracting Flame Describing Functions in the Presence of Self-Excited Thermoacoustic Oscillations," *Proceedings of the Combustion Institute,* vol. 36, no. 3, pp. 3851-3861, 2017.

[41] B. D. Bellows, A. Hreiz and T. Lieuwen, "Nonlinear Interactions Between Forced and Self-Excited Acoustic Oscillations in Premixed Combustor," *Journal of Propulsion and Power,* vol. 24, no. 3, pp. 628-31, 2008.

[42] S. Hochgreb, D. Dennis, I. Ayranci, W. Bainbridge and S. Cant, "Forced and Self-excited Instabilities from Lean Premixed, Liquid-fueled Aeroengine Injectors at High Pressures and Temperatures," in *Proceedings of ASME Turbo Expo 2013*, San Antonio, 2013.

[43] K. T. Kim, "Nonlinear Interactions Between the Fundamental and Higher Harmonics of Self-Excited Combustion Instabilities," *Combustion Science and Technology,* vol. 189, no. 7, pp. 1091-1106, 2017.

[44] M. L. Passarelli, T. M. Wabel, K. Venkatesan, A. Cross and A. M. Steinberg, "Influence of Cross-Frequency Interactions on Nonstationary Thermoacoustic Oscillations in a Rich-Burn Gas Turbine Combustor at Elevated Pressure," in *AIAA Propulsion & Energy Forum*, Indianapolis, 2019.

[45] A. Orchini and M. P. Juniper, "Flame Double Input Describing Function Analysis," *Combustion and Flame,* vol. 171, pp. 87-102, 2016.

[46] A. Jenkins, "Self-oscillation," *Physics Reports,* vol. 525, no. 2, pp. 167-222, 2013.

[47] M. Bennett, M. F. Schatz, H. Rockwood and K. Wiesenfeld, "Huygen's Clocks," *Proceedings: Mathematical, Physical and Engineering Sciences,* vol. 458, no. 2019, pp. 563-579, 2002.

[48] N. H. Fletcher, "The Nonlinear Physics of Musical Instruments," *Reports on Progress in Physics,* vol. 62, no. 5, pp. 723-764, 1999.

[49] D. Volk, I. Dubinin, A. Myasnikova, B. Gutkin and V. K. Nikulin, "Generalized Cross-Frequency Decomposition: A Method for the Extraction of Neuronal Components Coupled at Different Frequencies," *Frontiers in Neuroinformatics,* vol. 12, no. 72, 2018.

[50] J. W. Strutt Baron Rayleigh, The Theory of Sound, 2nd ed., New York: Dover, 1945.

[51] A. Balanov, N. Janson, D. Postnov and O. Sosnovtseva, Synchronization: From Simple to Complex, Heidelberg: Springer Berlin, 2009.

[52] A. Pikovsky, M. Rosenblum and J. Kurths, Synchronization: A Universal Concept in Nonlinear Sciences, Cambridge: Cambridge University Press, 2001.

[53] M. Cross and H. Greenside, Pattern Formation and Dynamics in Nonequilibrium Systems, New York: Cambridge University Press, 2009.

[54] S. Mondal, S. A. Pawar and R. I. Sujith, "Forced Synchronization and Asynchronous Quenching of Periodic Oscillations in a Thermoacoustic System," *Journal of Fluid Mechanics,* vol. 864, pp. 73-96, 2019.

[55] R. I. Sujith and V. R. Unni, "Complex System Approach to Investigate and Mitigate Thermoacoustic Instability in Turbulent Combustors," *Physics of Fluids,* vol. 32, p. 061401, 2020.

[56] K. Moon, Y. Guan, L. K. B. Li and K. T. Kim, "Mutual Synchronization of Two Flame-driven Thermoacoustic Oscillators: Dissipative and Time-delayed Coupling Effects," *Chaos,* vol. 30, p. 023110, 2020.

[57] J. M. Palva and S. Palva, "Functional Integration Across Oscillation Frequncies by Cross-Frequency Phase Synchronization," *European Journal of Neuroscience,* vol. 48, no. 7, pp. 2399-2406, 2017.

[58] S. Mondal, S. A. Pawar and R. I. Sujith, "Synchronous Behaviour of Two Interacting Oscillatory Systems Undergoing Quasiperiodic Route to Chaos," *Chaos: An Interdisciplinary Journal of Nonlinear Science,* vol. 27, no. 10, pp. 103119-1-9, 2017.

[59] Y. Guan, V. Gupta and L. K. B. Li, "Intermittency Route to Self-excited Chaotic Thermoacoustic Oscillations," *Journal of Fluid Mechanics,* vol. 894, no. R3, 2020.

[60] Y. Guan, V. Gupta, M. Wan and L. K. B. Li, "Forced Synchronization of Quasiperiodic Oscillations in a Thermoacoustic System," *Journal of Fluid Mechanics,* vol. 879, pp. 390-421, 2019.

[61] Y. Guan, L. K. B. Li, B. Ahn and K. T. Kim, "Chaos, Synchronization, and Desynchronization in a Liquid-Fueled Diffusion-Flame Combustor with an Intrinsic Hydrodynamic Mode," *Chaos,* vol. 29, p. 053124, 2019.

[62] Y. Guan, K. Moon, K. T. Kim and L. K. B. Li, "Low-order Modeling of the Mutual Synchronization between Two Turbulent Thermoacoustic Oscillators," *Physical Review E,* vol. 104, p. 024216, 2021.

[63] K. Kashinath, L. K. B. Li and M. P. Juniper, "Forced Synchronization of Periodic and Aperiodic Thermoacoustic Oscillations: Lock-in, Bifurcations and Open-loop Control," *Journal of Fluid Mechanics,* vol. 838, pp. 690-714, 2018.

[64] Y. Guan, M. Murugesan and L. K. B. Li, "Strange Nonchaotic and Chaotic Attractors in a Self-excited Thermoacoustic Oscillator Subjected to External Periodic Forcing," *Chaos: An Interdisciplinary Journal of Nonlinear Science,* vol. 28, no. 9, p. 093109, 2018.

[65] M. L. Passarelli, "An Investigation of Cross-Frequency Interactions in a Gas Turbine Combustor at Flight-Relevant Conditions," University of Toronto, Toronto, 2019.

[66] M. L. Passarelli, S. E. Wonfor, A. X. Zheng, S. Ram Manikandan, Y. Mazumdar, J. M. Seitzman, A. M. Steinberg, H. Bower, J. Hong, K. Venkatesan and M. Benjamin, "Experimental Characterization of a Lean Pre-vaporized Premixed Combustor for Supersonic Transport Applications," in *AIAA SciTech Forum*, San Diego, 2022.

[67] P. Saini, C. M. Arndt and A. M. Steinberg, "Development and Evaluation of Gappy-POD as a Data Reconstruction Technique for Noisy PIV Measurements in Gas Turbine Combustors," *Experiments in Fluids,* vol. 57, no. 7, 2016.

[68] T. García-Armingol, Y. Hardalupas, A. M. K. P. Taylor and J. Ballester, "Effect of Local Flame Properties on Chemiluminescence-based Stoichiometry Measurement," *Experimental Thermal and Fluid Science,* vol. 53, pp. 93-103, 2014.

[69] B. O. Ayoola, R. Blachandran, J. H. Frank, E. Mastorakos and C. F. Kaminski, "Spatially Resolved Heat Release Rate Measurements in Turbulent Premixed Flames," *Combustion and Flame,* vol. 144, no. 1-2, pp. 1-16, 2006.

[70] T. García-Armingol and J. Ballester, "Flame Chemiluminescence in Premixed Combustion of Hydrogen-enriched Fuels," *International Journal of Hydrogen Energy,* vol. 39, no. 21, pp. 11299-11307, 2014.

[71] J. G. Lee and D. A. Santavicca, "Experimental Diagnostics for the Study of Combustion Instabilities in Lean Premixed Combustors," *Journal of Propulsion and Power,* vol. 19, no. 5, pp. 735-750, 2003.

[72] V. N. Nori and J. M. Seitzman, "CH* Chemiluminescence Modeling for Combustion Diagnostics," *Proceedings of the Combustion Institute,* vol. 32, no. 1, pp. 895-903, 2009.

[73] C. S. Panoutsos, Y. Hardalupas and A. M. K. P. Taylor, "Numerical Evaluation of Equivalence Ratio Measurement using OH* and CH* Chemiluminescence in Premixed and Non-Premixed Methane–Air Flames," *Combustion and Flame,* vol. 156, no. 2, pp. 273-291, 2009.

[74] M. Lauer, M. Zellhuber, T. Sattelmayer and C. J. Aul, "Determination of the Heat Release Distribution in Turbulent Flames by a Model Based Correction of OH* Chemiluminescence," *Journal of Engineering for Gas Turbines and Power,* vol. 133, no. 12, pp. 121501-121501-8, 2011.

[75] Y. Hardalupas and M. Orain, "Local Measurements of the Time-Dependent Heat Release Rate and Equivalence Ratio Using Chemiluminescent Emission from a Flame," *Combustion and Flame,* vol. 139, pp. 188-207, 2004.

[76] H. Kang, C. Yoon and K. T. Kim, "Experimental and Numerical Investigations of Forced Response of Multi-Element Lean-Premixed Hydrogen Flames," *Combustion and Flame,* vol. 258, p. 113079, December 2023.

[77] A. C. Eckbreth, Laser Diagnostics for Combustion Temperature and Species, London: Taylor & Francis, 1996.

[78] T. Wabel, P. Zhang, X. Zhao, H. Wang, E. Hawkes and A. Steinberg, "Assessment of Chemical Scalars for Heat Release Rate Measurement in Highly Turbulent Premixed Combustion Including Experimental Factors," *Combustion and Flame,* 2017.

[79] M. Orain, P. Baranger, C. Ledier, J. Apeloig and F. Grisch, "Fluorescence Spectroscopy of Kerosene Vapour at High Temperatures and Pressures: Potential for Gas Turbines Measurements," *Applied Physics B,* vol. 116, pp. 729-745, 2014.

[80] M. Raffel, C. E. Willert, S. Wereley and J. Kompenhaus, Particle Image Velocimetry: A Practical Guide, Springer, 2013.

[81] M. L. Passarelli, T. M. Wabel, A. Cross, K. Venkatesan and A. M. Steinberg, "Cross-Frequency Coupling During Thermoacoustic Oscillations in a Pressurized Aeronautical Gas Turbine Model Combustor," *Proceedings of the Combustion Institute,* vol. 38, no. 4, pp. 6105-6113, 2021.

[82] W. Hai, X. Rui, W. Kun, C. T. Bowman, R. K. Hanson, D. F. Davidson, K. Brezinsky and F. N. Egolfopoulos, "A Physics-based Approach to Modeling Real-fuel Combustion Chemistry - I. Evidence from Experiments, and Thermodynamic,

Chemical Kinetic and Statistical Considerations," *Combustion and Flame,* vol. 193, pp. 502-519, July 2018.

[83] X. Rui, W. Kun, S. Banerjee, S. Jiankun, T. Parise, Z. Yangye, W. Shengkai, A. Movaghar, L. D. Joon, Z. Runhua, H. Xu, G. Yang, L. Tianfeng, K. Brezinsky, F. N. Egolfopoulos, D. F. Davidson, R. K. Hanson, C. T. Bowman and W. Hai, "A Physics-based Approach to Modeling Real-fuel Combustion Chemistry - II. Reaction Kinetic Models of Jet and Rocket Fuels," *Combustion and Flame,* vol. 193, pp. 520-537, July 2018.

[84] ANSYS, Inc., "Chemkin-Pro Theory Manual," ANSYS, Inc., 2020.

[85] C. R. Wilke, "A Viscosity Equation for Gas Mixtures," *Journal of Chemical Physics,* vol. 18, no. 4, pp. 517-519, 1950.

[86] R. B. Bird, W. E. Stewart and E. N. Lightfoot, Transport Phenomena, New York: John Wiley and Sons, 1960.

[87] Z. Xi, Z. Fu, X. Hu, S. W. Sabir and Y. Jiang, "An Experimental Investigation on the NO and CO Emission Characteristics of a Swirl Convergent-Divergent Nozzle at Elevated Pressure," *Energies,* vol. 11, no. 6, p. 1410, 2018.

[88] V. Nair, "Shear Layer Dynamics of a Reacting Jet in a Vitiated Crossflow," Georgia Institute of Technology, Atlanta, 2020.

[89] V. Salazar, K. Venkatesan, F. Han, S. Wonfor, M. Passarelli and A. Zheng, "Acoustic and Optical Flame Transfer Function Measurements in a High-Pressure Lean-Burn Aero-Engine Combustor Fueled With Jet A," in *Proceedings of the ASME Turbo Expo 2023*, Boston, 2023.